

ABSTRACT

Title of Dissertation: QUANTITATIVE IMAGING OF SHEET
RESISTANCE, PERMITTIVITY, AND
FERROELECTRIC CRITICAL PHENOMENA
WITH A NEAR-FIELD SCANNING
MICROWAVE MICROSCOPE

David Ethan Steinhauer, Doctor of Philosophy, 2000

Dissertation directed by: Associate Professor Steven M. Anlage
Department of Physics

I describe the design and use of a near-field scanning microwave microscope to make quantitative measurements of sample properties, such as sheet resistance and permittivity. The system consists of a resonator contained in a coaxial cable, terminated at one end with an open-ended coaxial probe. When a sample is brought near the probe tip, the resonant frequency and quality factor are perturbed depending on the local properties of the sample. The spatial resolution depends on the diameter of the probe's center conductor, which can be in the range 1–500 μm . This versatile technique is nondestructive, and has broadband (0.1–50 GHz) capability.

Quantitative imaging of the sheet resistance of conducting thin films can be achieved through a thin-film calibration sample. To reinforce our understanding of the physical mechanisms of the measurement, I use a physical model for the system based on microwave transmission line theory. I demonstrate the technique at 7.5 GHz by imaging the sheet resistance of a variable-thickness $\text{YBa}_2\text{Cu}_3\text{O}_{7-\delta}$ thin film on a sapphire substrate at room temperature.

Using a probe with a sharp, protruding center conductor held in contact with the sample, high-resolution ($1\text{ }\mu\text{m}$) imaging can be accomplished. I use a finite element calculation of the electric field near the probe tip, combined with perturbation theory, to make quantitative linear and nonlinear dielectric measurements of thin films and crystals. I demonstrate this capability by imaging the dielectric permittivity and nonlinearity of a $(\text{Ba,Sr})\text{TiO}_3$ thin film.

The microscope can also be used to image domains in ferroelectric crystals such as lithium niobate, barium titanate, and deuterated triglycine sulfate (DTGS). Critical phenomena can be investigated by varying the temperature of the sample. I measured the permittivity, dielectric nonlinearity, and domain relaxation time of DTGS as a function of temperature near the ferroelectric transition. For permittivity measurements, I found reasonable agreement with thermodynamic theory.

QUANTITATIVE IMAGING OF SHEET RESISTANCE,
PERMITTIVITY, AND FERROELECTRIC CRITICAL
PHENOMENA WITH A NEAR-FIELD SCANNING
MICROWAVE MICROSCOPE

by

David Ethan Steinhauer

Dissertation submitted to the Faculty of the Graduate School of the
University of Maryland, College Park in partial fulfillment
of the requirements for the degree of
Doctor of Philosophy
2000

Advisory Committee:

Associate Professor Steven M. Anlage, Chairman/Advisor
Professor Christopher J. Lobb
Professor Ramamoorthy Ramesh
Assistant Professor Ichiro Takeuchi
Professor Ellen Williams

© Copyright by
David Ethan Steinhauer
2000

DEDICATION

To Jenni

ACKNOWLEDGMENTS

First, I would like to thank my advisor, Steve Anlage, for his enthusiasm, positive attitude, and continual encouragement. Second, I would like to thank my co-workers: Gus Vlahacos, with whom I had interesting conversations about many things, and not just physics; Andy Schwartz, whose knowledge and positive attitude have been an inspiration; Dave Kokales, Ashfaq Thanawalla, Vladimir Talanov, John Lee, Atif Imtiaz, Sudeep Dutta, Ali Gokirmak, Wensheng Hu, Lucia Mercaldo, Johan Feenstra, Mark Scheffler, Georg Breunig, and Jesse Bridgewater. They have all been great people to work with. I thank Chadwick Canedy for his assistance by making numerous thin-film samples, and Andrei Stanishevsky for his work with focused ion beams. I also thank Hans Christen for his assistance, and the valuable experience that I was able to gain working with him at Neocera. I acknowledge Fred Wellstood, Doug Bensen, Brian Straughn, and Sangjin Hyun for their various roles which have helped me with my

research. I would like to thank Chris Lobb, Ramamoorthy Ramesh, Ellen Williams, and Ichiro Takeuchi for being on my doctoral defense committee. I thank my parents for a lifetime of encouragement and support; my brother, Jonathan, for his friendship; and my father- and mother-in-law for their encouragement. I thank God for blessing me in so many ways, most of all by giving me my wife, Jenni, and our children, Joshua and Abigail. Finally, and most importantly, I wish to thank my loving wife, Jenni, for being my constant companion and encouragement, and for giving up so much by marrying me and moving to Maryland. The nearly four years we have been married have been the best in my life.

TABLE OF CONTENTS

List of Tables	x
List of Figures	xi
1 Introduction	1
1.1 Overview of Microwave Measurements	1
1.2 Motivation for the Experiment	4
1.3 Outline of Dissertation	4
2 Description of the Experiment	7
2.1 Overview of Experimental Apparatus	7
2.2 Comparison between Non-Contact and Contact Modes	10
2.3 The Frequency-Following Circuit	16
2.4 Measuring the Q of the Resonator	18
2.4.1 The General Idea	18
2.4.2 Finding the Reflection Coefficient	19
2.4.3 Calculating Q from the Width of a Resonant Minimum . .	19
2.4.4 Calculating Q Using a Curve Fit	22
2.4.5 The Q Calibration Process	23
2.5 Obtaining Calibrated Data, and Removing Drift Effects	23

2.6	Patents on the Microwave Microscope	25
3	Quantitative Sheet Resistance Imaging	27
3.1	Introduction	27
3.2	A Model For the System	27
3.3	Calibration Using a Variable-Thickness Aluminum Thin Film . . .	32
3.4	Imaging the Microwave Sheet Resistance of a $\text{YBa}_2\text{Cu}_3\text{O}_{7-\delta}$ Thin Film	36
3.5	Sheet Resistance Sensitivity	39
4	High-Resolution Dielectric Imaging	42
4.1	Introduction	42
4.2	Changes to the Microscope Apparatus	43
4.3	Physical Description of the Measurement	44
4.4	Spatial Resolution	45
4.5	Effect of Contact on the Probe Tip and Sample	48
4.5.1	Damage to the Probe Tip	48
4.5.2	Damage to the Sample	50
5	A Physical Model for Dielectric Imaging	52
5.1	Introduction	52
5.2	Modeling the Fields Near the Probe Tip	53
5.2.1	Model Geometry	53
5.2.2	The Finite Element Model Equations	56
5.3	Calculating Frequency Shift From Perturbation Theory	59
5.4	Bulk Sample Imaging	61
5.5	Thin Film Imaging	64

5.6	Other Microscope Issues, Using the Model	66
5.6.1	Spatial Resolution	66
5.6.2	Permittivity Tensor Directional Sensitivity	68
5.6.3	Spherical Approximation for the Probe Tip	72
5.7	Images of a (Ba,Sr)TiO ₃ Thin Film	75
5.8	Sensitivity to Permittivity	78
6	Nonlinear Dielectric Imaging	79
6.1	Introduction	79
6.2	Measuring Dielectric Nonlinearity	80
6.3	Quantitative Dielectric Nonlinearity	85
6.4	Nonlinear Dielectric Images	88
6.5	Other Methods of Applying a Bias	90
6.6	Sensitivity to Dielectric Nonlinearity	91
7	Imaging of Domains in Ferroelectric Crystals	92
7.1	Introduction	92
7.2	Determining the Sign of Polarization	94
7.3	Ferroelectric Domain Images	98
7.3.1	Lithium Niobate	98
7.3.2	Barium Titanate	100
7.3.3	Deuterated Triglycine Sulfate	100
8	Critical Phenomena in Deuterated Triglycine Sulfate Crystals	107
8.1	Introduction	107
8.2	Changes to the Experiment	108
8.3	Critical Phenomena in the Permittivity of DTGS	110

8.3.1	Measurement Technique	110
8.3.2	Thermodynamic Theory and Curie Constants	113
8.3.3	Critical Slowing Down of Dielectric Response	117
8.4	Dielectric Nonlinearity	119
8.5	Ferroelectric Domain Structure Relaxation Time	121
9	Summary and Future Work	129
9.1	Summary	129
9.2	Future Work	130
9.2.1	Improvements to the Scanning System	130
9.2.2	Making Dielectric Loss Measurements	131
9.2.3	Further Investigation of Dielectric Measurements	133
9.2.4	Improving the Spatial Resolution	133
9.3	Conclusion	134
A	Input Impedance to a Conducting Thin Film Sample	136
B	Disentangling Sheet Resistance and Topography	139
B.1	Introduction	139
B.2	Description of the Disentangling Algorithm	140
C	Microwave Microscope Operating Procedure	144
C.1	Introduction	144
C.2	Setting up the Experiment	145
C.2.1	Components	145
C.2.2	Getting the Feedback Circuit Locked	145
C.2.3	Optimizing the Feedback Settings	149

C.3	Using the Runtime software	149
C.3.1	Loading a Configuration	150
C.3.2	Dependent Variable Settings	150
C.3.3	Independent Variable Settings	151
C.3.4	The Control Panel	152
C.3.5	Setting the Probe Height	153
C.3.6	Setting Scan Parameters and Running the Scan	154
C.3.7	Saving Your Data	155
C.4	Using Transform to View Your Data	156
C.5	Other Information	157
C.5.1	Re-establishing Your GPIB Connected With the Motor Con- troller	157
C.5.2	Viewing Images in Runtime	157
C.5.3	Adjusting the Tilt of the Sample and Probe	158
C.6	Additional Capabilities of Runtime	159
C.6.1	Z-Axis Slow Approach	159
C.6.2	Recording Scaled Data	160
C.6.3	Step Scans	160
C.6.4	Taking Background Data	161
C.6.5	Bidirectional Scans	161
C.6.6	Hysteresis Scans	162
C.6.7	Scans at Multiple Frequencies	163

Bibliography	164
---------------------	------------

LIST OF TABLES

1.1	Summary of materials property measurement techniques	3
5.1	Microwave vs. dc permittivity in dielectric thin films	65
C.1	List of components for the microwave microscope	147

LIST OF FIGURES

2.1	Schematic of the microscope	8
2.2	Reflected signal from the resonator vs. frequency	9
2.3	Photograph of the experimental apparatus.	11
2.4	Close-up view of the probe and sample holder.	12
2.5	Close-up of the STM tip probe and sample holder	15
2.6	Graphs illustrating how the frequency-following circuit works . . .	17
2.7	Transmission and reflection resonance curves	20
2.8	Resonator Q calibration curve.	24
3.1	Transmission line model for the microwave microscope.	28
3.2	Variable-thickness aluminum calibration sample.	33
3.3	Frequency shift and Q vs. height and sample sheet resistance. . .	34
3.4	Images of a $\text{YBa}_2\text{Cu}_3\text{O}_{7-\delta}$ thin film.	37
3.5	DC sheet resistance measurements of the $\text{YBa}_2\text{Cu}_3\text{O}_{7-\delta}$ thin film. .	40
4.1	Scan of aluminum lines	46
4.2	Scan of aluminum lines buried under a dielectric	47
4.3	High resolution images of probe tips	49
4.4	Evidence that the probe tip does not scratch the sample in contact	51
5.1	Diagram of the model calculation	54

5.2	A grid element and the four adjacent elements	55
5.3	Model results for the electric field near the probe tip	60
5.4	Frequency shift vs. permittivity ϵ_r for bulk samples	63
5.5	Thin film perturbation model	64
5.6	Spatial resolution as a function of sample permittivity	67
5.7	Permittivity tensor directional sensitivity	69
5.8	Electric field near the probe tip for anisotropic dielectric samples .	70
5.9	Frequency shift vs. permittivity for anisotropic dielectrics	71
5.10	Model using a sphere for the probe tip	73
5.11	Cross-sectional schematic of a $\text{Ba}_{0.6}\text{Sr}_{0.4}\text{TiO}_3$ thin film sample . .	76
5.12	Permittivity images of a $(\text{Ba},\text{Sr})\text{TiO}_3$ thin film	77
6.1	Schematic showing nonlinear dielectric measurement	81
6.2	The low-frequency electric field in a thin film	83
6.3	Dielectric nonlinearity at one point on a thin film	84
6.4	Quantitative dielectric nonlinearity at one point on a thin film . .	86
6.5	Nonlinear dielectric images of a BST thin film	89
7.1	Schematic of the periodically-poled LiNbO_3 crystal	95
7.2	Hysteresis loops in LiNbO_3	96
7.3	Images showing domains in a ferroelectric LiNbO_3 crystal	99
7.4	Image showing domains in a BaTiO_3 crystal	101
7.5	Domain images of DTGS, showing the change in domains over time	102
7.6	Domain image of a large area of a DTGS crystal	104
7.7	Switching a ferroelectric domain in a DTGS crystal	105
8.1	Side view of the sample holder with a heater stage	108

8.2	Hysteresis loops in DTGS	111
8.3	Permittivity vs. temperature in DTGS	112
8.4	Critical slowing down of dielectric response in TGS	118
8.5	Dielectric nonlinearity vs. temperature in DTGS	120
8.6	Permittivity function ξ as a function of electric field	122
8.7	Domain formation in DTGS at 330 K.	124
8.8	Domain formation in DTGS at 320 K.	125
8.9	Ferroelectric domain relaxation times for DTGS	127
A.1	Input impedance to a conducting thin film sample	137
B.1	Surface plots to disentangle sample sheet resistance and topography	141
B.2	Images of topography and sheet resistance of a $\text{YBa}_2\text{Cu}_3\text{O}_{7-\delta}$ thin- film sample	142
C.1	Microwave microscope circuit diagram	146

Chapter 1

Introduction

1.1 Overview of Microwave Measurements

Recently, microwave microscopy has entered the diverse scene of materials property measurement techniques. As computer chip and wireless communication industries expand, the demand has grown for measurement techniques that go beyond the ability of currently established methods. For example, higher computer clock speeds, as well as the cellular industry's reliance on microwave communication, have shifted the demand toward measurements at higher frequencies than were previously required.

In addition, as our understanding of the fundamental physics of materials increases, new measurement techniques are needed to probe further into the fundamental properties of materials. Ferroelectric and paraelectric materials, in particular, are at the forefront of materials science research today. However, many of the established measurement techniques are destructive to samples, and do not allow spatially resolved imaging. Other common methods are restricted to frequency ranges which are easier to work with experimentally, namely, low frequencies ($\lesssim 1$ MHz) or optical frequencies. Only in the last few years have some

new forms of microwave measurement come into practice; this trend is toward near-field measurement techniques.

Far-field measurements, such as optical photography with a camera or optical microscopy, are limited in spatial resolution to the Abbé limit [2] of half the wavelength ($\lambda/2$) of the incident radiation. In contrast, near-field measurements [8, 109], accomplished by bringing a probe to within a wavelength of the sample, have no such limitation. In the near field, the spatial resolution is generally equal to the size of the probe. For example, at 10 GHz, the wavelength is 3 cm, much larger than the size of many interesting samples. Far-field measurements in this case would have a resolution of about 3 cm, which is clearly not useful for the typical sample. On the other hand, by using a tiny probe in the near field, spatial resolutions of 1 μm or better [$\lambda/(3 \times 10^4)$] can be achieved. The main disadvantage with near-field measurements, however, is that a “snap shot” is no longer possible; instead, the probe must be raster-scanned across the sample, which can be time-consuming.

An overview of quantitative materials property measurement techniques is given in Table 1.1, with a focus on those that can measure sheet resistance and/or permittivity. Several advantages of near-field techniques over far-field techniques are evident from Table 1.1. Near-field measurements are non-destructive, for example, and allow imaging. They are also readily used at microwave frequencies, which is often not the case for traditional techniques.

In Table 1.1, our microscope, the Near-Field Scanning Microwave Microscope (NSMM) stands out for its versatility. The same type of instrument has been used for imaging conductors [92, ?, ?], dielectrics [94, ?], magnetic materials [64], and superconductors [9, ?]. It also has been used to image electric [32, ?, ?] and

Far-Field Techniques	Sample properties	Bulk (B) / Thin film (TF)	Spatial resolution (μm)	Non-destructive	Can image	Broad-band	Frequency range
Cavity perturbation [31, 57, 60, 83]	R, ϵ_r	B	Whole sample	yes	no	no	0.1–20 GHz
Confocal resonator [12, 43, 47, 50, 68]	R, ϵ_r	B, TF	0.5–1000	yes	yes	no	20 GHz–Optical
Dielectric resonator [34, 37, 86, 120]	R, ϵ_r	TF	5000	yes	yes	no	> 10 GHz
Parallel-plate resonator [77, 97, 102]	R, ϵ_r	B (ϵ_r), TF (R)	Whole sample	no	no	no	1–50 GHz
Propagation constant from transmission line [22, 35, 118]	ϵ_r	TF	10^4	no	no	yes	0.1–50 GHz
Waveguide transmission [14, 119, 123]	ϵ_r	B	Whole sample	yes	no	yes	0.1–50 GHz
Near-Field Techniques							
Thin film capacitors [13, 41, 72]	ϵ_r	B, TF	1000	no	no	yes	$\lesssim 1$ MHz
Microwave reflection; Corbino [17, 19, 20, 53, 67, 74, 112]	R, ϵ_r	B, TF	2000	no	no	yes	0–50 GHz
Coaxial cavity [24, 39, 40]	R, ϵ_r	B, TF	0.1–250	yes	yes	no	~ 1 GHz
Microstrip resonator [98, 99]	R, ϵ_r	B, TF	0.4–300	yes	yes	no	~ 1 GHz
Waveguide resonator [42, 63]	R	B, TF	20–50*	yes	yes	no	~ 100 GHz
Lumped element resonator [25, 26]	ϵ_r	TF	0.01	yes	yes	no	~ 1 GHz
NSMM [92–95, 111]	R, ϵ_r	B, TF	1–500	yes	yes	yes**	0.1–50 GHz

*20–50 μm resolution achieved after image processing

**Broadband capability using phase shifter in the resonator

Table 1.1: Summary of materials property measurement techniques that can quantitatively measure sheet resistance (R) or dielectric permittivity (ϵ_r).

magnetic fields above operating microwave devices. The available spatial resolutions span three orders of magnitude. It also has broadband capability, when a commercially-available phase shifter is used in the resonator to continuously vary its length.

1.2 Motivation for the Experiment

The motivation for the work described in this dissertation is as follows. First, we wanted to use the microwave microscope to make quantitative measurements. Previous work on near-field microwave microscopy was mainly qualitative, with an emphasis on spatial resolution improvement at the expense of quantitative understanding of contrast mechanisms. Two very different physical properties were chosen: sheet resistance and permittivity. Developing the quantitative measurement capacity required an additional level of understanding of the physical mechanisms involved in the interaction between the microscope and the sample, which was achieved through physical models for the system.

Second, we wanted to use the microscope to investigate the fundamental physics of materials. We chose ferroelectric materials, because this is an active area of research today. It was possible, for example, to image ferroelectric domains, and observe how domain structure and permittivity changed with temperature in the vicinity of the critical temperature.

1.3 Outline of Dissertation

This dissertation describes the accomplishment of the goals listed above. This work involved many new aspects of microwave microscopy that were previously

undeveloped or unstudied.

In Chapter 2, I describe the experimental apparatus of the microwave microscope, including both non-contact and contact mode imaging. I discuss the frequency-following circuit which is used to perform the measurement, and describe the measurement of the Q of the microscope resonator. Finally, I discuss the initial requirements for quantitative imaging with the microscope.

In Chapter 3, I describe the first of two forms of quantitative imaging: the sheet resistance of conducting thin films. I discuss a theoretical model for the system to reinforce our understanding of the physical mechanisms involved. Results are presented for a variable-thickness conducting thin film sample, and are compared with an independent dc measurement of the sheet resistance.

In Chapter 4, I describe the second form of imaging, which is the imaging of dielectrics in contact mode. In this chapter, I focus on the requirements for this form of imaging, and demonstrate that the spatial resolution is about $1\text{ }\mu\text{m}$. Also discussed is an investigation of damage to the probe tip and sample in contact mode.

In Chapter 5, I describe a physical model for the electric field near the probe tip based on a finite-element calculation, for imaging dielectric samples. This model is used to make quantitative measurements of permittivity. Using the model, I also investigate the spatial resolution of the microscope, the directional sensitivity to the permittivity tensor, and an alternative type of model for the system using an analytic calculation. As a demonstration of quantitative imaging, I present results from scanning a (Ba,Sr)TiO₃ thin film sample.

In Chapter 6, I describe nonlinear dielectric imaging. For thin films, dielectric nonlinearity can be measured quantitatively. Resulting images are presented for

a (Ba,Sr)TiO₃ thin film sample.

In Chapter 7, I describe the imaging of domains in ferroelectric crystals. This method can be used to observe domain dynamics. Images are presented for LiNbO₃, BaTiO₃, and deuterated triglycine sulfate crystals.

In Chapter 8, I describe an investigation of critical phenomena in deuterated triglycine sulfate crystals. Behavior of permittivity as a function temperature shows reasonable agreement with thermodynamic theory. Critical slowing down of the dielectric response can also be seen, as well as a maximum in the dielectric nonlinearity at the Curie temperature. Also, the relaxation time of the crystal's domain structure is observed as a function of temperature.

In Chapter 9, I give a summary of the capabilities of the microscope which have been described in this dissertation. I also give a description of future work that could be done with the near-field scanning microwave microscope.

Chapter 2

Description of the Experiment

2.1 Overview of Experimental Apparatus

The near-field scanning microwave microscope [92,93] (NSMM, see Fig. 2.1) consists of a microwave resonator contained in a coaxial transmission line. One end of the resonator is coupled via a coupling capacitor to a microwave source, while the other end of the resonator consists of an open-ended coaxial probe. Bringing a sample near the open end of the probe perturbs the microwave fields at the probe tip, resulting in a perturbation to the boundary condition at the probe end of the resonator.

An example of the reflected signal from the resonator as a function of frequency is shown in Fig. 2.2. The minima in the reflected signal are the resonant frequencies of the microscope resonator. The spacing between the minima depend on the length of the resonator. For a resonator with a length of 25 cm, the resonances are spaced approximately 500 MHz apart. Without a sample near the probe, the curve looks like the solid curve in Fig. 2.2. However, when a sample, such as a piece of metal, is brought near the probe tip, the resonator is perturbed so that the result resembles the dotted curve in the figure. The resonant frequen-

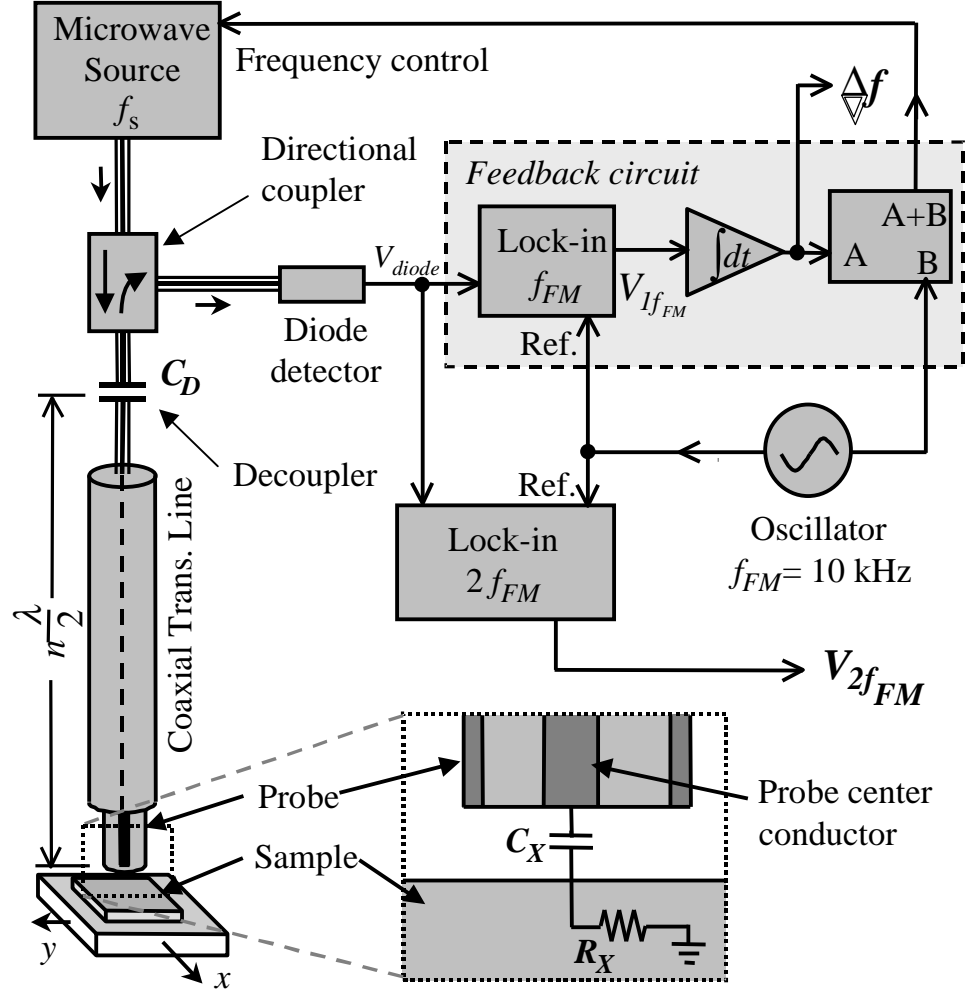


Figure 2.1: Schematic of the near-field scanning microwave microscope.

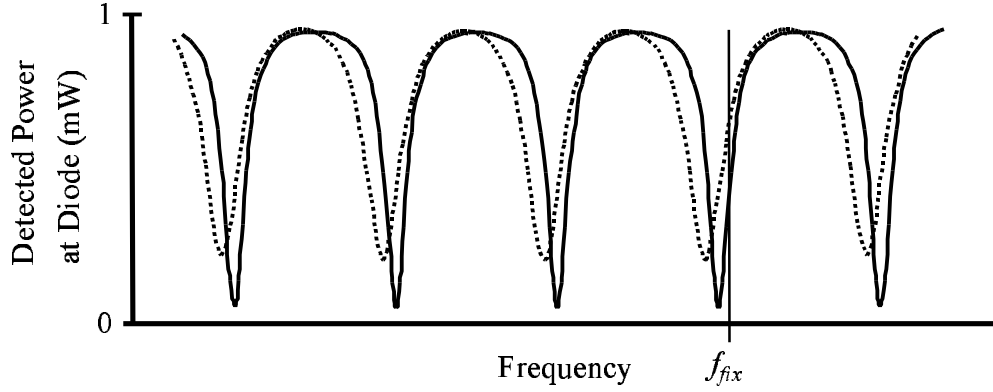


Figure 2.2: The reflected signal from the resonator as a function of frequency. The solid line represents the unperturbed resonator, while the dotted line represents the resonator with a sample beneath the probe.

cies are shifted downward, as the boundary condition at the probe end of the resonator moves from an open circuit toward a short circuit. Also, the minima are broadened, due to losses in the sample, and hence, a lowering of the Q of the resonator. For a metallic sample, the frequency shift is mainly a function of the separation between the probe and the sample, while the Q is mainly a function of the sheet resistance or surface resistance [92].

The reflected microwave signal from the resonator is sent to a diode detector using a directional coupler. The diode detector outputs a voltage which is proportional to the incident microwave power. The diode detector output signal is the input to a frequency-following feedback circuit (see section 2.3), which keeps the microwave source locked onto the selected resonant frequency of the microscope resonator. Two outputs of the feedback circuit are the resonant frequency shift Δf and the $V_{2f_{FM}}$ of the resonator.

An image is obtained by raster scanning the sample in x and y beneath the probe, while recording Δf and Q . After scanning, the data can be viewed in a false-color image.

Photographs of the system are shown in Figs. 2.3–2.4. Figure 2.3 is a photograph of the scanning apparatus. The sample holder, which is hidden, is attached to a tilt table, which is on top of a two-axis translation stage. The probe and resonator are fixed to a z-axis translation stage, which is held in place by the probe support apparatus. A video camera and binocular microscope allow two ways of viewing the probe and sample. Figure 2.4 is a close-up view of the probe and sample holder. The spring-loaded sample holder, which will be described in the next section, is shown here.

The entire system is on top of a vibration isolation table to isolate it from vibrations in the floor of the room. I also built a Plexiglass enclosure which surrounds the microscope apparatus, protecting it from gusts of wind, for example. Another benefit of the enclosure is that the interior environment is isolated from the environment of the room, so that the temperature inside is more stable. This greatly reduced thermal drifts in the probe support structure, which previously caused the probe’s position relative to the sample to shift with time (see Sec. 4.2).

2.2 Comparison between Non-Contact and Contact Modes

The microscope has two modes for materials imaging: non-contact mode and contact mode. In non-contact mode, the probe is held fixed above a planar

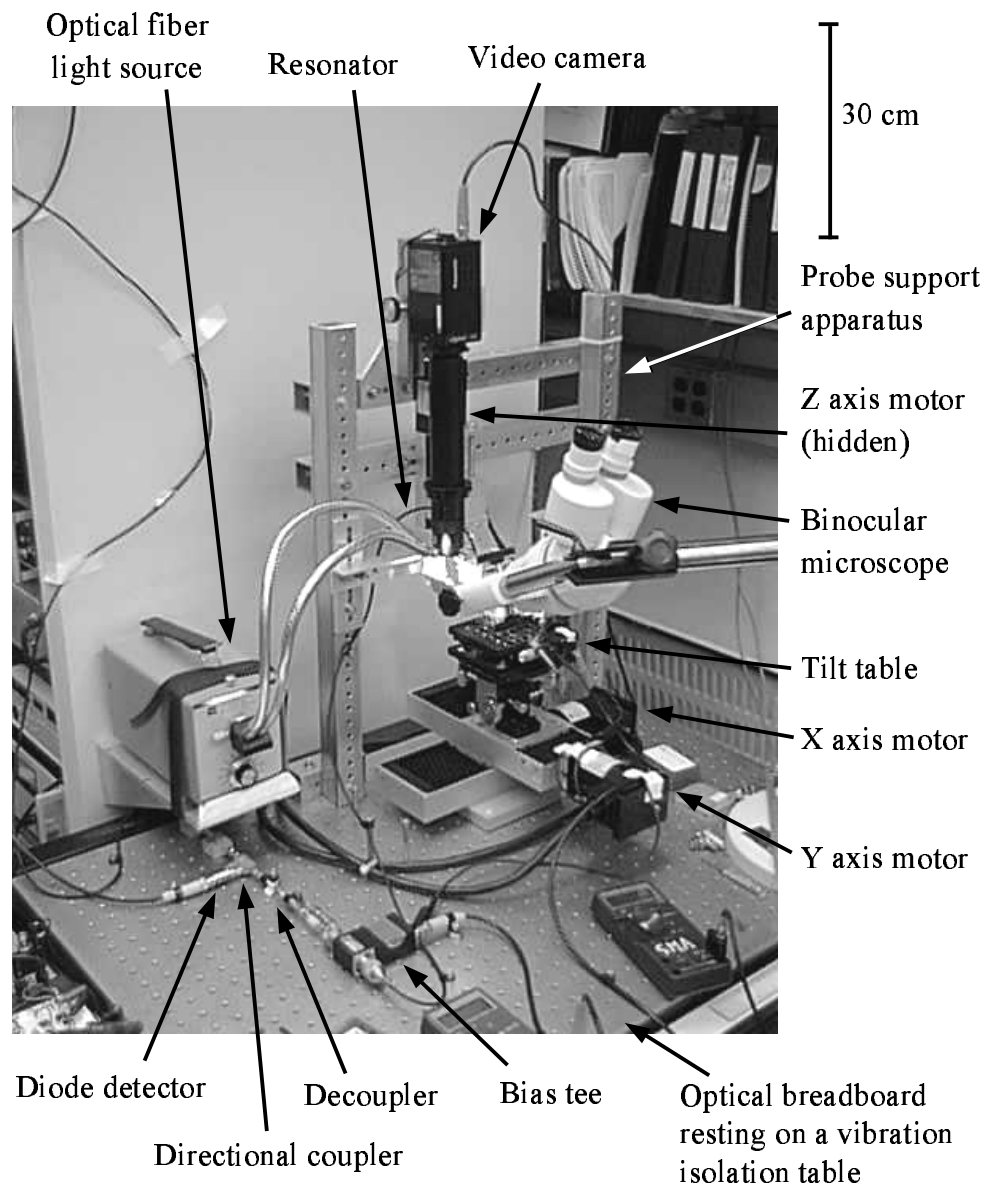


Figure 2.3: Photograph of the experimental apparatus.

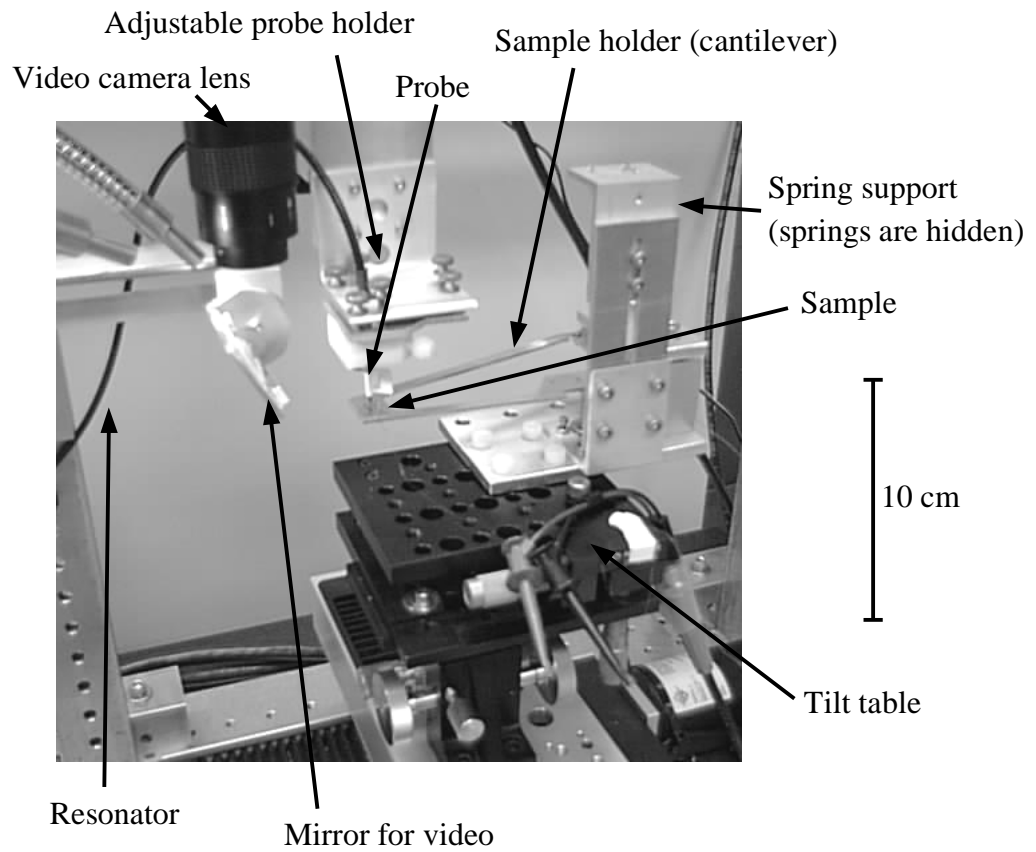


Figure 2.4: Close-up view of the probe and sample holder.

sample (see the inset to Fig. 2.1). In this mode, the spatial resolution depends on the larger of two quantities: the separation between the probe and the sample (h), and the diameter of the probe's center conductor (d_{cc}). The strongest coupling between the resonator and the sample is obtained for $h \ll d_{cc}$. All of the non-contact imaging described in this dissertation is in this limit, giving a spatial resolution which is approximately equal to the probe center conductor diameter [10, 109, 111].

The disadvantage of non-contact mode is that the sample must be planar. Also, the tilt of the sample surface must be adjusted so that the top surface of the sample is parallel to the scanning axes; this can be a tedious operation which can take longer than the actual scanning. The advantage is that non-contact scanning can be very fast: a 2" wafer can be scanned at a speed of 25 mm/s, with a spatial resolution of 0.5 mm, in about 10 minutes [92]. Another problem with non-contact mode is that fluctuations in the probe-sample separation (h) will occur due to nonlinearity in the scanning mechanism, and also due to vibrations. Thus, h must be significantly greater than these fluctuations to minimize noise in the data. Because the probe-sample separation should be less than the center conductor diameter ($h \ll d_{cc}$), d_{cc} cannot be too small. This, in turn, limits the maximum spatial resolution which can be obtained in non-contact mode. With our scanning system with stepper motor-driven translation stages, vibration and non-linearity in the stages require that the probe-sample separation be at least $\sim 30 \mu\text{m}$ for large-area ($\gtrsim 1 \text{ cm}^2$) scans.

Effects due to sample topography (and scanning stage non-linearity) can in fact be eliminated from the data by applying a disentangling algorithm to extract a sample property (such as sheet resistance) and probe-sample separation from

the two microscope outputs, Δf and Q . This capability has been demonstrated with a conducting thin-film sample [6].

The second mode of operation of the microscope is contact mode (see Fig. 2.5). In this mode, the probe tip is held in gentle contact with the sample. This is accomplished in our system by holding the probe fixed, and placing the sample on a spring-loaded cantilever. Using soft springs mounted near the cantilever's pivot axis, the spring constant at the sample can be smaller than 2 N/m. If the sample is compressed 30 μm by the probe, this gives a force smaller than 60 μN .

There are several advantages to contact mode. First, sample topography no longer has an effect on the measurement. Also, the spatial resolution can be much higher than in non-contact mode. This is accomplished by extending the probe's center conductor beyond the outer conductor, and bringing the tip to a sharp point. In our system (see Fig. 2.5), the center conductor extension is a thin, sharp-tipped tungsten wire such as the kind used in scanning tunneling microscopy (STM). The probe is constructed by removing the center conductor of the coaxial cable, and replacing it with a tube with approximately the same outer diameter as the center conductor. The STM tip fits inside this tube. Bending the STM tip slightly creates enough friction to hold the STM tip in place. The tip extends beyond the outer conductor by 1–1.5 mm so that it can be removed with tweezers. Easy tip removal is important, because the fragile tips are easily damaged, and often need to be replaced. Using commercial STM tips made of tungsten [66], we have shown the spatial resolution of the microscope to be about 1 μm [33, 94].

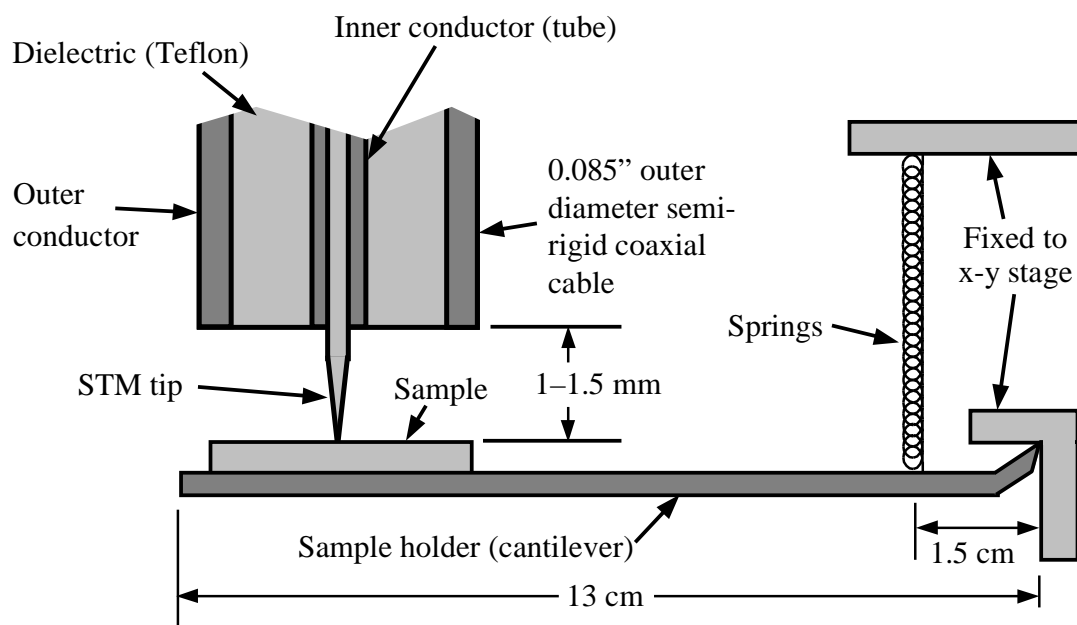


Figure 2.5: Close-up view of the STM tip probe and sample holder. Drawing is not to scale.

2.3 The Frequency-Following Circuit

In the original NSMM system, scanning was performed at a fixed frequency [110]. By selecting a frequency f_{fix} (Fig. 2.2) near a resonance, where there is a large slope in the reflected signal vs. voltage curve, one could observe contrast in the reflected signal V_{diode} while scanning a sample. However, one could not distinguish between changes in the resonant frequency and changes in Q . Thus, it was necessary to invent a frequency-following feedback circuit [11, 92, 93] in order to measure both Δf and Q (see Fig. 2.1).

In order to measure changes in the resonant frequency, the feedback circuit keeps the microwave source locked onto the selected resonance. The microwave source frequency is modulated at a rate $f_{FM} = 10$ kHz. The diode detector signal V_{diode} is sent to the f_{FM} lock-in amplifier, which extracts the component of V_{diode} at f_{FM} . The f_{FM} lock-in output signal ($V_{1f_{FM}}$) depends on the location of f_s , the microwave source frequency, relative to the resonance frequency f_0 , as illustrated in Fig. 2.6. Figure 2.6(a) shows a typical $-V_{diode}$ vs. frequency curve near a resonant frequency f_0 . (Note that V_{diode} is a negative voltage.) The frequency modulation reference signal (the output from the oscillator in Fig. 2.1) as a function of time is shown in Fig. 2.6(b). First, consider the case where f_s is below the resonant frequency f_0 , with $f_s = f_1$, as shown in (a). In this case, $-V_{diode}$ as a function of time will resemble the curve in (c). The output of the f_{FM} lock-in amplifier ($V_{1f_{FM}}$), which is the time-average of the product of the reference signal [Fig. 2.6(b)] and V_{diode} [Fig. 2.6(c)], is positive. On the other hand, if f_s is above the resonance, at f_2 in (a), $-V_{diode}$ as a function of time looks like the curve in (d), and $V_{1f_{FM}}$ is negative. Finally, if f_s is on resonance ($f_s = f_0$), $-V_{diode}$ vs. time looks like (e), and $V_{1f_{FM}} = 0$ V because the curve in

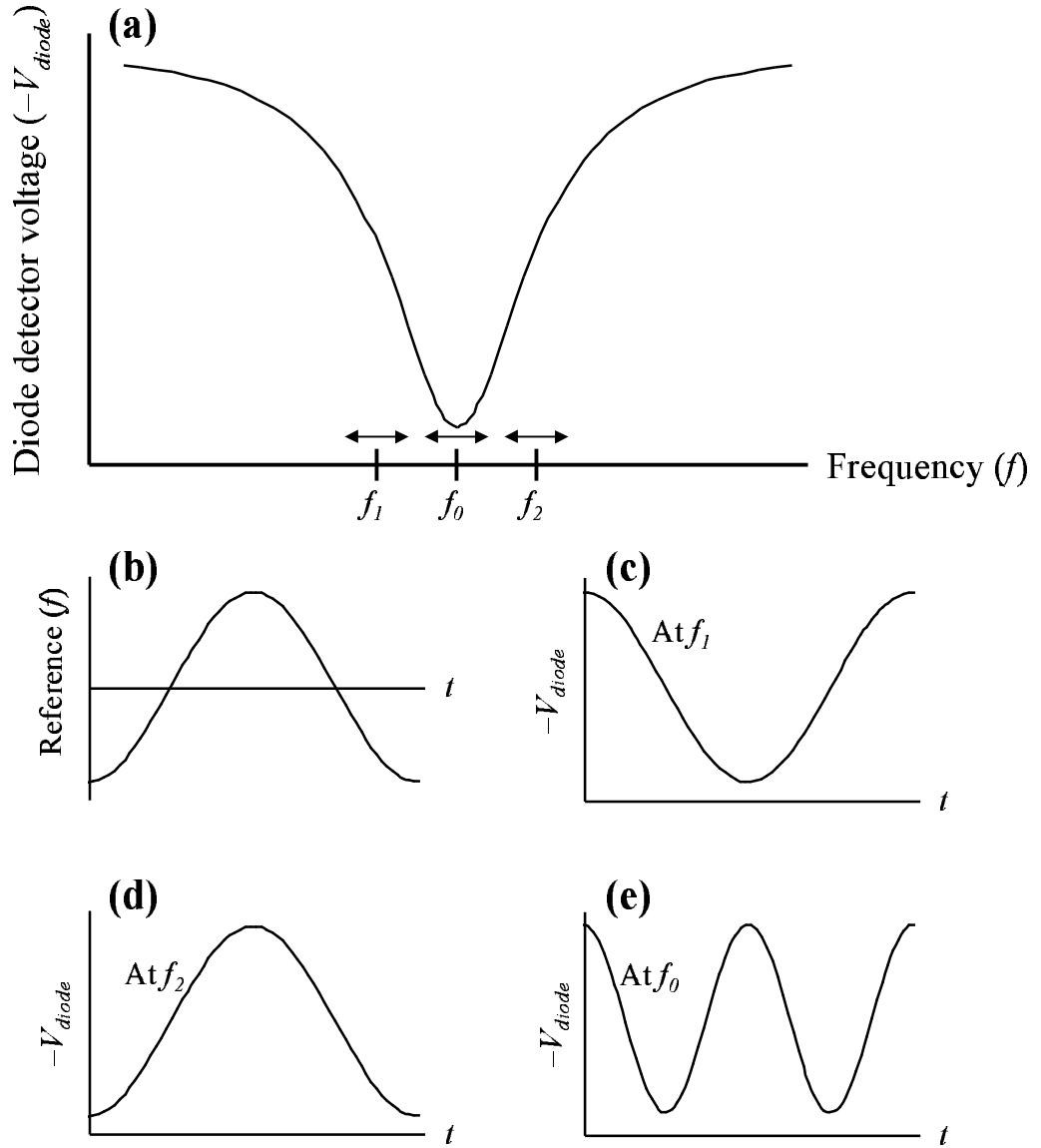


Figure 2.6: Graphs illustrating how the frequency-following circuit works. (a) The diode detector voltage ($-V_{diode}$) as a function of microwave source frequency f_s . (b) The oscillator reference signal as a function of time. The V_{diode} signal as a function of time is shown (c) below the resonance, (d) above the resonance, and (e) on resonance.

(e) is at twice the reference frequency. Thus, $V_{1f_{FM}}$ indicates the position of f_s relative to the resonant frequency f_0 .

The signal $V_{1f_{FM}}$ is sent to a time integrator, which adjusts its output upward or downward with time depending on the sign of $V_{1f_{FM}}$. This integrator output is in fact the error signal of the feedback, or the frequency shift signal Δf . The error signal is then added to the oscillator signal with frequency f_{FM} , and sent to the microwave source FM input, completing the feedback loop. This signal has a dc component which is equal to the error signal, and an ac component which causes the microwave source to frequency modulate.

The locked V_{diode} signal oscillates at frequency $2f_{FM}$. The amplitude of this sinusoidal signal is proportional to the curvature (second derivative) of the V_{diode} -vs.-frequency curve on resonance. This curvature is related to the Q of the resonator (see Sec. 2.4), and can be measured using a second lock-in amplifier referenced at $2f_{FM}$.

Thus, two quantities can be measured and recorded while scanning the sample: the frequency shift signal (Δf), and the “2f” signal, $V_{2f_{FM}}$, which is related to the Q of the resonator.

2.4 Measuring the Q of the Resonator

2.4.1 The General Idea

There is a one-to-one relationship between $V_{2f_{FM}}$ and Q . To determine this relationship, we need to be able to calculate the Q of the resonator, which can be accomplished by measuring the reflection coefficient of the resonator as a function of frequency, as described in the following sections. Once we have determined

the values of Q for several different values of $V_{2f_{FM}}$, a linear fit allows us to find a function to convert any value of $V_{2f_{FM}}$ to its corresponding Q value.

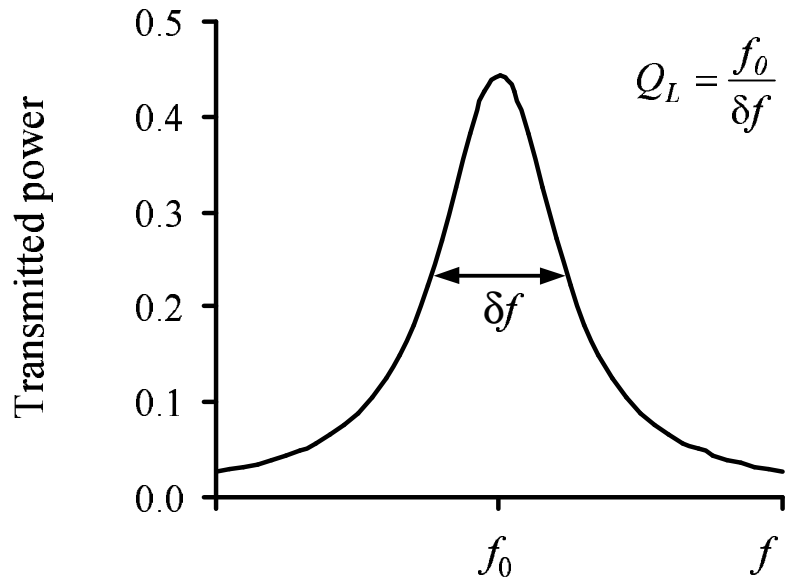
2.4.2 Finding the Reflection Coefficient

To calculate the Q of the microscope resonator, first the system must be calibrated to allow measurement of the reflection coefficient $|\rho|^2$ at the resonator input. The reflection coefficient is defined as $|\rho|^2 = P_r/P_i$, where P_i is the incident power, and P_r is the reflected power. To define the scale for $|\rho|^2$, we first replace the resonator with a short circuit at approximately the location where the coupling capacitor will be. Next, we sweep the microwave source frequency through the resonance of interest, recording V_{diode} as a function of frequency. This V_{diode} data defines the full-scale reflected signal, which is a function of frequency. Future V_{diode} data with the resonator in place is divided by the full-scale V_{diode} data, to obtain $|\rho|^2$.

2.4.3 Calculating Q from the Width of a Resonant Minimum

For resonators which are measured in transmission, the transmitted power-vs.-frequency curve is a maximum at its resonant frequencies [Fig. 2.7(a)]. Measuring the Q of such a resonator is accomplished by simply taking the full-width at half-maximum (δf) along this curve, and dividing it by the resonant frequency: $Q = \delta f/f$. In the case of our resonator which is measured in reflection [4, 61], the situation is more complicated. In this case, the curve has a minimum on resonance instead of a maximum [Fig. 2.7(b)]. The value of $|\rho|^2$ where we measure the width of the resonant minimum (which we will call $|\rho_1|^2$) is now a function

(a)



(b)

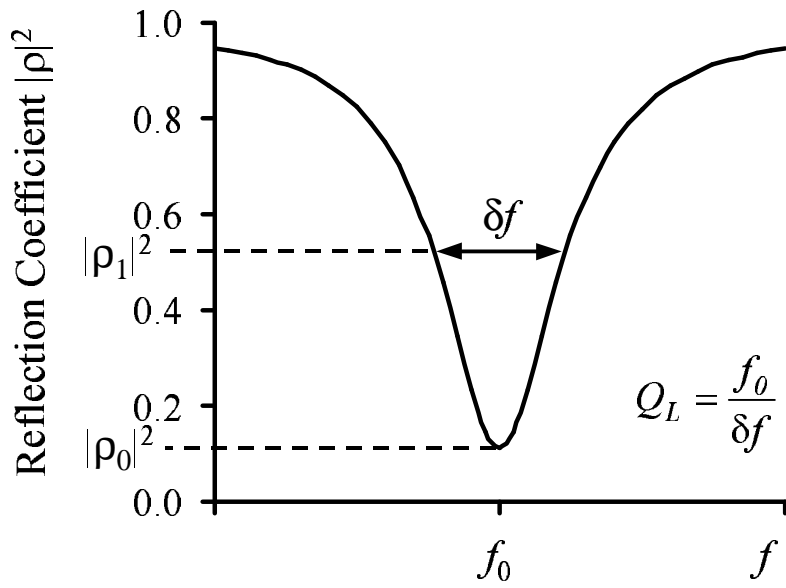


Figure 2.7: Resonance curves for a resonator measured in (a) transmission and (b) reflection.

of the coupling of the microwave input to the resonator. Only in the special case where the resonator is critically coupled does $|\rho_1|^2 = 0.5$, like in the case of a resonator measured in transmission.

The coupling coefficient (β) defines the coupling to the resonator through the coupling capacitor. A critically-coupled resonator has $\beta = 1$, while an undercoupled resonator has $0 < \beta < 1$, and an overcoupled resonator has $\beta > 1$. For the case of an undercoupled resonator, the parameter β is found by measuring the reflection coefficient on resonance, and calculating

$$\beta = \frac{1 - |\rho_0|}{1 + |\rho_0|}, \quad (2.1)$$

where ρ_0 is the reflection coefficient on resonance. For an overcoupled resonator, β is equal to the inverse of Equation 2.1.

Determining whether a resonator is undercoupled or overcoupled can be difficult. The most reliable way is to connect the resonator to a properly-calibrated network analyzer [61]. With the display in Smith Chart mode, the resonances will form circles on the display. With a perfect calibration (the plane of the calibration being exactly at the resonator coupling capacitor, which is difficult to achieve), the resonances will appear as circles which are centered on the horizontal axis, at or to the right of the origin. If the plane of the calibration is not exactly at the coupling capacitor, the circle will be rotated by some angle about the origin. The curve for an overcoupled resonance will encircle the origin of the Smith Chart, while the curve for an undercoupled resonance will not. Coupling is a function of frequency; if a resonator is critically coupled at a frequency f_0 , then we have found that the resonator will be undercoupled for frequencies $f < f_0$, and overcoupled for $f > f_0$.

Using the value for β as calculated in equation 2.1, we then calculate $|\rho_1|^2$:

$$|\rho_1|^2 = \frac{1 + \beta^2}{(1 + \beta)^2}. \quad (2.2)$$

The quantity δf is defined as the width of the resonance curve at $|\rho|^2 = |\rho_1|^2$.

Then the loaded Q is calculated as

$$Q_L = \frac{\delta f}{f}. \quad (2.3)$$

The unloaded Q , which would be the Q of the resonator with no coupling ($\beta \rightarrow 0$), is then

$$Q_0 = (\beta + 1)Q_L. \quad (2.4)$$

2.4.4 Calculating Q Using a Curve Fit

A better way calculate the Q of the resonator involves a curve fit to a theoretical function for $|\rho(f)|^2$. This method can be more accurate, because it is less sensitive to imperfections in the resonator, which distort the shape of the resonance. By fitting a curve to a narrow band of frequencies near f_0 , distortions to the resonances have a reduced effect. The theoretical curve for a resonator measured in reflection is [79]

$$|\rho(f)|^2 = \frac{\left[\frac{1}{Q_L} \left(1 - \frac{2}{1+\beta} \right) \right]^2 + \left(\frac{f_0}{f} - \frac{f}{f_0} \right)^2}{\left(\frac{1}{Q_L} \right)^2 + \left(\frac{f_0}{f} - \frac{f}{f_0} \right)^2}. \quad (2.5)$$

The resonant frequency f_0 is found from the minimum in the power-vs.-frequency curve. Then, β is calculated from $|\rho_0|^2$ using equation 2.1. Finally, Q_L is calculated by minimizing the error between equation 2.5 and the data.

2.4.5 The Q Calibration Process

There is a functional relationship between $V_{2f_{FM}}$ and Q_L for a given resonator. To determine this relationship, we vary the Q of the resonator by positioning a microwave absorber material near the probe tip. After plotting several points for different values of Q_L (see Fig. 2.8), we obtain a linear fit $Q_L(V_{2f_{FM}})$ to the data. In a typical scan, we measure $V_{2f_{FM}}$, and convert it to Q_L for recording. Only a small range of Q needs to be calibrated, as was done in Fig. 2.8, since the change in Q for a typical sample is less than 5%.

This calibration needs to be done only once for a given probe, as long as the probe tip is not altered or damaged. If any part of the resonator (its length, coupling, etc.) is changed, the Q calibration must be repeated.

2.5 Obtaining Calibrated Data, and Removing Drift Effects

To obtain quantitative data, it is necessary to establish an absolute scale for the microscope output signals. The absolute Δf signal depends on several factors in addition to the sample, including the frequency dial setting on the analog microwave source. The Δf signal also drifts with time, because of microwave source frequency drift. Thus, it is necessary to define Δf relative to some constant, in a way that can be repeated reliably with each new scan. For the microwave microscope, one method is to define $\Delta f = 0$ to be the case of the resonator with no sample present. Then, Δf will be the perturbation to the resonant frequency due to the sample.

Similarly, one must define an absolute scale for $V_{2f_{FM}}$, because $V_{2f_{FM}}$ depends

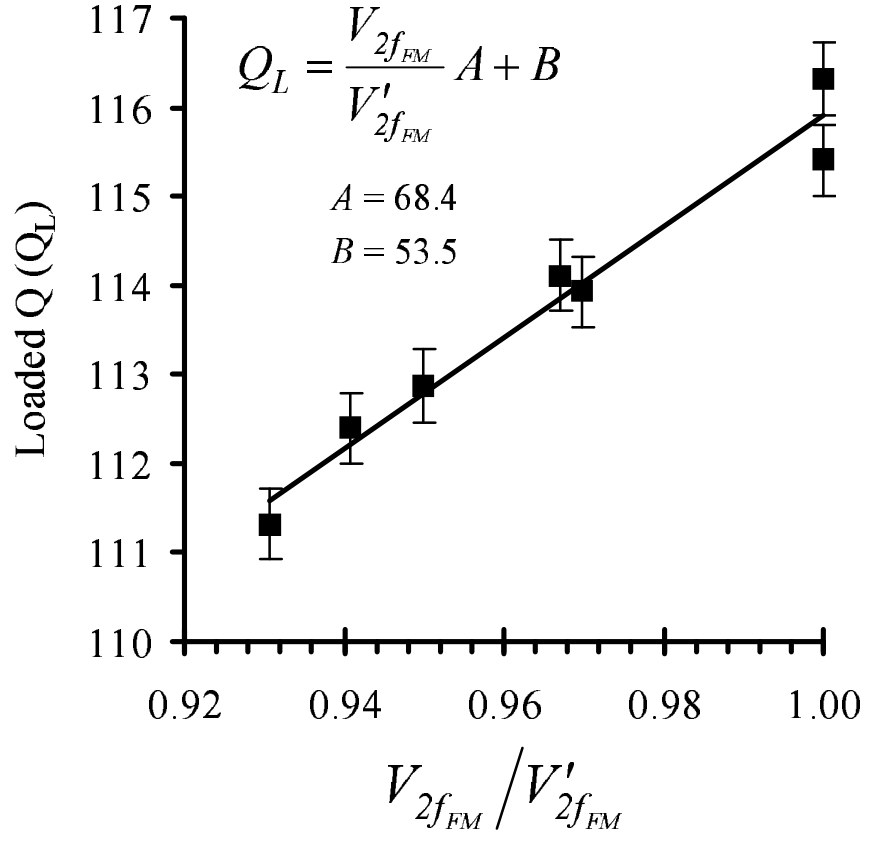


Figure 2.8: Resonator quality factor (Q) calibration curve, measured by positioning the probe at various heights above a microwave absorber. The quantity $V'_{2f_{FM}}$ is the $2f$ signal with no sample present near the probe.

on the power level setting of the microwave source, which is an analog dial. In addition, the power level drifts with time, making it important to define the absolute scale in a reliable manner, each time a scan is acquired. This purpose can be accomplished in the same way as it is for Δf : define $V'_{2f_{FM}}$ to be the full-scale value of $V_{2f_{FM}}$ with no sample present. Then, the Q of the resonator can be calculated as

$$Q_L(V_{\Delta f}) = \frac{V_{2f_{FM}}}{V'_{2f_{FM}}} A + B, \quad (2.6)$$

where A and B are determined from the $V_{2f_{FM}} \rightarrow Q_L$ calibration described in section 2.4.5. Examples of A and B are shown in Fig. 2.8.

Because of the problem of drifts in both Δf (due mainly to source frequency drift) and $V_{2f_{FM}}$ (due mainly to source power drift) during a scan, it is preferable to take background measurements before each scan line. This is accomplished by retracting the probe from the sample sufficiently far ($\gtrsim 3$ mm) that the sample no longer perturbs the resonator. This can be done before each scan line, to remove drifts that occur during a scan. I use this method for contact mode imaging of dielectrics, because of the greater length of time (~ 1 hour) required for many of these scans.

2.6 Patents on the Microwave Microscope

I am an inventor on three patent applications [6, 7, 11] regarding the microwave microscope, including one which has been issued, U.S. Patent No. 5,900,618. All three of these have been licensed by Neocera, Inc., of Beltsville, Maryland. Neocera is developing a commercial version of the microscope, EPSCANTM. In

these patents, further descriptions are given of the microscope apparatus and measurement techniques.

Chapter 3

Quantitative Sheet Resistance Imaging

3.1 Introduction

As a first step in quantitative imaging with the microwave microscope, we chose to image the sheet resistance of conducting thin films. In order to further our understanding of the interaction between the probe and the sample, we developed a physical model for the system. Quantitative imaging required a calibration standard. We tested our quantitative sheet resistance imaging method on a variable-thickness $\text{YBa}_2\text{Cu}_3\text{O}_{7-\delta}$ thin film sample.

3.2 A Model For the System

Using microwave transmission line theory [27, ?, ?], we developed a model for the microscope resonator and sample. The model is summarized in Fig. 3.1. Figure 3.1(a) shows a circuit diagram for the microwave source, directional coupler, and diode detector. The lumped input impedance to the resonator portion of the microscope is Z_{res} . We define the complex microwave source voltage and current

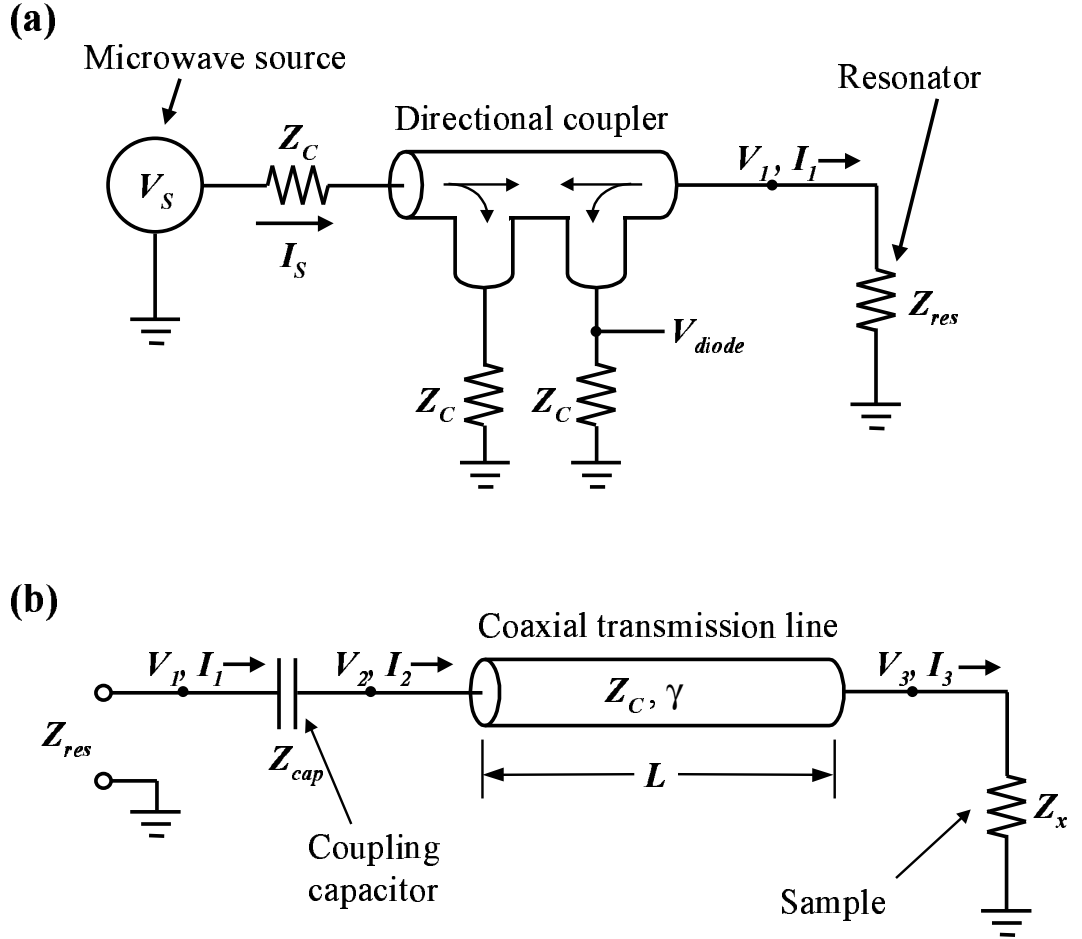


Figure 3.1: (a) A transmission line model for the microwave microscope. The resonator, represented as the effective impedance Z_{res} , is modeled as shown in (b).

to be

$$\begin{aligned} V_S &= e^{i\omega t} (V_S^+ + V_S^-) \\ I_S &= \frac{e^{i\omega t}}{Z_C} (V_S^+ - V_S^-), \end{aligned} \quad (3.1)$$

where ω is the frequency of the microwave source, and $Z_C = 50 \, \Omega$ is the characteristic impedance of the coaxial cables. The quantity V_S^+ is the amplitude of the wave traveling to the right in Fig. 3.1(a), while V_S^- is the amplitude of the wave traveling to the left. The output voltage of the microwave source is V_S^+ . We define the voltage and current at the input to the resonator to be

$$\begin{aligned} V_1 &= e^{i\omega t} (V_1^+ + V_1^-) \\ I_1 &= \frac{e^{i\omega t}}{Z_C} (V_1^+ - V_1^-). \end{aligned} \quad (3.2)$$

For the directional coupler, we define the coupling voltage fraction to be $\eta \equiv 10^{\zeta/20}$, where ζ is the coupling in dB. For our directional coupler with $\zeta = -6 \, \text{dB}$, η is approximately 0.5. The equations for the directional coupler are

$$\begin{aligned} V_1^+ &= V_S^+ (1 - \eta) \\ V_S^- &= V_1^- (1 - \eta) \\ V_{diode} &= -\eta V_1^-. \end{aligned} \quad (3.3)$$

Finally, we have

$$V_1 = I_1 Z_{res}. \quad (3.4)$$

Combining the above equations, eliminating V_S^- , and solving for V_{diode} , we obtain

$$V_{diode} = \left(\frac{Z_{res} - Z_0}{Z_{res} + Z_0} \right) \eta (1 - \eta) V_S^+. \quad (3.5)$$

The resonator portion of the circuit (Z_{res}) is shown in Fig. 3.1(b). The coupling capacitor impedance is

$$Z_{cap} = \frac{1}{i\omega C_{cap}}, \quad (3.6)$$

where C_{cap} is the coupling capacitance. We calculate Z_{res} as follows. We define the voltage and current at the coupling end of the resonator to be

$$\begin{aligned} V_2 &= e^{i\omega t} (V'_+ + V'_-) \\ I_2 &= \frac{e^{i\omega t}}{Z_C} (V'_+ - V'_-) . \end{aligned} \quad (3.7)$$

The coaxial transmission line in Fig. 3.1(b) is the only distributed element in the model. We take the propagation constant to be

$$\gamma = \alpha + i\beta, \quad (3.8)$$

where α is the attenuation constant in nepers/m, and

$$\beta = \frac{\omega\sqrt{\epsilon}}{c}, \quad (3.9)$$

where ϵ is the dielectric permittivity in the coaxial cable, and c is the speed of light. At the probe end of the resonator, the voltage and current are

$$\begin{aligned} V_3 &= e^{i\omega t} (V'_+ e^{-\gamma L} + V'_- e^{\gamma L}) \\ I_3 &= \frac{e^{i\omega t}}{Z_C} (V'_+ e^{-\gamma L} - V'_- e^{\gamma L}), \end{aligned} \quad (3.10)$$

where L is the length of the resonator. Finally, at the coupling capacitor, we have

$$\begin{aligned} I_1 &= I_2 \\ V_2 - V_1 &= I_1 Z_{cap}. \end{aligned} \quad (3.11)$$

Combining the above equations, we find

$$Z_{res} = \frac{V_1}{I_1} = Z_{cap} + Z_C \left[\frac{(Z_x + Z_C) e^{\gamma L} + (Z_x - Z_C) e^{-\gamma L}}{(Z_x + Z_C) e^{\gamma L} - (Z_x - Z_C) e^{-\gamma L}} \right]. \quad (3.12)$$

Thus, the diode detector voltage V_{diode} can be calculated using equations 3.5 and 3.12.

These equations are part of a Mathematica [121] program called “Model Zx.nb.” The frequency shift can be calculated in Mathematica as well, by determining the change in frequency of a resonant minimum. The Q can also be calculated, using the method described in section 2.4.3.

We determined the quantities α and C_{cap} as follows [92]. For a resonator which is 6 ft long, we experimentally measured $Q_0 = 555$ and $Q_L = 353$. We then used α and C_{cap} as fitting parameters to obtain agreement between the experiment and the model for Q_0 and Q_L . The resulting parameters were $\alpha = -1.26$ dB/m $= -0.145$ nepers/m (in close agreement with the manufacturer’s specified value of $\alpha = -1.23$ dB/m [114]), and $C_{cap} = 0.17$ pF.

For a conducting thin film sample, we took the sample impedance Z_x to be a capacitor and resistor in series (see Fig. 2.1):

$$Z_x = \frac{1}{i\omega C_x} + R_x. \quad (3.13)$$

The capacitor C_x is taken to be a parallel plate capacitor the size of the probe center conductor:

$$C_x = \frac{\epsilon_0 \pi r_o^2}{h}, \quad (3.14)$$

where ϵ_0 is the permittivity of free space, r_o is the radius of the probe center conductor, and h is the height of the probe above the sample. The resistance R_x is simply the sheet resistance of the conducting thin film (see Appendix A) [92, 4].

3.3 Calibration Using a Variable-Thickness Aluminum Thin Film

To determine the relationship between the properties R_x and h , and the measured quantities Δf and Q_0 , a sheet resistance calibration standard was required. We used a variable-thickness aluminum thin film for this standard. The film was deposited using thermal deposition, with one end of the sample closer to the aluminum source than the other end. Because of the $1/r^2$ dependence of the flux of aluminum atoms, the film grew thicker at the end of the sample which was the closest to the aluminum source. The result was a sample with a wedge-shaped cross section [Fig. 3.2(a)]. After all microwave microscope measurements of the calibration sample were complete, we cut the aluminum film into narrow strips with a razor blade [Fig. 3.2(b)]. This allowed two-point dc resistance measurements to be made with an ohmmeter. The resistance could then be converted into sheet resistance R_x using the formula

$$R_x = \frac{\rho}{t_f} = \frac{R_{dc}w}{L}, \quad (3.15)$$

where ρ is the resistivity, t_f is the film thickness, R_{dc} is the measured dc resistance, w is the width of the metallic strip, and L is its length. This formula assumes $L \gg w$. The resulting R_x as a function of position across the sample is shown in Fig. 3.2(c).

The data from the sheet resistance calibration sample is shown in Fig. 3.3. Measurements were made with a probe with a $500 \mu\text{m}$ diameter center conductor at 7.5 GHz, with h ranging from $40 \mu\text{m}$ to $800 \mu\text{m}$. As shown in Fig. 3.3(a), the frequency shift Δf monotonically becomes more negative with decreasing sheet resistance. This is because a small sheet resistance presents a large perturbation

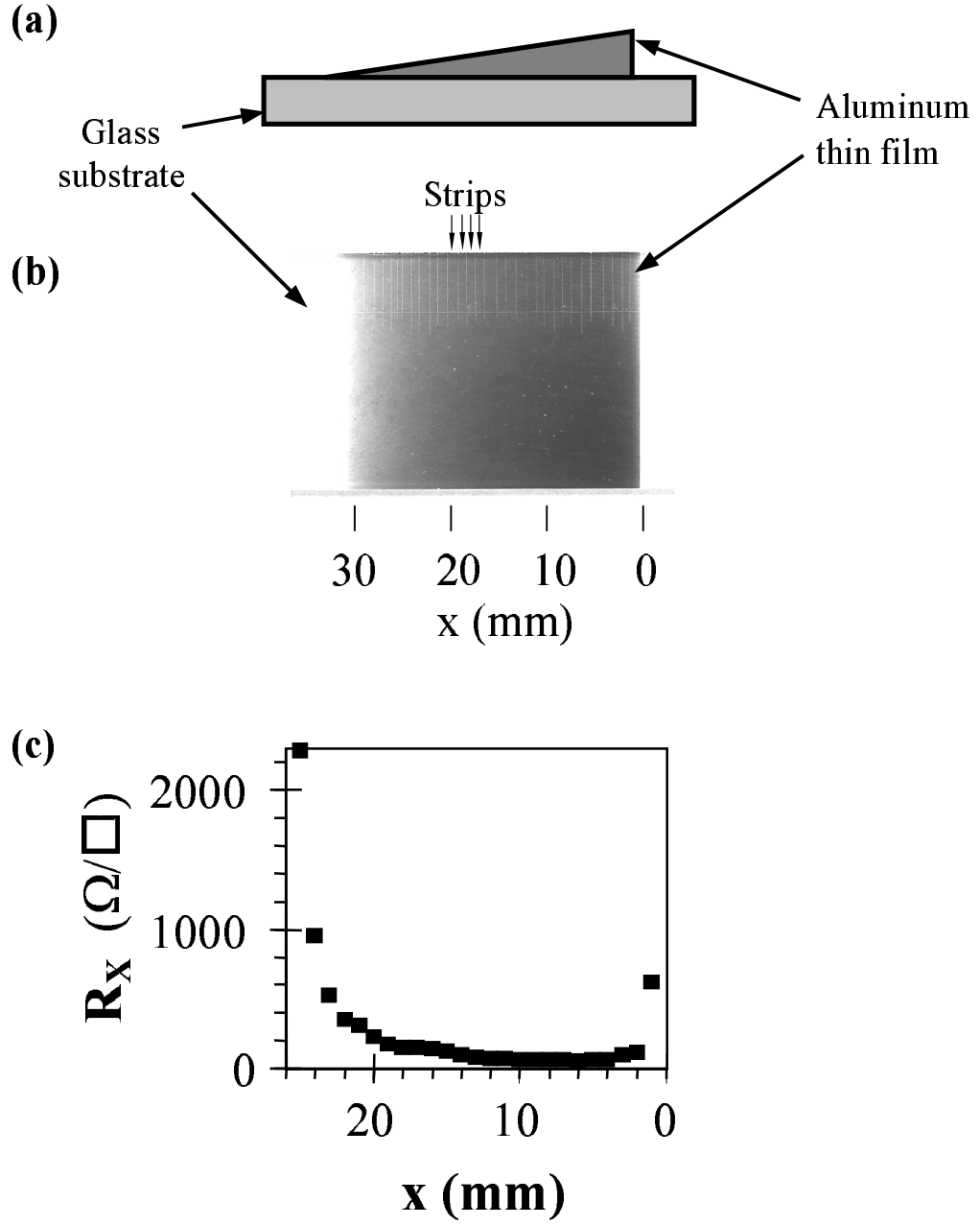


Figure 3.2: (a) Cross section and (b) top view (optical photograph) of the variable-thickness aluminum calibration sample. The cuts in the aluminum film, allowing two-point resistance measurements, are visible in (b). The dc sheet resistance across the sample as measured by a two-point probe is shown in (c).

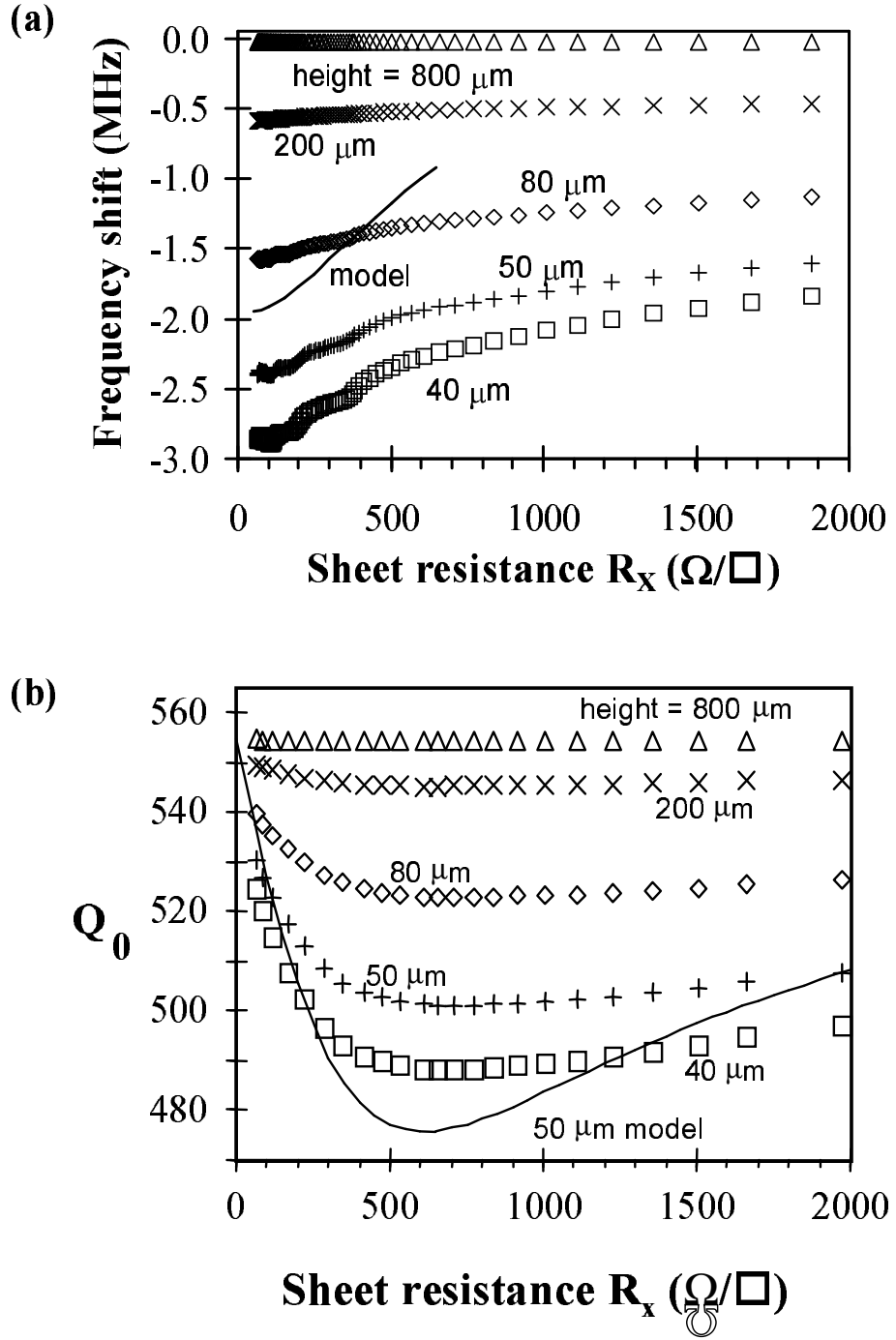


Figure 3.3: (a) Frequency shift (Δf) and (b) Q_0 vs. sheet resistance (R_x). The labels indicate different probe-sample separations. The solid lines are model results (Sec. 3.2).

to the resonator, causing the boundary condition at the probe end of the resonator to move from an open circuit, toward a short circuit.

The Q , on the other hand, is a non-monotonic function of sample sheet resistance. The value of Q_0 is a maximum at small R_x , because resistive losses are minimized here. As R_x increases, Q_0 drops due to loss from currents induced in the sample, reaching a minimum around $R_x = 660 \text{ } \Omega/\square$ for a height of $50 \text{ } \mu\text{m}$. Similarly, as $R_x \rightarrow \infty$, resistive losses are no longer present, causing Q_0 to again reach its maximum value.

The model results for a height of $50 \text{ } \mu\text{m}$ are shown as solid lines in Fig. 3.3(a) and (b). In Fig. 3.3(a), the measured frequency shift is underestimated slightly by the model. As R_x increases, the model curve quickly moves toward $\Delta f = 0$. This is due to the presence of the substrate, which itself contributes to Δf , and is ignored in the model. At small R_x , the model is the most accurate, because the metallic film effectively screens the substrate, so that the substrate has a diminished contribution to Δf .

Figure 3.3(b) shows good qualitative agreement between the model curve for $Q(R_x)$ and the data at a height of $50 \text{ } \mu\text{m}$. Although Q_0 is underestimated in the model, the value of R_x where Q_0 is a minimum is within 10 % of the measured value.

We also note that when the probe is located $50 \text{ } \mu\text{m}$ above the bare glass substrate, $Q_0 = 549$, which is only slightly less than $Q' = 555$ when the probe is far away ($>1 \text{ mm}$) from the sample. Using $1/Q_0 = 1/Q_s + 1/Q'$, we find $Q_s = 51000 \gg Q' = 555$, where Q_s is associated with losses in the glass substrate, and Q' is associated with losses in the transmission line. As a result, we conclude that the glass substrate has little effect on Q_0 . In contrast, frequency shift is

highly sensitive to the substrate [93, 112]. This suggests that we use the Q data, rather than the frequency shift data, to generate substrate-independent images of thin film sheet resistance.

As shown in Fig. 3.3, R_X is a double-valued function of Q_0 . This presents a problem for converting the measured Q_0 to R_X . However, R_X is a single-valued function of the frequency shift [93], allowing one to use the frequency shift data to determine which branch of the $R_X(Q)$ curve should be used (see Sec. 3.4 below).

3.4 Imaging the Microwave Sheet Resistance of a $\text{YBa}_2\text{Cu}_3\text{O}_{7-\delta}$ Thin Film

To explore the capabilities of our system, we scanned a thin film of $\text{YBa}_2\text{Cu}_3\text{O}_{7-\delta}$ (YBCO) on a 5 cm-diameter sapphire substrate at room temperature [92]. The film was deposited using pulsed laser deposition with the sample temperature controlled by radiant heating. The sample was rotated about its center during deposition, with the ~ 3 cm diameter plume held at a position halfway between the center and the edge. The thickness of the YBCO thin film varied from about 100 nm at the edge to 200 nm near the center.

Figure 3.4 shows three microwave images of the YBCO sample. The frequency shift [Fig. 3.4(a)] and Q_0 [Fig. 3.4(b)] were acquired simultaneously, using a probe with a 500 μm -diameter center conductor at a height of 50 μm above the sample. The scan took approximately 10 minutes to complete, with the scanning stage moving at 25 mm/s and raster lines 0.5 mm apart. The frequency shifts in Fig. 3.4(a) are relative to the resonant frequency of 7.5 GHz when the probe was far away (>1 mm) from the sample; the resonant frequency shifted downward

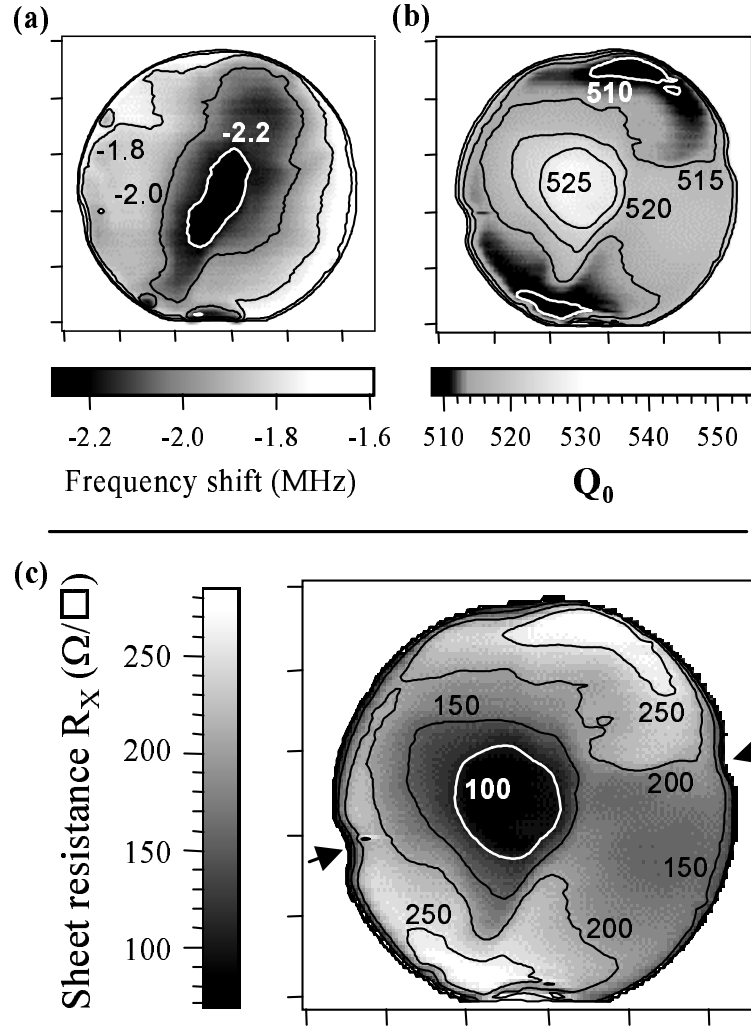


Figure 3.4: Images of a variable-thickness YBCO thin-film on a 5 cm-diameter sapphire wafer, where the film is the thickest at the center. The tick marks are 1 cm apart for the images of (a) frequency shift relative to the resonant frequency when the probe is far away (>1 mm) from the sample, (b) unloaded Q , and (c) sheet resistance (R_x). The arrows in (c) point to small semi-circular regions where clips held the wafer during deposition, and thus no film is present. The labels indicate values at each contour line. A probe with a $500\ \mu\text{m}$ diameter center conductor was used at a height of $50\ \mu\text{m}$, at a frequency of 7.5 GHz.

by more than 2.2 MHz when the probe was above the center of the sample. Noting that the resonant frequency drops monotonically between the edge and the center of the film, and that the resonant frequency is a monotonically increasing function of sheet resistance [93], we conclude that the sheet resistance decreases monotonically between the edge and the center.

The frequency shift and Q_0 images [Fig. 3.4(a) and (b)] differ slightly in the shape of the contour lines. This is most likely due to the 300 μm -thick substrate being warped, causing a variation of a few microns in the probe-sample separation during the scan [6]. However, for a sample such as that shown in Fig. 3.4, with an R_X variation across the sample of $\sim 100 \text{ } \Omega/\square$, the Q_0 data are primarily sensitive to changes in R_X , while the frequency shift data are primarily sensitive to changes in probe-sample separation. As a result, we attribute the difference between the frequency shift and Q_0 images to small changes in probe-sample separation, which will mainly affect the frequency shift data. Since the values of R_X are retrieved from the Q data, the warping does not affect the final R_X appreciably.

From Fig. 3.4(b), we see that the lowest Q occurs near the edge of the film, and that the Q rises toward the center of the sample. As mentioned above, R_X is not a single-valued function of Q and we must use the frequency shift image [Fig. 3.4(a)] to determine which branch of the Q_0 vs. R_X curve in Fig. 3.3(b) to use. From the frequency shift image we learned that R_X decreases monotonically from the edge to the center of the sample; therefore we use the branch of the Q_0 vs. R_X curve with $R_X < 660 \text{ } \Omega/\square$, since this is the branch that yields a decreasing R_X for increasing Q_0 .

With the appropriate branch identified, we transformed the Q image in Fig.

3.4(b) to the sheet resistance image in Fig. 3.4(c) using a polynomial least-squares fit to the data presented in Fig. 3.3 for $R_X < 540 \text{ } \Omega/\square$ and a height of $50 \text{ } \mu\text{m}$. Figure 3.4(c) confirms that the film does indeed have a lower resistance near the center, as was intended when the film was deposited. We note that the sheet resistance does not have a simple radial dependence, which could be due to either non-stoichiometry or defects in the film.

After scanning the YBCO film, we photolithographically patterned it into a grid of “H”-shaped regions for four-point dc resistance measurements all over the wafer [see Fig. 3.5(a)]. We calculated the sheet resistance at each “H” using Eq. 3.15. The dc sheet resistance [Fig. 3.5(c)] has a spatial dependence identical to the microwave data in Fig. 3.4(b). However, the absolute values are approximately twice as large as the microwave results, most likely due to degradation of the film during patterning.

3.5 Sheet Resistance Sensitivity

To estimate the sheet resistance sensitivity, we monitored the noise in $V_{2f_{FM}}$. We found the Q sensitivity of the system to be $\Delta Q_0 \approx 0.08$ for $Q_0 = 555$ and an averaging time of 10 ms. Combining this with the data in Fig. 3.3, we found $\Delta R_X/R_X = 6.4 \times 10^{-3}$, for $R_X = 100 \text{ } \Omega/\square$ using a probe with a $500 \text{ } \mu\text{m}$ diameter center conductor at a height of $50 \text{ } \mu\text{m}$ and a frequency of 7.5 GHz. The sensitivity scales with the capacitance between the probe center conductor and the sample (C_X) [Eq. 3.14]; increasing the diameter of the probe center conductor and/or decreasing the probe-sample separation h would improve the sensitivity. On the down side, decreasing h also increases the sensitivity to fluctuations in h due to

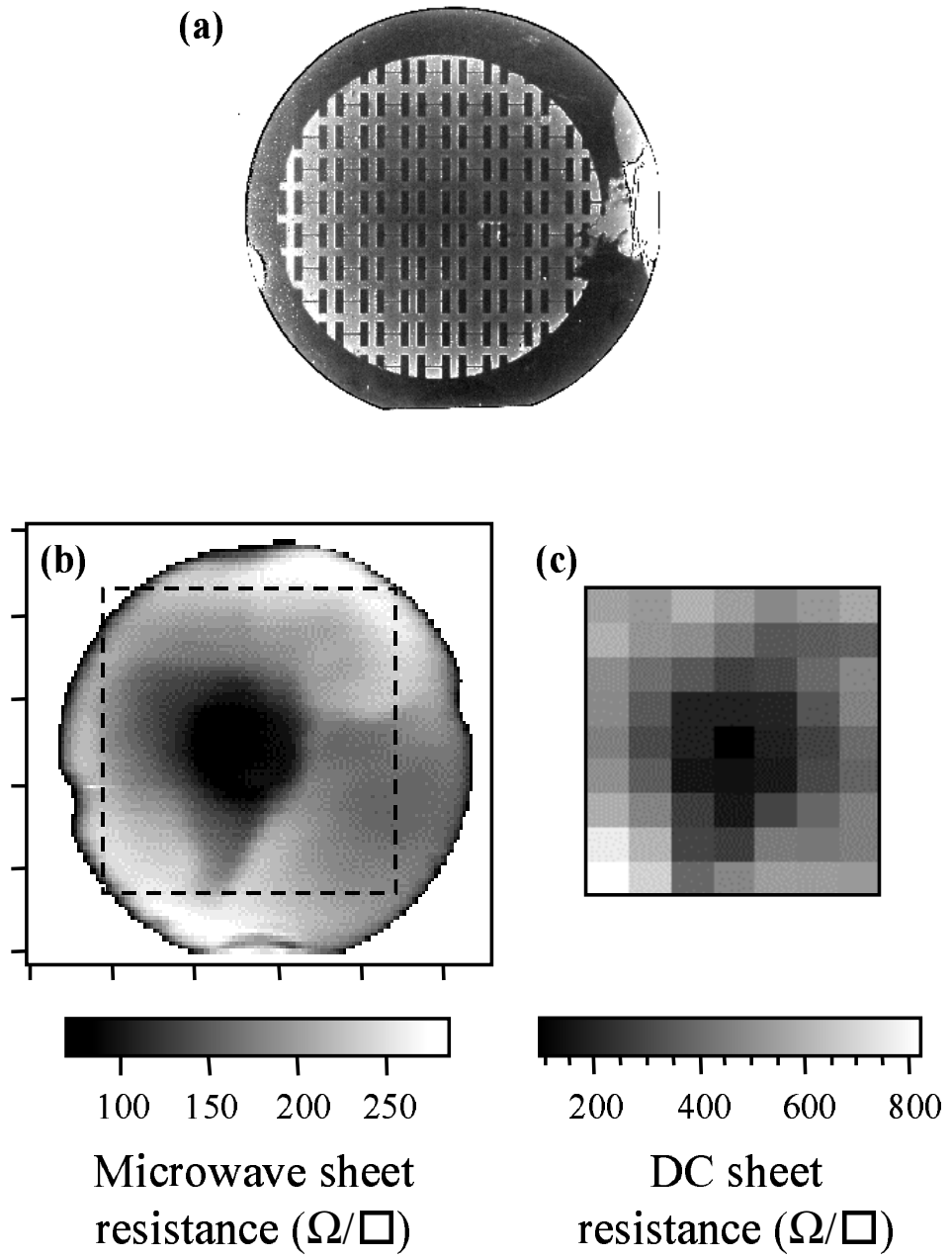


Figure 3.5: (a) Optical photograph, (b) microwave microscope image, and (c) dc resistance image of the YBCO wafer. The “H” shaped regions in (a) were patterned after image (b) was acquired, and were used to measure the dc sheet resistance values shown in (c).

vibration in the scanning apparatus and nonlinearity in the scanning stages (see Sec. 2.2).

Chapter 4

High-Resolution Dielectric Imaging

4.1 Introduction

For the next step in quantitative imaging with the microwave microscope, I chose dielectric crystals and thin films. Dielectric imaging was performed in contact mode (see Sec. 2.2), as opposed to sheet resistance imaging (Chapter 3), which was performed in non-contact mode.

There were several reasons for choosing contact mode. First, I wanted to push the limits of the spatial resolution of the microscope. Since the spatial resolution is approximately equal to the larger of the probe center conductor diameter and the probe-sample separation, achieving $1\text{ }\mu\text{m}$ spatial resolution requires having the probe tip within $1\text{ }\mu\text{m}$ of the sample; the easiest way to do this was simply putting the probe in contact. This higher spatial resolution was beneficial, in that it allowed imaging of defects in thin films and domains in crystals, rather than averaging over large areas of the samples. The second reason for using contact mode is its enhanced sensitivity to thin films. Because the depth resolution of the microscope is approximately equal to its lateral spatial resolution, imaging with a $500\text{ }\mu\text{m}$ diameter probe tip out of contact would be sensitive to not only

the thin film, but the substrate as well. Because the substrate is much thicker than the film, substrate properties would dominate the measurement. With a $1\text{ }\mu\text{m}$ diameter probe tip in contact, however, the microscope is sensitive to the properties of the sample within $\sim 1\text{ }\mu\text{m}$ of the probe tip, making this method quite sensitive to thin film properties. The final advantage of contact mode is the ability to apply a voltage bias directly to the sample, permitting nonlinear dielectric imaging (see Chapter 6).

4.2 Changes to the Microscope Apparatus

As described in Sec. 2.2, contact mode uses a sharp STM tip which extends from the probe center conductor. The sample is held in gentle contact with this tip using a spring-loaded cantilever (Fig. 2.5).

In addition, a bias tee was inserted into the resonator, allowing the probe tip to be given a dc or low-frequency voltage bias. The resulting electric field in the sample is useful for measuring dielectric non-linearity (Chapter 6), as well as for imaging ferroelectric domains (Chapter 7).

To increase the microscope's sensitivity to sample permittivity, I decreased the resonator's length from $\sim 2\text{ m}$ to $\sim 30\text{ cm}$. This increased the spacing between resonant frequencies, effectively increasing the frequency shifts that occur due to the sample perturbation. A tradeoff is that the Q of the resonator went down, which can be understood using the equation

$$Q_L = \frac{\omega_0 W}{P_l^{cable} + P_l^{ends}}, \quad (4.1)$$

where ω_0 is the resonant frequency, W is the energy stored in the resonator, and P_l^{cable} is the rate of energy loss in the coaxial cable. The quantity P_l^{ends}

is the rate of energy loss at the ends of the resonator, and includes loss in the coupling capacitor and probe, and radiation from the probe. If the length of a resonator is reduced by a factor of 2, W and P_l^{cable} also decrease by about a factor of 2. However, P_l^{ends} remains virtually constant. Thus, when the resonator is shortened, the Q will drop by an amount dependent on loss at the ends of the resonator.

A final change to the microscope was to construct a Plexiglass enclosure around the apparatus, to solve a problem with shifts in the position of the probe relative to the sample due to thermal drifts. This not only reduced air currents, but also stabilized the temperature of the apparatus. The result was that thermal drifts were significantly reduced, so that scans became much more repeatable. Previously, the relative placement of the probe and sample could drift by 10 μm or more in an hour; with the enclosure, this drift was reduced to 2 μm or less. This drift could probably be reduced further by isolating the stepper motors, which get very hot, from the rest of the apparatus; in addition, the temperature inside the enclosure could be regulated electronically.

4.3 Physical Description of the Measurement

Due to the “lightning rod effect,” the microwave electric field is concentrated at the sharp STM probe tip. If these strong fields are perturbed by a sample, the boundary condition of the resonator will change. This perturbation concept is the essence of contact-mode dielectric imaging, and is the basis for the quantitative theory described in the next chapter.

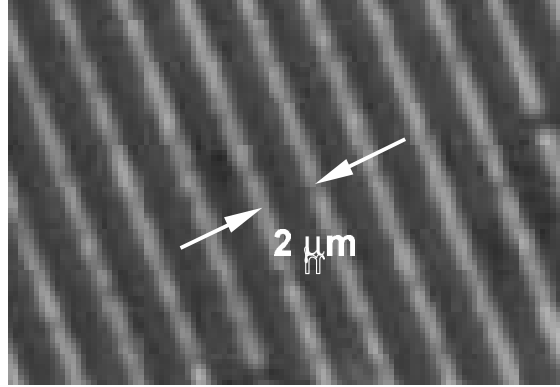
4.4 Spatial Resolution

The concentration of the electric field near the probe tip is expected to have a length scale approximately equal to the radius of curvature of the STM tip. Thus, if the tip has a radius of $1\text{ }\mu\text{m}$, the lateral as well as depth resolution should be approximately equal to $1\text{ }\mu\text{m}$.

A demonstration of the spatial resolution is shown in Fig. 4.1. A sample containing aluminum lines with a spacing of $2\text{ }\mu\text{m}$ on a stretched 1.5 mm thick stretched Mylar film [56], was scanned along a straight path perpendicular to the lines. The minima in the frequency shift in Fig. 4.1 indicate the locations of the aluminum lines. The minima have different magnitudes, probably due to the probe scratching the lines during scanning. This figure shows that the spatial resolution of the microscope is better than $2\text{ }\mu\text{m}$.

A second demonstration of the spatial resolution of the microscope is shown in Fig. 4.2. The sample, from a leading semiconductor manufacturer, contains $2\text{ }\mu\text{m}$ wide aluminum lines which are buried beneath a $1\text{ }\mu\text{m}$ thick SiO_2 dielectric overlayer. An optical photograph is shown in Fig. 4.2(a), while frequency shift and Q images are shown in (b) and (c). The image in (b) shows that even with the metallic lines $1\text{ }\mu\text{m}$ below the probe tip, the spatial resolution is $\sim 2\text{ }\mu\text{m}$. We expect the resolution to be worse in the case of buried features than in the measurement of surface properties, since the buried metallic lines are farther from the probe tip, where the microwave electric field is weaker and more spread out.

(a)



(b)

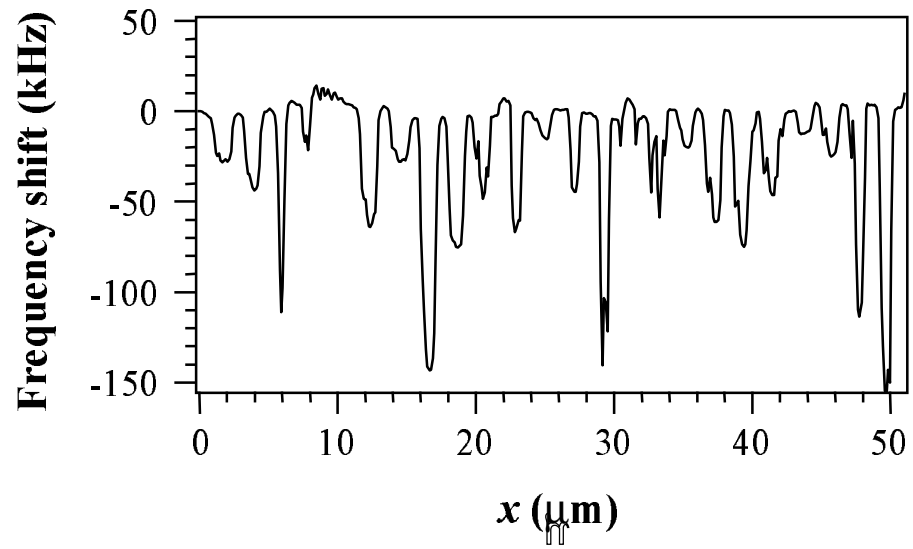


Figure 4.1: (a) Optical photograph, and (b) a line scan, of a series of aluminum lines on Mylar. The lines are $\sim 0.6 \mu\text{m}$ wide, and have a periodicity of $2 \mu\text{m}$.

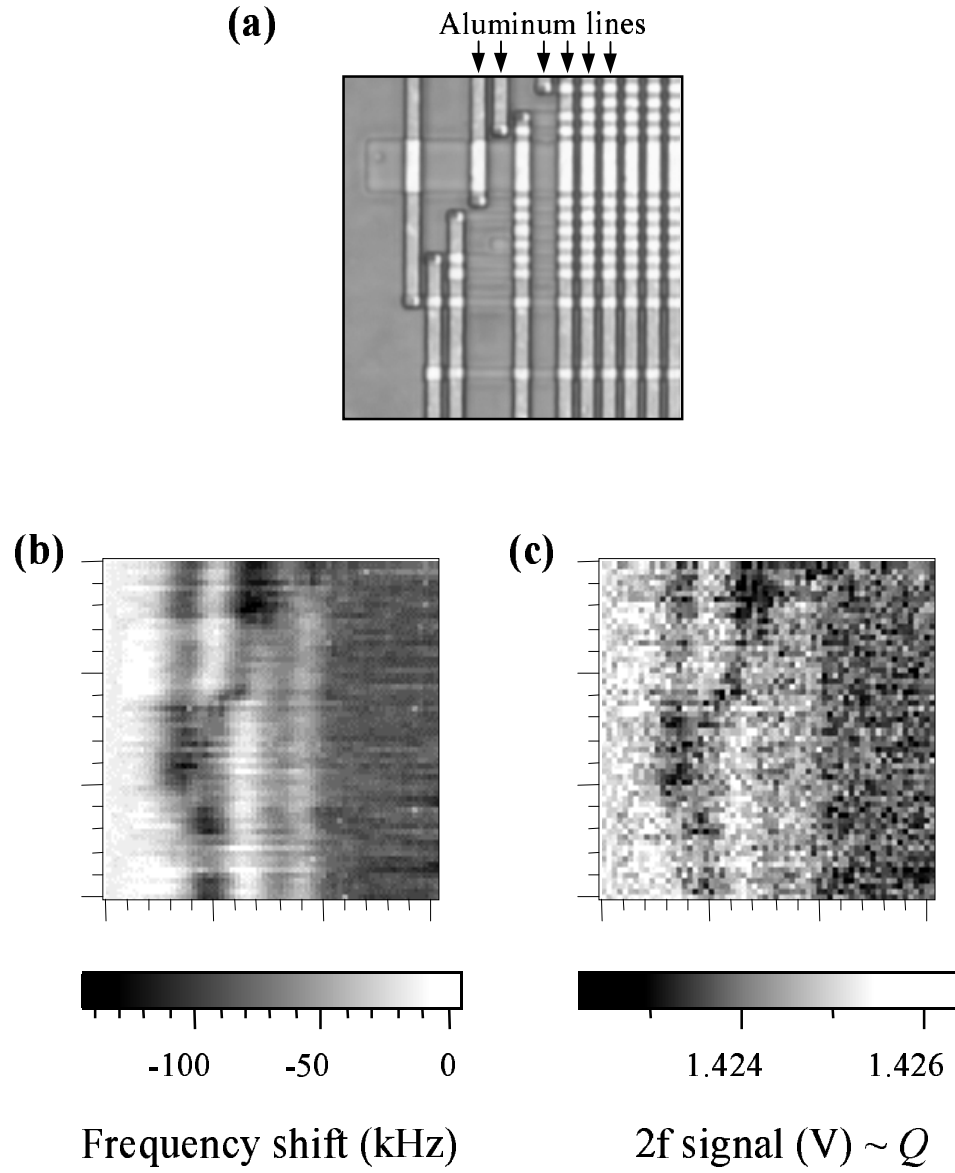


Figure 4.2: A sample with 2 μm -wide aluminum lines, which are buried under a 1 μm thick SiO dielectric overlayer. (a) Optical photograph, (b) frequency shift (Δf) image, and (c) “2f” signal image are of the same $30 \times 30 \mu\text{m}^2$ region.

4.5 Effect of Contact on the Probe Tip and Sample

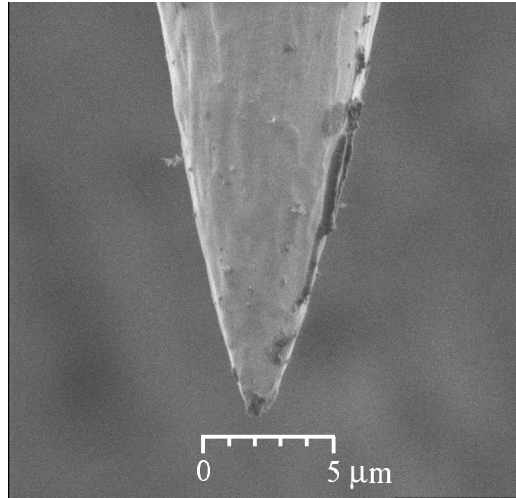
4.5.1 Damage to the Probe Tip

A concern with contact mode imaging is that both the probe and sample could become damaged due to the probe tip being pressed against and dragged across the sample. For a probe tip with a radius of $0.5\ \mu\text{m}$ pressed against a sample with a force of $50\ \mu\text{N}$, the pressure is $6 \times 10^7\ \text{Pa}$, which could be enough to damage the sharp tip.

To preserve the sharpness of the probe tip, two things can be done. First, the force between the probe and the sample is minimized, using the spring-loaded cantilever described in Sec. 2.2. Second, we use STM tips made of tungsten, which is a hard metal.

Figure 4.3(a) shows a scanning ion-beam image, taken by Andrei Stanishvsky, of one of our STM tips before being used for scanning. The radius of curvature of the tip is approximately $0.5\ \mu\text{m}$. Figure 4.3(b) shows a tip after it has been used for several scans in contact mode. The sharp end has now become blunt, with a radius of about $1.5\ \mu\text{m}$. The tip is asymmetric, due to the probe being dragged across the sample from right to left. Despite the bluntness of a used STM tip, we find experimentally that the spatial resolution is still $1\text{--}2\ \mu\text{m}$, which is somewhat surprising considering the bluntness of the used tip shown in the Fig. 4.3(b).

(a)



(b)

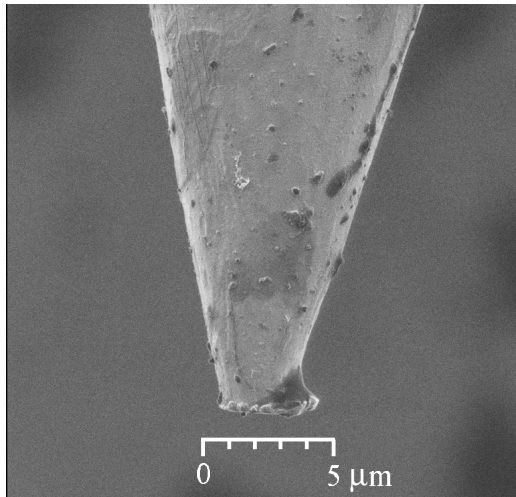


Figure 4.3: Scanning ion-beam images of (a) an unused STM tip, and (b) a tip which has been used in contact mode with the microwave microscope.

4.5.2 Damage to the Sample

The second concern with contact mode imaging is damage to the sample. We would expect the dragging motion of a probe to scratch the sample.

Figure 4.4(a) shows a frequency shift (Δf) image of a $\text{Ba}_{0.6}\text{Sr}_{0.4}\text{TiO}_3$ thin film (this sample will be discussed further in Chapters 5 and 6). The image is of a $20 \times 20 \mu\text{m}^2$ region, and has a vertical line (marked by the arrows) which has been milled through the thin film with a focused ion beam.

Figure 4.4(b) shows an atomic force microscope (AFM) image of the same region as (a), acquired after the microwave imaging. No sign of scratching by the microscope probe tip is evident in the image. Thus, we can conclude that at least as long as a sample isn't too soft, the surface will not be significantly damaged by contact mode imaging.

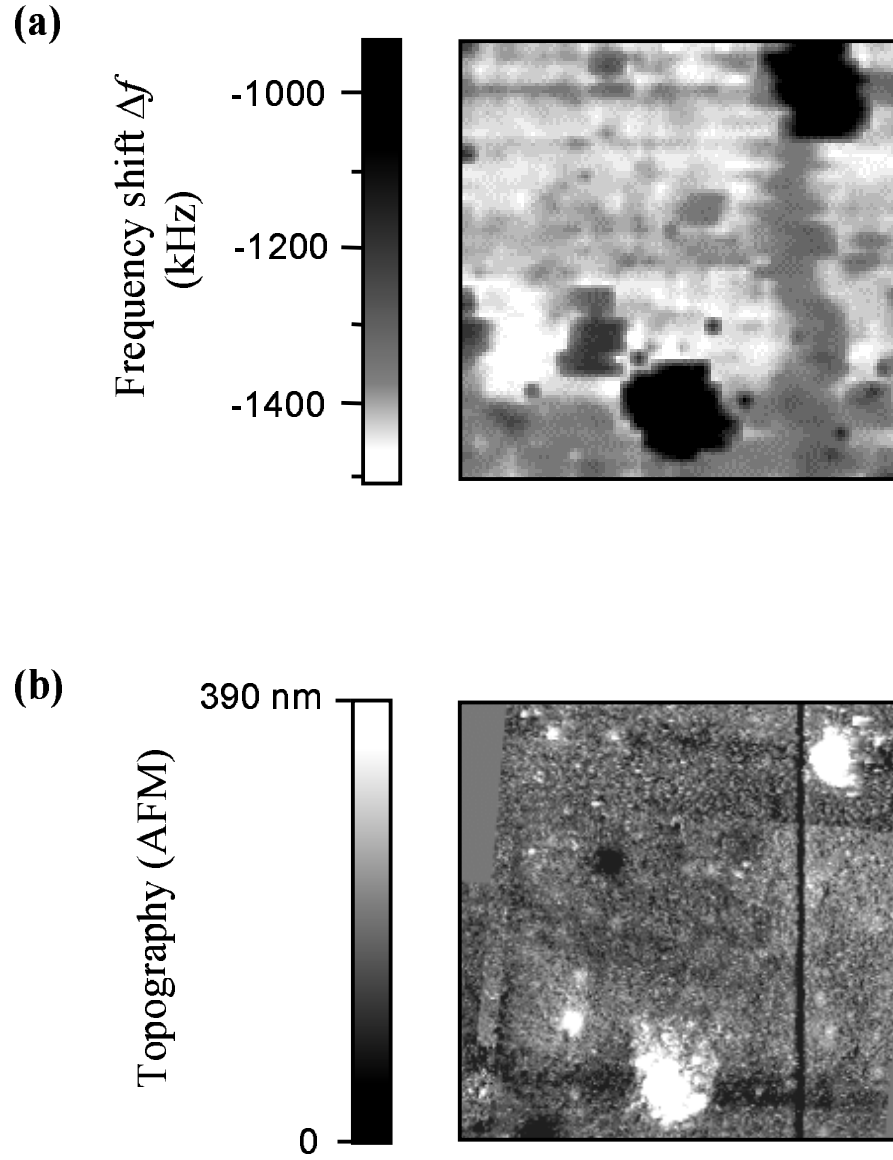


Figure 4.4: (a) A frequency shift (Δf) image of a $\text{Ba}_{0.6}\text{Sr}_{0.4}\text{TiO}_3$ thin film sample. The scan region is $20 \times 20 \mu\text{m}^2$. (b) An AFM image of the same region, which shows no evidence of scratching by the microwave microscope probe tip.

Chapter 5

A Physical Model for Dielectric Imaging

5.1 Introduction

To go beyond imaging surface property contrast in dielectrics, quantitative dielectric imaging is required. We accomplished this using a physical model for the system. Using this physical model, we can obtain the relationship between the frequency shift Δf of the microscope and the permittivity ϵ_r of the sample. This requires calibration standards which have known permittivities. However, because of the model, the calibration standards don't have to be exactly like the sample of interest. For example, for a dielectric thin film sample, one doesn't need to have a thin film calibration standard, which would be difficult, considering the large variation in permittivity from sample to sample for thin films. Finally, the model allows the use of different probe tips which aren't exactly alike; this is especially important for STM tips in contact with the sample, where the shape of the sharp tip, which can vary, affects the measurement.

Thus, the model has three purposes: (1) to interpolate between data from calibration samples (Sec. 5.4), (2) to allow the quantitative imaging of samples which aren't exactly like the calibration samples (Sec. 5.5), and (3) to allow for

probe tips which have different shapes (Sec. 5.2.1).

5.2 Modeling the Fields Near the Probe Tip

5.2.1 Model Geometry

The first step for modeling quantitative dielectric imaging is to calculate the microwave fields near the probe tip. The simplest case is a uniform bulk dielectric sample. Because the probe tip length is much less than the wavelength $\lambda \sim 4$ cm, a static calculation [81] of the microwave electric fields is sufficient. Due to the complicated geometry of the probe tip in contact with a multi-layered sample, I used a finite element model, rather than an analytical model (see Sec. 5.6.3). Cylindrical symmetry further simplified the problem to two dimensions.

The resulting problem (Fig. 5.1) consists of a rectangular grid, with the two axes r (the cylindrical radius) and z . The left border of the grid is the cylindrical axis, with $r = 0$. The bottom border of the grid is the sample holder. The sharp probe tip was defined to be at a potential $\Phi = 1$. Beneath the sample, I used the boundary condition $\Phi = 0$, which is the boundary condition for a metal. Thus, experimentally, the sample holder has a metal layer on top of which the sample is placed; an advantage of this metal layer is that the microwaves are screened from whatever is beneath the metal. The outer boundary of the finite element grid must be sufficiently far away from the probe tip that the chosen boundary conditions do not affect the calculated electric field near the probe tip. A finite element grid outer radius of at least 4 mm, and a height of the top boundary above the sample surface of 1.5 mm, were adequate. The outer boundary condition was $d\Phi/dn = 0$ where n is the coordinate normal to the edge. It would have been

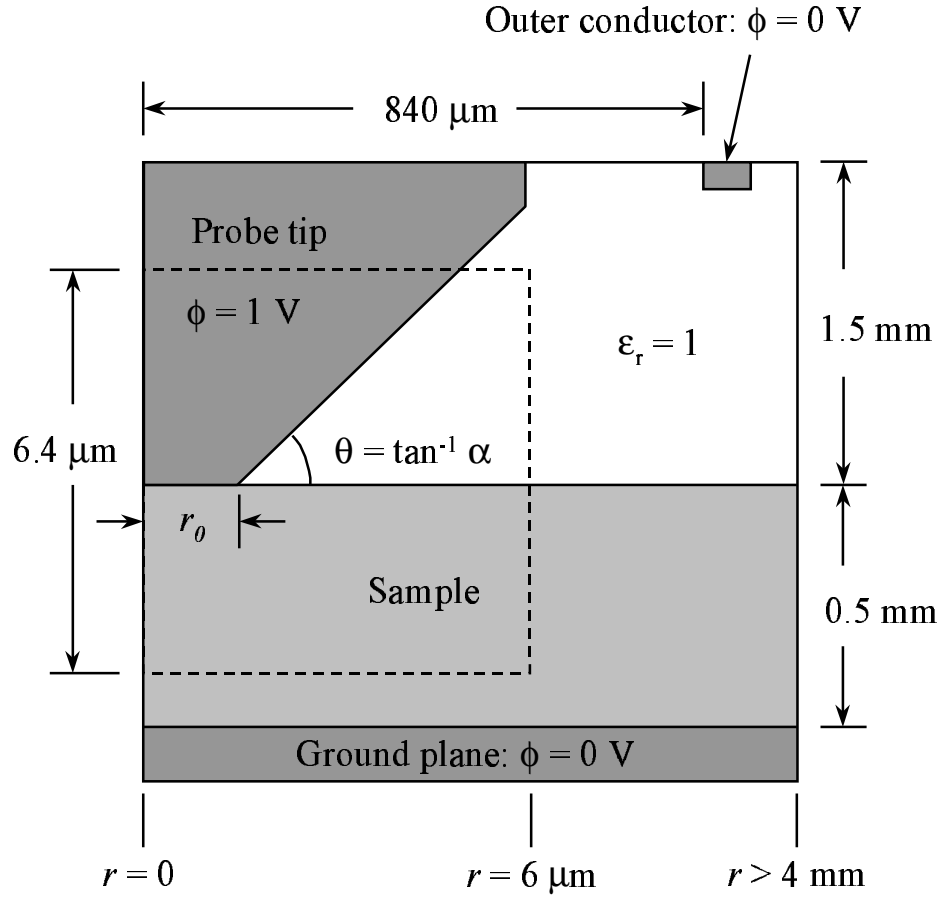


Figure 5.1: The geometry of the finite element relaxation model (not to scale). The left border represents the cylindrical coordinate axis. Inside the dashed box, the grid cell spacings, Δr and Δz are constant, while outside, they continuously increase toward the boundaries.

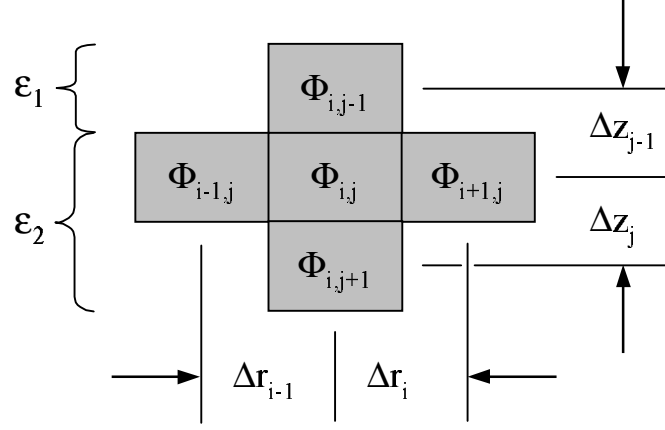


Figure 5.2: A grid element in the finite element simulation, and the four adjacent element. The permittivity ϵ_r changes between row $j - 1$ and row j .

equally appropriate to use the outer boundary condition $\Phi = 0$, since the electric field is small far away from the probe tip.

The probe tip is represented as a cone of aspect ratio α with a blunt end of radius r_0 . For each column of grid elements, Δr is defined as the physical distance represented by the spacing between columns in the grid (see Fig. 5.2). Similarly, for each row of cells, Δz represents the spacing between rows in the vertical direction. Inside the dashed box in Fig. 5.1, both Δr and Δz are constant. However, outside the dashed box, both Δr and Δz continually increase toward the boundary of the grid. This allows the grid element spacing to be small ($\leq 0.1 \mu\text{m}$) inside the dashed box where the electric field is strongest, and large near the boundary where the electric field is weakest, permitting the outer boundaries to be very far away from the probe tip.

To account for variation between probe tips, the probe aspect ratio $\alpha =$

$\Delta z/\Delta r$ can be adjusted by changing Δz or Δr inside the dashed box in Fig. 5.1. For example, for $\Delta z = \Delta r$, the angle θ in Fig. 5.1 is 45° . For the results here, I fixed $\Delta z = 0.1 \mu\text{m}$ inside the dashed box, and varied Δr inside the box to change α .

5.2.2 The Finite Element Model Equations

From elementary electrostatics [52], we have the three following equations, where \mathbf{E} is the electric field, \mathbf{D} is the electric displacement, ϵ_0 is the permittivity of free space, ϵ_r is the relative permittivity, and Φ is the potential:

$$\nabla \cdot \mathbf{D} = 0 \quad (5.1)$$

$$\mathbf{D} = \epsilon_0 \epsilon_r \mathbf{E} \quad (5.2)$$

$$\mathbf{E} = -\nabla \Phi. \quad (5.3)$$

Combining these, we find

$$\nabla^2 \Phi + \frac{1}{\epsilon_r} (\nabla \Phi) \cdot (\nabla \epsilon_r) = 0. \quad (5.4)$$

The second term is due to changes in the permittivity ϵ_r ; without this term, we would have the Laplace equation.

As shown in Fig. (5.2), $\Phi_{i,j}$ is the potential at the grid element at column i and row j ; r is the radial coordinate, while z is the vertical coordinate. Also, Δz_{j-1} , Δz_j , Δr_{i-1} , and Δr_i are the physical separation between grid elements represented in the model; in general, they do not have to be equal. Finally, ϵ_1 and ϵ_2 are the permittivities of row $j-1$, and rows j and $j+1$, respectively. We will start with the simplest case, with $\Delta z_{j-1} = \Delta z_j = \Delta r_{i-1} = \Delta r_i \equiv \Delta r$, and $\epsilon_1 = \epsilon_2$. We need the following definitions to calculate $\Phi_{i,j}$ as a function of $\Phi_{i,j-1}$,

$\Phi_{i-1,j}$, $\Phi_{i+1,j}$, and $\Phi_{i,j+1}$:

$$\nabla^2 \Phi \implies \frac{\partial^2 \Phi}{\partial z^2} + \frac{\partial^2 \Phi}{\partial r^2} + \frac{1}{r} \frac{\partial \Phi}{\partial r} \quad (5.5)$$

$$\frac{\partial^2 \Phi}{\partial z^2} \implies \frac{\Phi_{i,j-1} - 2\Phi_{i,j} + \Phi_{i,j+1}}{(\Delta r)^2} \quad (5.6)$$

$$\frac{\partial^2 \Phi}{\partial r^2} + \frac{1}{r} \frac{\partial \Phi}{\partial r} = \frac{\Phi_{i+1,j} - 2\Phi_{i,j} + \Phi_{i-1,j}}{(\Delta r)^2} + \frac{\Phi_{i+1,j} - \Phi_{i,j}}{r \Delta r} \quad (5.7)$$

Solving Eq. 5.4 for $\Phi_{i,j}$, we find that $\Phi_{i,j}$ is a weighted average of the values of the four adjacent cells:

$$\Phi_{i,j} = \frac{\Phi_{i+1,j}(1 + \frac{\Delta r}{r}) + \Phi_{i-1,j} + \Phi_{i,j-1} + \Phi_{i,j+1}}{4 + \frac{\Delta r}{r}}. \quad (5.8)$$

A more general case for this calculation allows Δr and Δz to be unequal, and a function of the row number j and the column number i . Also, the permittivity ϵ_r can be different for different rows, as shown in Fig. 5.2. Finally, we will allow ϵ_{r2} to be anisotropic. In other words, ϵ_{r2} is a tensor, which we assume to take the form

$$\vec{\epsilon}_{\mathbf{r2}} = \begin{pmatrix} \epsilon_{r2}^r & 0 & 0 \\ 0 & \epsilon_{r2}^r & 0 \\ 0 & 0 & \epsilon_{r2}^z \end{pmatrix}. \quad (5.9)$$

Now we have the following:

$$\frac{\partial^2 \Phi}{\partial z^2} \implies \frac{2}{\Delta z_{j-1} + \Delta z_j} \left(\frac{\Phi_{i,j-1} - \Phi_{i,j}}{\Delta z_{j-1}} + \frac{\Phi_{i,j+1} - \Phi_{i,j}}{\Delta z_j} \right) \quad (5.10)$$

$$\begin{aligned} \frac{\partial^2 \Phi}{\partial r^2} + \frac{1}{r} \frac{\partial \Phi}{\partial r} \implies & \frac{2}{\Delta r_{i-1} + \Delta r_i} \left(\frac{\Phi_{i+1,j} - \Phi_{i,j}}{\Delta z_{j-1}} + \frac{\Phi_{i-1,j} - \Phi_{i,j}}{\Delta z_j} \right) \\ & + \frac{\Phi_{i+1,j} - \Phi_{i,j}}{r \Delta r_i} \end{aligned} \quad (5.11)$$

$$\frac{1}{\epsilon_r}(\nabla\Phi) \cdot (\nabla\epsilon_r) \implies \frac{1}{\epsilon_{r2}} \left(\frac{\Phi_{i,j-1} - \Phi_{i,j}}{\Delta z_{j-1}} \right) \left(\frac{\epsilon_{r1} - \epsilon_{r2}}{\Delta z_{j-1}} \right). \quad (5.12)$$

Solving Eq. 5.4, we have a new equation for $\Phi_{i,j}$ which replaces Eq. 5.8:

$$\begin{aligned} \Phi_{i,j} = & \left[2\epsilon_{r2}^z \left(\frac{\Phi_{i,j+1}\Delta z_{j-1} + \Phi_{i,j-1}\Delta z_j}{\Delta z_{j-1} + \Delta z_j} \right) \right. \\ & + 2\epsilon_{r2}^r \left(\frac{\Delta z_{j-1}\Delta z_j}{\Delta r_{i-1}\Delta r_i} \right) \left(\frac{\Phi_{i+1,j}\Delta r_{i-1} + \Phi_{i-1,j}\Delta r_i}{\Delta r_{i-1} + \Delta r_i} \right) \\ & \left. + \epsilon_{r2}^r \Phi_{i+1,j} \frac{\Delta z_{j-1}\Delta z_j}{r\Delta r_i} + \Phi_{i,j-1}(\epsilon_{r1}^z - \epsilon_{r2}^z) \frac{\Delta z_j}{\Delta z_{j-1}} \right] \\ & / \left[2\epsilon_{r2}^r \Delta z_{j-1}\Delta z_j + 2\epsilon_{r2}^z \Delta r_{i-1}\Delta r_i + \epsilon_{r2}^r \frac{\Delta z_{j-1}\Delta z_j}{r\Delta r_i} + (\epsilon_{r1}^z - \epsilon_{r2}^z) \frac{\Delta z_j}{\Delta z_{j-1}} \right] \end{aligned} \quad (5.13)$$

Equation 5.13 is the most general case that was needed for the probe tip field model.

The finite element grid consists of 84×117 cells, which is small enough to be a manageable calculation with a modern personal computer. Using Eq. 5.13 for each individual grid element, we can solve the two-dimensional finite element problem using relaxation methods [80]. The idea of a relaxation calculation is that no matter what the initial values of $\Phi_{i,j}$, by iterating the calculation for $\Phi_{i,j}$ over the whole grid, the values of Φ will gradually “relax,” or converge asymptotically, to the solution. I used a Microsoft Excel spreadsheet to perform this iterative calculation; using a spreadsheet simplified the analysis and display of the results, since all calculations could be performed in Excel. In addition, the speed of the calculation was significantly enhanced by using the method of successive over-relaxation (SOR), which is discussed in Ref. [80].

Two possible fitting parameters for the model are the aspect ratio α of the conical tip, and the radius r_0 of the blunt probe end. We obtain a satisfactory fit with our data (see below) by fixing $r_0 = (0.6 \mu\text{m})/\alpha$. This leaves α as a single

fitting parameter to represent all probe tips; typically we find that $1 < \alpha < 2$ for all of our probes. The need for only one fitting parameter is a significant result which greatly simplifies the calibration process, though it is probably a characteristic of the STM tips we use [66] rather than of STM tips in general.

Shown in Fig. 5.3(a) is the calculated electric field near the probe tip for a probe with $\alpha = 1$, and a sample with $\epsilon_r = 2.1$. We notice that the fields are concentrated near the probe tip, as expected. The spatial resolution is related to the size of the probe tip, as shown by this concentration of the fields near the tip. Figure 5.3(b) shows the calculated electric field as a function of radius away from the center of the probe, for two samples with $\epsilon_r = 2.1$ and 305. For higher ϵ_r , the fields are more highly concentrated, and fall off more quickly away from the probe, suggesting that the spatial resolution of the microscope is higher for high ϵ_r bulk materials (see Sec. 5.6.1).

5.3 Calculating Frequency Shift From Perturbation Theory

Using resonant cavity perturbation theory [5], we calculated the frequency shift of the microscope as a function of the fields near the probe tip. For this derivation, we start out with two resonant cavities, which have the same volume, but differ in the permittivities $\epsilon_1 = \epsilon_0\epsilon_{r1}$ and $\epsilon_2 = \epsilon_0\epsilon_{r2}$, and permeabilities μ_1 and μ_2 inside the two cavities. The electric and magnetic fields inside the two cavities are \mathbf{E}_1 and \mathbf{E}_2 , and \mathbf{H}_1 and \mathbf{H}_2 . Assuming that the cavities are lossless, the change in resonant frequency upon going from cavity 1 to cavity 2 is [5]

$$\frac{f_2 - f_1}{f_2} = \frac{\Delta f}{f} = \frac{\int_{V_C} [(\mu_2 - \mu_1)\mathbf{H}_1 \cdot \mathbf{H}_2 - (\epsilon_2 - \epsilon_1)\mathbf{E}_1 \cdot \mathbf{E}_2] dV}{\int_{V_C} (\epsilon_1\mathbf{E}_1 \cdot \mathbf{E}_2 - \mu_1\mathbf{H}_1 \cdot \mathbf{H}_2) dV} \quad (5.14)$$

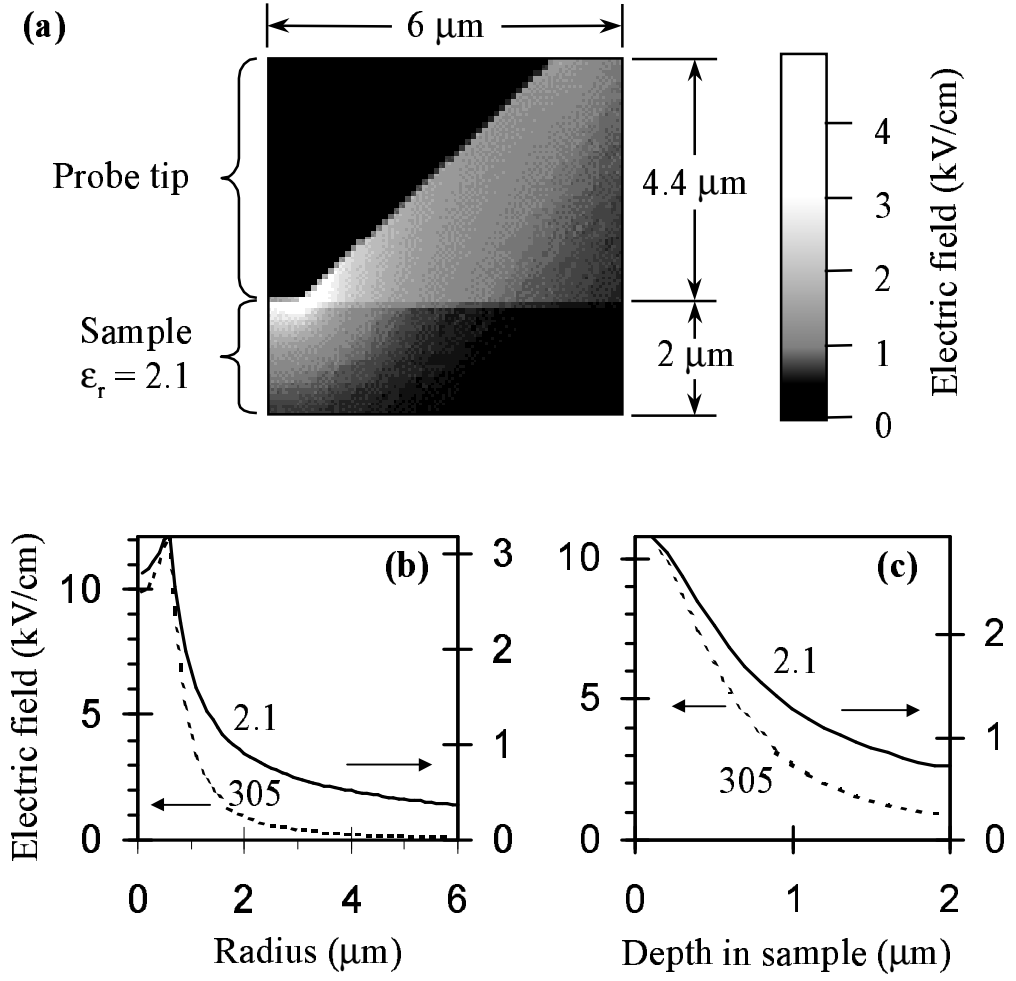


Figure 5.3: (a) The calculated electric field magnitude near the probe tip (in the region indicated by the dashed box in Fig. 5.1) for a sample with permittivity $\epsilon_r = 2.1$, and a probe with aspect ratio $\alpha = 1$ and tip bluntness $r_0 = 0.6 \mu\text{m}$. The electric field magnitude as a function of radius (b) and depth in the sample (c) are shown for samples with $\epsilon_r = 2.1$ and 305.

where V_c is the volume of the cavities, and f_1 and f_2 are the resonant frequencies of the two cavities. Since we are interested in dielectric materials rather than magnetic materials, we take $\mu_1 = \mu_2$. We also take the perturbation to be only in a small volume $V_S \ll V_C$. Thus $\epsilon_1 = \epsilon_2$ in all of the cavity except in the volume V_S of the sample, where $\epsilon_1 \neq \epsilon_2$. Using the relation

$$\int_{V_C} \epsilon |\mathbf{E}|^2 = \int_{V_C} \mu |\mathbf{H}|^2 \quad (5.15)$$

for a lossless cavity, the denominator in Eq. 5.14 becomes

$$\int_{V_C} (\epsilon_1 \mathbf{E}_1 \cdot \mathbf{E}_2 - \mu_1 \mathbf{H}_1 \cdot \mathbf{H}_2) dV = \int_{V_C} (\epsilon_1 |\mathbf{E}_1|^2 + \mu_1 |\mathbf{H}_1|^2) dV \approx 2 \int_{V_S} \epsilon_1 |\mathbf{E}_1|^2 dV \quad (5.16)$$

The energy stored in a lossless resonant cavity is

$$W = \int_V \frac{\epsilon}{4} |\mathbf{E}_1|^2 dV + \int_V \frac{\mu}{4} |\mathbf{H}_1|^2 dV = 2 \int_V \frac{\epsilon}{4} |\mathbf{E}_1|^2 dV \quad (5.17)$$

Thus, Eq. 5.14 can be written as

$$\frac{\Delta f}{f} \approx -\frac{\epsilon_0}{4W} \int_{V_S} (\epsilon_{r2} - \epsilon_{r1}) \mathbf{E}_1 \cdot \mathbf{E}_2 dV. \quad (5.18)$$

We calculate an approximate W using the equation for the loaded Q of the resonator

$$Q_L = \frac{\omega_0 W}{P_l}, \quad (5.19)$$

where ω_0 is the resonant frequency, and P_l is the power loss in the resonator.

We use Eq. 5.18 to convert the electric field calculated in Sec. 5.2.2 to the frequency shift Δf of the microwave microscope.

5.4 Bulk Sample Imaging

To establish the validity of our microscope and model for performing permittivity measurements, we started with bulk dielectric materials. For the imaging of 500

μm thick bulk samples, we use a bare $500\ \mu\text{m}$ thick LaAlO_3 (LAO) substrate for the unperturbed system ($\epsilon_{r1} = 24$, E_1) [124], because its properties are well-characterized and it is a common substrate for oxide dielectric thin films. Thus, cavity 1 (see Sec. 5.3) is the microscope with the probe in contact with a LAO sample, while cavity 2 (the perturbed system) is the microscope with the probe in contact with the sample to be imaged. The frequency shift Δf is the change in the microscope's resonant frequency upon replacement of the LAO substrate by the sample of interest with permittivity ϵ_{r2} .

In order to obtain a comparison between the model presented above and experimental results, we scanned a series of $500\ \mu\text{m}$ thick bulk dielectrics with known microwave permittivities [55, 60]: Teflon ($\epsilon_r = 2.1$), MgO ($\epsilon_r = 10$), LAO ($\epsilon_r = 24$), and SrTiO_3 ($\epsilon_r = 300$). In Fig. 5.4, the experimental frequency shift data points are shown for three different probe tips. Model fits are also shown, with different values of the fitting parameter α for each probe tip. Note that the zero of frequency shift is for LAO ($\epsilon_r = 24$), the chosen unperturbed state of our resonator.

To measure the permittivity ϵ_r of a dielectric sample, we must first calibrate the probe (i.e. determine the parameter α) using at least two samples with known ϵ_r and the same thickness. I normally use three samples (Teflon, LAO, and SrTiO_3), and plot them in a graph much like Fig. 5.4, to find the value of α which gives the best fit to the model. Once α has been determined from this calibration, we can measure ϵ_r of any sample, using the finite element model and Eq. (5.18) to convert the measured Δf to ϵ_r .

We tested this method by measuring ϵ_r of a $500\ \mu\text{m}$ thick KTaO_3 crystal, which is paraelectric with a cubic perovskite structure at room temperature ($T_c =$

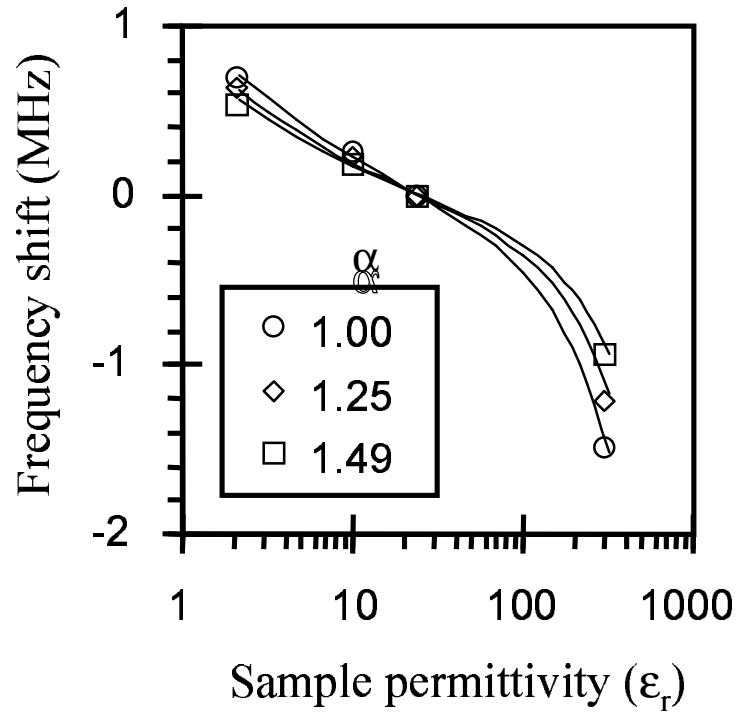


Figure 5.4: Model results (lines) vs. data (symbols) for 500 μm thick bulk dielectrics for three different probe tips with different values of the aspect ratio α . Frequency shifts are relative to a LaAlO_3 sample, with $\epsilon_r = 24$.

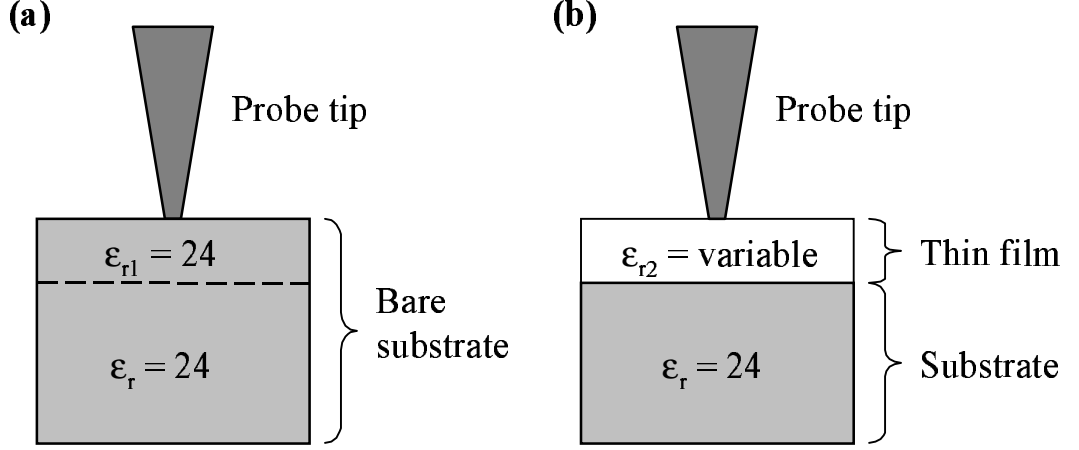


Figure 5.5: (a) The unperturbed and (b) perturbed resonator for a thin film on a LAO ($\epsilon_r = 24$) substrate.

13 K) [54]. We found the permittivity to be $\epsilon_r = 262 \pm 20$, in agreement with microwave data in the literature ($\epsilon_r = 240$ at 9.4 GHz) [84] and low-frequency data obtained with a parallel-plate capacitor ($\epsilon_r = 260$ at 100 Hz, and $\epsilon_r = 238.5$ at 100 kHz).

5.5 Thin Film Imaging

In the case of thin films on a LAO substrate, the unperturbed system (cavity 1 in Sec. 5.3) is a bare LAO substrate, while the perturbed system (cavity 2) is a thin film on a LAO substrate (see Fig. 5.5). Because the change in total thickness with the addition of a thin film is negligible compared to the $500 \mu\text{m}$ thick substrate, we can treat the thin film as the only perturbation to the system. Thus, V_S in Eq. 5.18 includes only the thin film volume, and we calculate the frequency shift Δf associated with replacing a thin top layer of the LAO substrate with a thin

Film material	Thickness (nm)	Microwave ϵ_r	ϵ_r at 10 kHz
SrTiO ₃	440	145 ± 26 at 7.2 GHz	150
Ba _{0.6} Sr _{0.4} TiO ₃	300	388 ± 14 at 8.1 GHz	700
Ba _{0.6} Sr _{0.4} TiO ₃	400	573 ± 27 at 8.1 GHz	1030

Table 5.1: Comparison of microwave permittivity ϵ_r of thin-films on LaAlO₃, measured with the microwave microscope, and low-frequency permittivity, measured using interdigital electrodes.

film of permittivity ϵ_{r2} .

Once a probe's α parameter is found using the bulk calibration method described in Sec. 5.3, we use the thin film model to obtain a functional relationship between Δf and ϵ_r of the thin film.

To test the thin film model, we imaged thin-film samples of SrTiO₃ and Ba_{0.6}Sr_{0.4}TiO₃ (BST) on 500 μm thick LAO substrates. The results are summarized in Table 5.1. The thin-film permittivity was also measured at 10 kHz using Au interdigital electrodes deposited on the films. Both our microwave measurements and the interdigital electrode measurements are primarily sensitive to the in-plane component of ϵ_r for these samples (see Sec. 5.6.2). For the SrTiO₃ sample, the microwave permittivity is comparable to the low-frequency permittivity, showing that there is very little dispersion in this film. On the other hand, the BST films both show significant dispersion, which is nonetheless within the range observed in the literature for similar films [46, 96].

5.6 Other Microscope Issues, Using the Model

5.6.1 Spatial Resolution

Using the finite element model, we can calculate the spatial resolution of the microscope. From Eq. (5.18) we see that the important quantity is the electric field dot product $\mathbf{E}_1 \cdot \mathbf{E}_2$ contained in the integral. Near the probe tip, the electric field is strongest, falling off nearly to zero at the outer boundary of the model grid. Thus, most of the contribution to the integral will come from the region in the sample near the probe tip. For our purposes, we define the lateral spatial resolution to be $2r_{res}$, where the integral over the volume $V = \pi r_{res}^2 d$ under the probe tip is equal to half of the integral over the volume of the whole sample. For thin films, we take the depth d to be the thickness of the film, while for bulk samples, we choose $d = 2r_{res}$.

Figure 5.6 shows the calculated spatial resolution for both a 500 μm thick bulk dielectric sample, and for a 400 nm thin film on a 500 μm thick LAO substrate, for a typical probe with $r_0 = 0.4 \mu\text{m}$ and an aspect ratio $\alpha = 1.5$. We notice that the spatial resolution is the highest ($2r_{res} \sim 1$ to $1.3 \mu\text{m}$) for thin films; this value for $2r_{res}$ agrees with experimental results (see Sec. 4.4, and Sec. 5.7). At high permittivities, the spatial resolutions for bulk and thin film samples converge to about $1.5 \mu\text{m}$, which is approximately twice the tip bluntness of $2r_0 = 0.8 \mu\text{m}$. Model results show that the spatial resolution for any ϵ_r is approximately proportional to r_0 .

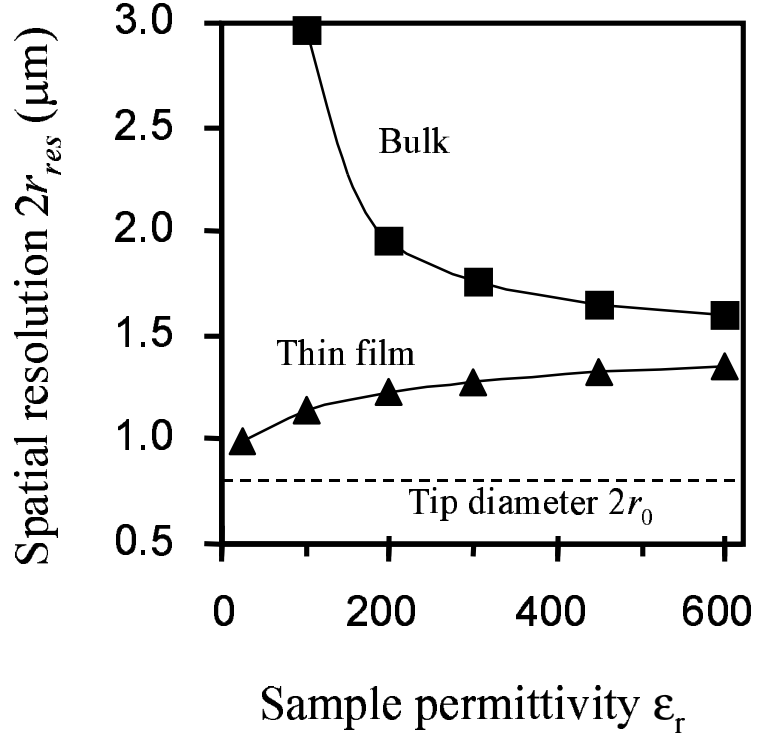


Figure 5.6: Spatial resolution of the microscope as a function of sample permittivity, for a probe tip with aspect ratio $\alpha = 1.5$ and radius $r_0 = 0.4 \mu\text{m}$ (see Fig. 5.1). These model results are given for a $500 \mu\text{m}$ thick bulk sample, and a 400 nm thin film on top of a $500 \mu\text{m}$ bulk LAO substrate.

5.6.2 Permittivity Tensor Directional Sensitivity

Again using the model, we can determine the directional sensitivity of the microscope to the permittivity tensor by finding the relative magnitude of the radial (I_r) and vertical (I_z) components of the integral in Eq. (5.18). This ratio is equal to

$$\frac{I_r}{I_z} = \frac{\int_{V_S} E_{r1} E_{r2} dV}{\int_{V_S} E_{z1} E_{z2} dV}, \quad (5.20)$$

where E_{r1} , E_{r2} , E_{z1} , and E_{z2} are the unperturbed and perturbed radial and vertical electric fields, respectively. This quantity I_r/I_z is shown in Fig. 5.7 as a function of sample permittivity for a 500 μm thick bulk dielectric and a 400 nm thin film on a 500 μm thick LAO substrate. As shown in the figure, for low-permittivity bulk samples, the normal (z) component of the permittivity tensor dominates, while for most thin films, the in-plane (radial) component dominates. However, this calculation is valid only for small deviations from the isotropic case.

We tested these model results by imaging a $5 \times 5 \times 10$ mm 0.1% Ce-doped $(\text{Sr}_x\text{Ba}_{1-x})_{1-y}(\text{Nb}_2\text{O}_5)_y$ (SBN) single crystal, with $x = 0.61$ and $y = 0.4993$. This anisotropic crystal has specified low-frequency permittivities of $\epsilon_{11} = 450$ and $\epsilon_{33} = 880$ [28]. We found that the microscope frequency shift was $\sim 5\%$ larger (more negative) when the probe was in contact with the face with ϵ_{33} in-plane, relative to when the probe was in contact with the face with ϵ_{11} in-plane; this agrees well with our model results, which predict a difference of 7%.

Another way to investigate the microscope's sensitivity to dielectric anisotropy is using Eq. 5.13, with $\epsilon_r^r \neq \epsilon_r^z$. Shown in Fig. 5.8(a) are the fields (equipotential lines) for an isotropic sample with $\epsilon_r^r = \epsilon_r^z = 50$. The fields for two anisotropic samples are shown in (b) and (c). In (b), ϵ_r^r is larger than ϵ_r^z , so that the electric field is oriented more in the vertical direction than in (a). In (c), ϵ_r^r is smaller

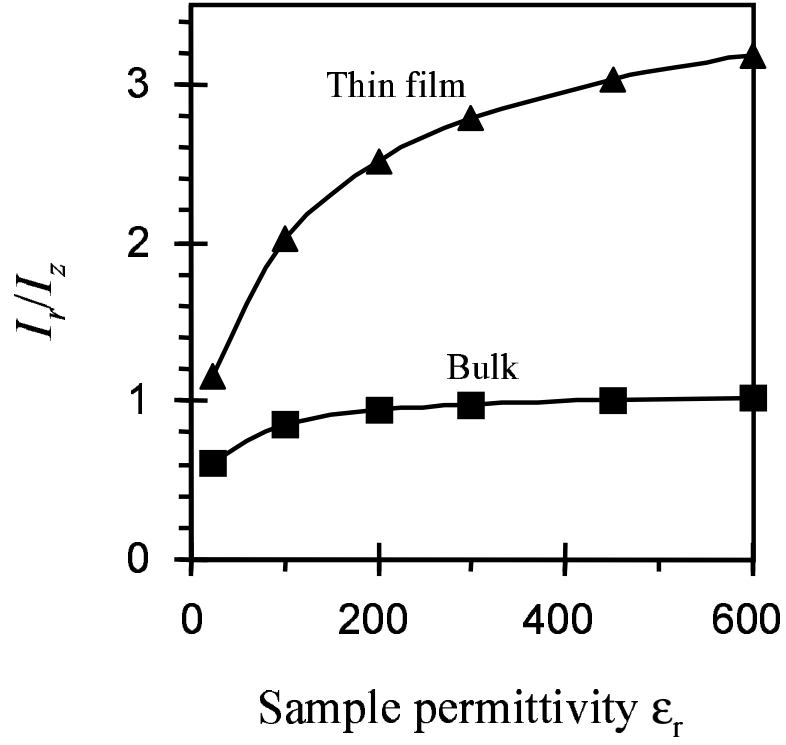


Figure 5.7: The directional sensitivity of the microscope to the sample's permittivity tensor. The ratio I_r/I_z gives the relative contribution of the radial (in-plane) to the vertical (normal) components of ϵ_r . Results are given for a 500 μm thick bulk sample, and a 400 nm thin film on top of a 500 μm bulk LAO substrate.

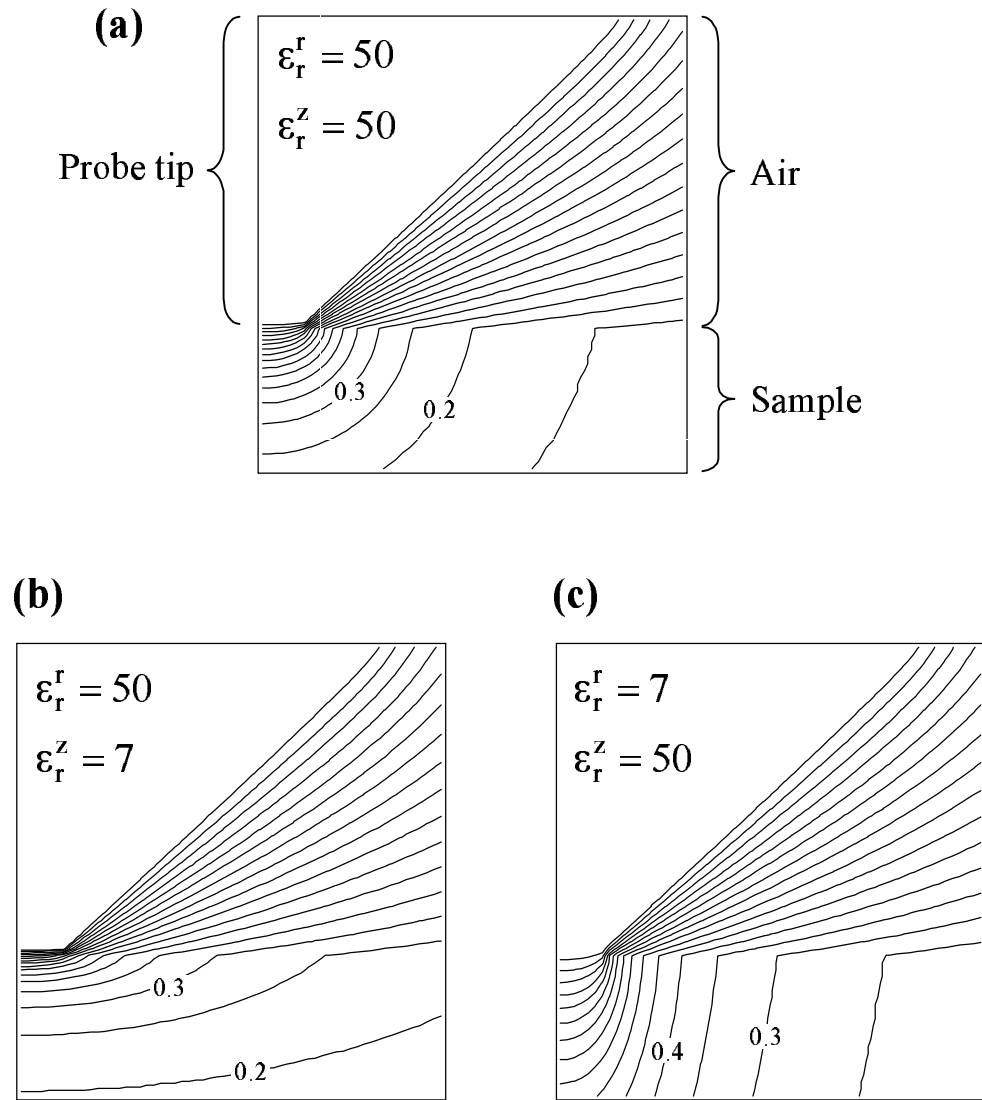


Figure 5.8: Calculated electric field near the probe tip for three different samples. The equipotential lines are shown; the electric field is perpendicular to these lines, and is largest where the lines are close together. (a) Isotropic sample with $\epsilon_r^r = \epsilon_r^z$. Anisotropic samples are shown in (b) and (c).

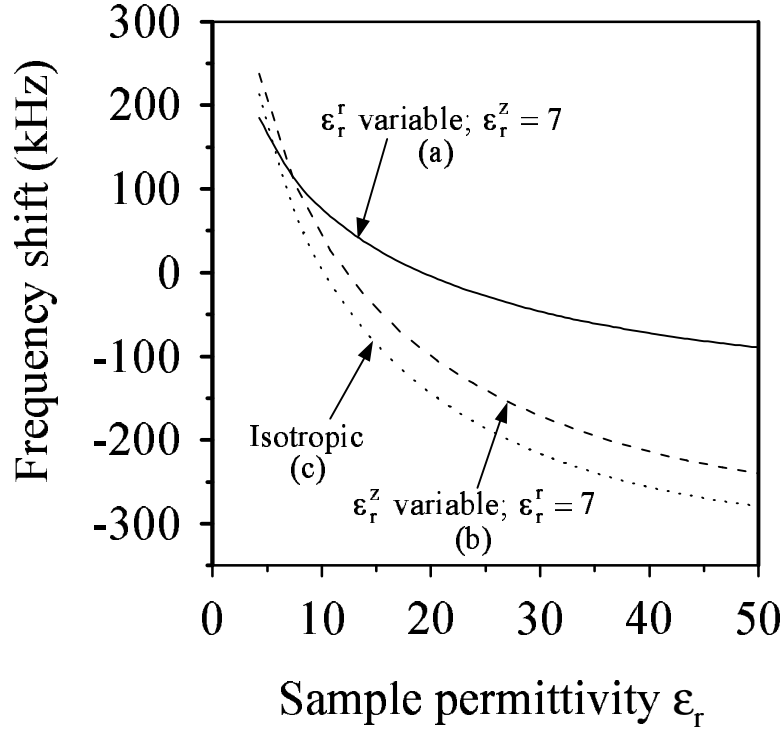


Figure 5.9: Model results for frequency shift vs. permittivity for some isotropic and anisotropic dielectric samples. Frequency shift is relative to a sample with $\epsilon_r^r = \epsilon_r^z$

than ϵ_r^z , so that the electric field is larger in the horizontal direction.

Model results for the frequency shift of the microscope are shown in Fig. 5.9 for some 5.5 mm thick anisotropic dielectric samples. Curve (a) indicates the frequency shift for a sample with ϵ_r^z fixed at 7, while ϵ_r^r is variable. Curve (b) indicates the frequency shift for ϵ_r^r fixed at 7, while ϵ_r^z is variable. Finally, curve (c) is for isotropic samples. The frequency shifts are relative to a sample with $\epsilon_r^r = \epsilon_r^z = 10$. Because the slope of curve (b) is larger than the slope of curve (c), the microwave microscope is more sensitive to changes in ϵ_r^z for these samples. This is in agreement with the “bulk” curve Fig. 5.7.

A second example of an anisotropic dielectric material is triglycine sulfate (TGS), which will be investigated in depth in Chapter 8. In TGS, ϵ_{11} and ϵ_{33} are virtually constant over a large temperature range, while ϵ_{22} is a strong function of temperature [49]. Curve (b) in Fig. 5.9 with ϵ_r^z variable will be used in Chapter 8 to compute quantitative permittivity in TGS.

5.6.3 Spherical Approximation for the Probe Tip

As an alternative to our finite element model, an analytic solution for the electric field near the probe tip can be found by approximating the probe tip as a sphere of radius r_{sph} , and assuming an infinite sample. This model has been used by X.-D. Xiang *et al.* at Lawrence Berkeley Labs for quantitative measurement of sample permittivity [39, 40]. Wanting to compare our finite element model with this analytic approximation, we tried replacing the blunt cone with a sphere in our finite element model. To obtain the correct dependence of frequency shift on sample permittivity, it was necessary to include a second fitting parameter, the radius r_0 of a flat area of the sphere in contact with the sample. The best fit of Δf vs. ϵ_r for one of our probes gave $r_{sph} = 14 \mu\text{m}$ and $r_0 = 0.4 \mu\text{m}$, as shown in Fig. 5.10(a).

The required radius r_{sph} of the sphere is surprisingly large, so we calculated the spatial resolution of such a probe using the method described in Sec. 5.6.2, for a 400 nm thin film with $\epsilon_r = 300$ on a LAO substrate. Shown in Fig. 5.10(b) is the integral inside a cylinder of radius r_{int} as a fraction of the total integral in Eq. 5.18, for a spherical tip and the corresponding conical tip. For the sphere-shaped probe, the spatial resolution was $2r_{res} = 3 \mu\text{m}$. The conical probe model giving the best fit of Δf vs. ϵ_r has $\alpha = 1.3$, giving a spatial resolution of $1.4 \mu\text{m}$ [see

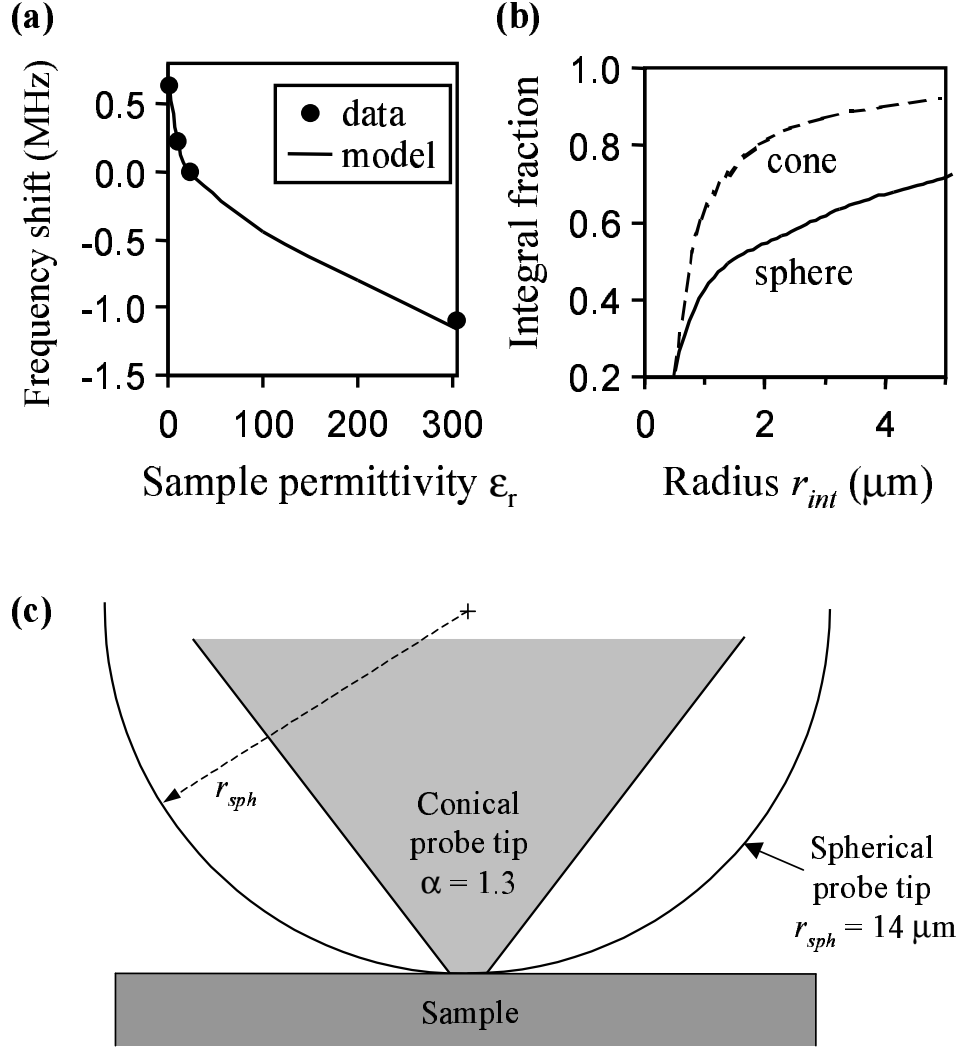


Figure 5.10: (a) Data vs. model results, using a spherical approximation for the probe tip, with $500 \mu\text{m}$ thick bulk dielectric samples. The spherical tip parameters are the sphere radius $r_{sph} = 14 \mu\text{m}$, and contact area radius $r_0 = 0.4 \mu\text{m}$. (b) The contribution to the electric field integral in Eq. 5.18 inside a radius r_{int} as a fraction of the total integral. Results are given for the sphere-shaped probe tip, and a blunt cone-shaped tip (with $\alpha = 1.3$), for a 400 nm thin film of permittivity $\epsilon_r = 300$ on a $500 \mu\text{m}$ thick LAO substrate. (c) Scale drawing showing a comparison between the conical and spherical probes.

Fig. 5.10(c)]. In addition, because of the slow fall-off of the integral as a function of radius for a spherical tip [Fig. 5.10(b)], imaging with such a tip would result in the smallest image features being smeared out to a diameter greater than $10\text{ }\mu\text{m}$. Since we do not observe this effect, and find our spatial resolution to be much closer to $1.4\text{ }\mu\text{m}$, we conclude that a cone is a much better approximation for the probe tip than a sphere, at least for the geometry of our system. We believe that this is due to the long-range nature of electromagnetism, where the potential due to a point charge diminishes at the rate $1/r$, causing the sides of the cone-shaped tip to have an important contribution to the frequency shift [113]. Figure 5.3(a) illustrates this effect, by showing that even at a distance of $6\text{ }\mu\text{m}$ from the axis, the electric field is relatively strong at the cone surface.

Also, a problem with an analytic solution using a sphere for the tip is the limitation to a single fitting parameter, the sphere radius r_{sph} . For our probe tips, it was not possible to obtain a reasonable fit with the data on a Δf vs. ϵ_r curve without an additional fitting parameter, such as the radius of a flat area on the sphere (a geometry which cannot be solved analytically).

These results are supported by the findings of other groups [51, 82, ?] which were unable to obtain agreement between their data and a model which represents the probe tip as a sphere. For example, to achieve reasonable agreement between model and theory, S. Hyun *et al.* had to introduce another fitting parameter to the spherical probe tip model, a sample-independent frequency shift offset, which they claim is due to the sides of the cone-shaped probe.

The assumption of an infinite sample [39, 40] can also pose problems. We find that this is an unrealistic assumption, because the properties of whatever is directly beneath the sample substrate can have a measurable effect on the

frequency shift of the microscope, which will affect quantitative imaging. We believe that a better approach is to have a bulk conducting ground plane beneath the sample in the experiment and also in the model, so that everything beneath this ground plane can be safely ignored.

5.7 Images of a (Ba,Sr)TiO₃ Thin Film

To demonstrate the usefulness of this quantitative permittivity imaging technique, we scanned a sample (see Fig. 5.11) consisting of a laser-ablated 370 nm thick Ba_{0.6}Sr_{0.4}TiO₃ (BST) thin film on a 70 nm La_{0.95}Sr_{0.05}CoO₃ (LSCO) counterelectrode. The substrate is LaAlO₃ (LAO). The films were deposited at 700 °C in 200 mTorr of O₂. The sheet resistance of the LSCO counterelectrode is about 400 Ω/□, sufficiently large to render it invisible at microwave frequencies.

Figure 5.12(a) shows a schematic diagram of a $76.5 \times 20 \mu\text{m}^2$ region of the thin film sample which we scanned. The gray-shaded areas indicate regions which were milled through the BST layer using a gallium focused ion beam (FIB). There is a $1 \mu\text{m}$ wide line and a corner of a $5 \mu\text{m}$ wide “frame” surrounding an untouched $20 \times 20 \mu\text{m}^2$ region. Fig. 5.12(b) shows a permittivity image of the region sketched in (a). The narrow line shows up as a wider band with low permittivity, a sign that the region near the line was damaged by the gallium ion beam tails [117] during milling. The wide frame appears as a double line in (b) due to edge effects at the edge of the milled area; also, the value of ϵ_r shown in this wide frame region is invalid, since there is no dielectric thin film there. Several low-permittivity regions appear randomly scattered over the scan area. As shown in Fig. 4.4, these probably are particles (“laser particles”) on the surface which accrued during pulsed laser deposition [94].

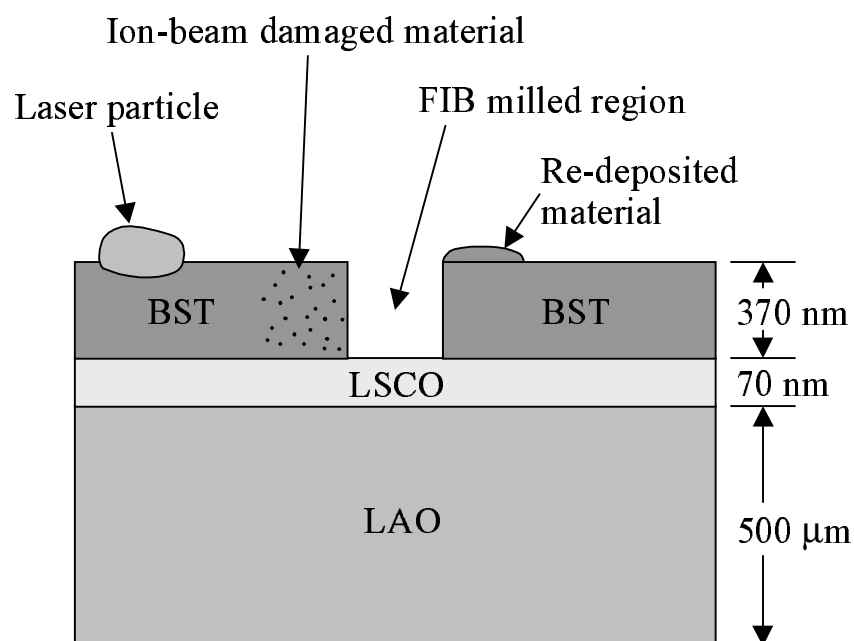


Figure 5.11: Cross-sectional schematic of a $\text{Ba}_{0.6}\text{Sr}_{0.4}\text{TiO}_3$ thin film sample. Also shown is typical defective regions, including laser particles, re-deposited material, and ion-beam damaged material.

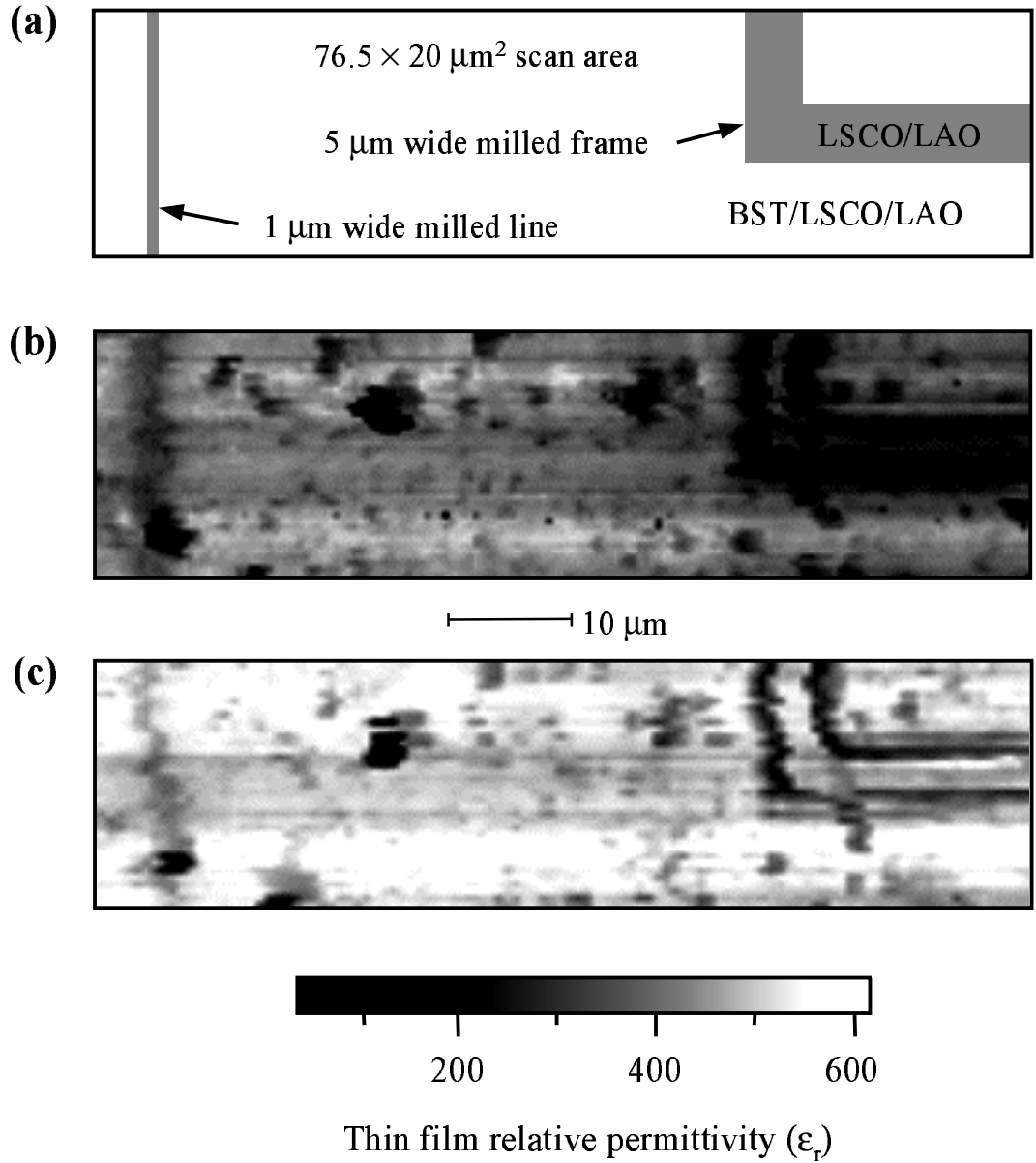


Figure 5.12: Images of a 370 nm thick $\text{Ba}_{0.6}\text{Sr}_{0.4}\text{TiO}_3$ (BST) thin film on a 70 nm $\text{La}_{0.95}\text{Sr}_{0.05}\text{CoO}_3$ (LSCO) counterelectrode on a LaAlO_3 (LAO) substrate. Images are of the same $76.5 \times 20 \mu\text{m}^2$ region. (a) Schematic diagram of the focused ion beam (FIB) milled regions in the scan region. (b) Scan of the thin film permittivity before annealing. (c) Thin film ϵ_r after annealing at 650 $^\circ\text{C}$ in air for 20 minutes.

After acquiring the image shown in Fig. 5.12(b), we annealed the sample at 650 °C in air for 20 minutes. Afterward, we scanned the same region again; the resulting image is shown in (c). The overall thin film permittivity has increased between (b) and (c), and the narrow line has become less prominent, indicating that perhaps the permittivity of the damaged region was partially restored.

In addition, using the size of the smallest features visible in Fig. 5.12, we again find the spatial resolution to be 2 μm or better, in agreement with our theoretical results in Sec. 5.6.1.

5.8 Sensitivity to Permittivity

We found the sensitivity of the microwave microscope by observing the noise in the dielectric permittivity and tunability data. For a 370 nm thin film on a 500 μm thick LAO substrate, with an averaging time of 40 ms, we found that the permittivity sensitivity is $\Delta\epsilon_r = 2$ at $\epsilon_r = 500$.

Chapter 6

Nonlinear Dielectric Imaging

6.1 Introduction

Dielectric nonlinearity, or the dependence of permittivity on electric field, is another property of interest for dielectric materials. For example, electrically-tunable microwave electronics, such as filters and phase shifters, rely on the nonlinear characteristics of paraelectric materials [1, 23, 73]. Dielectric nonlinearity is also useful in the investigation of ferroelectric critical phenomena, where nonlinearity reaches a maximum near the Curie temperature [69].

Several different methods are available for measuring dielectric nonlinearity. The most common method is to use thin-film capacitors, such as interdigital electrodes or parallel-plate capacitors. The linear permittivity is measured through the capacitance by applying an ac voltage to the electrodes [41]; by applying a dc voltage in addition to the ac voltage, one can also measure dielectric nonlinearity [46, 49, 72]. This method is useful for frequencies up to ~ 1 MHz.

A second method is to apply an ac voltage to a sample, and measure the component of the permittivity at higher harmonics of the fundamental measurement frequency. This method can be readily applied to the traditional capacitive

measurements [69]. It can also be used at higher frequencies, such as microwave [103] or optical frequencies [89]. A disadvantage of this method is that it requires a high-bandwidth measurement system. For example, if the measurement frequency is at 8 GHz, the system must be able to simultaneously operate at 16 GHz for the second harmonic, and 24 GHz for the third harmonic. However, some components in our system have low bandwidth, such as the directional coupler (7–12.4 GHz) and isolators between the microwave source and decoupler (5–10 GHz). A solution would be to use higher-bandwidth components.

A third method is to measure the permittivity at high frequency (eg., microwave frequencies), and simultaneously apply a lower-frequency ac voltage to the sample. Dielectric nonlinearity can then be measured by monitoring harmonics of the ac signal. For example, one could measure the permittivity at 8 GHz, while applying an ac voltage at 1 kHz. The dielectric nonlinearity would be measured by monitoring the component of the permittivity at 1 kHz for the first harmonic, and 2 kHz for the second harmonic. This method, introduced by Cho *et al.* [24], was the method which we adopted for our measurements. The advantage over the second method above is that we do not need a high-bandwidth system.

6.2 Measuring Dielectric Nonlinearity

To measure dielectric nonlinearity, we use a bias tee in the resonator to apply a dc or low-frequency voltage bias to the sample (see Sec. 4.2). A grounded metallic layer beneath the thin film acts as a counterelectrode, as shown in Fig. 6.1. In order to prevent the counterelectrode from dominating the microwave measurement, we use a high-sheet-resistance counterelectrode, making it virtually

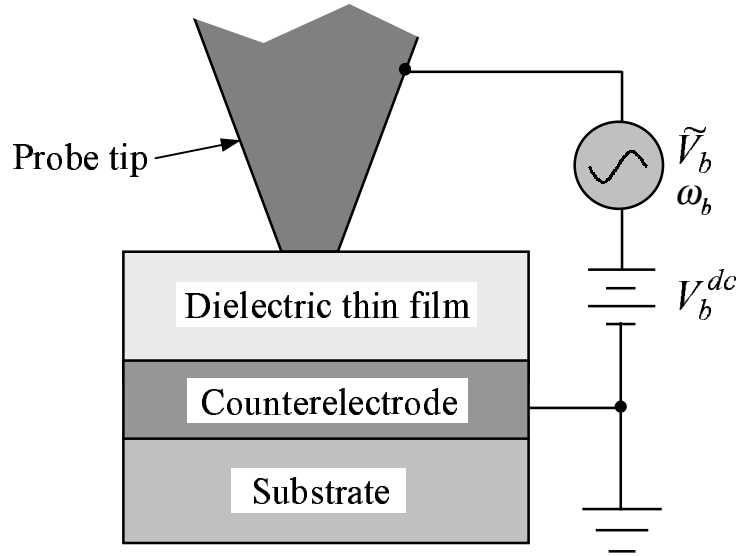


Figure 6.1: Schematic showing the nonlinear dielectric measurement setup for a thin film sample. A bias tee in the microscope resonator allows a voltage bias to be applied to the probe tip. The applied bias can have both dc and ac components.

invisible to the microwave fields. This is illustrated in Fig. 3.3(b), which shows that at high sheet resistances the frequency shift saturates at a value dependent only on the substrate. As a result, the presence of the thin-film counterelectrode can be safely ignored in the finite-element model described in Chapter 5.

Because the counterelectrode is immediately beneath the dielectric thin film, the applied electric field is primarily in the vertical direction, unlike the microwave electric field, which is mainly in the horizontal direction for thin films with large permittivities (Fig. 5.6.2). Figure 6.2 shows the low-frequency electric field distribution beneath the probe tip, as calculated using the finite-element model presented in Sec. 5.2.2. As shown in this figure, the electric field beneath the probe tip is mainly in the vertical direction, and is quite uniform. Thus, we can assume that the bias electric field is $E_b = V_b/t_f$, where t_f is the thickness of the dielectric thin film, and V_b is the bias voltage.

An example of frequency shift vs. bias voltage is shown in Fig. 6.3(a). The sample was the same as that described in Sec. 5.12: a 370 nm thick $\text{Ba}_{0.6}\text{Sr}_{0.4}\text{TiO}_3$ (BST) thin film on a 70 nm $\text{La}_{0.95}\text{Sr}_{0.05}\text{CoO}_3$ (LSCO) counterelectrode on a LaAlO_3 (LAO) substrate. The sheet resistance of the LSCO layer is approximately $400 \, \Omega/\square$, sufficiently large to render it invisible at microwave frequencies. The small amount of hysteresis seen in Fig. 6.3 is probably due to the broadened transition temperature of the nominally paraelectric thin film.

For imaging purposes, it is useful to measure the nonlinearity without having to sweep the bias voltage and acquire multiple data points at each location on a sample, as was done in Fig. 6.3. This is accomplished by modulating the bias voltage and using a lock-in amplifier referenced at the bias modulation rate ω_b

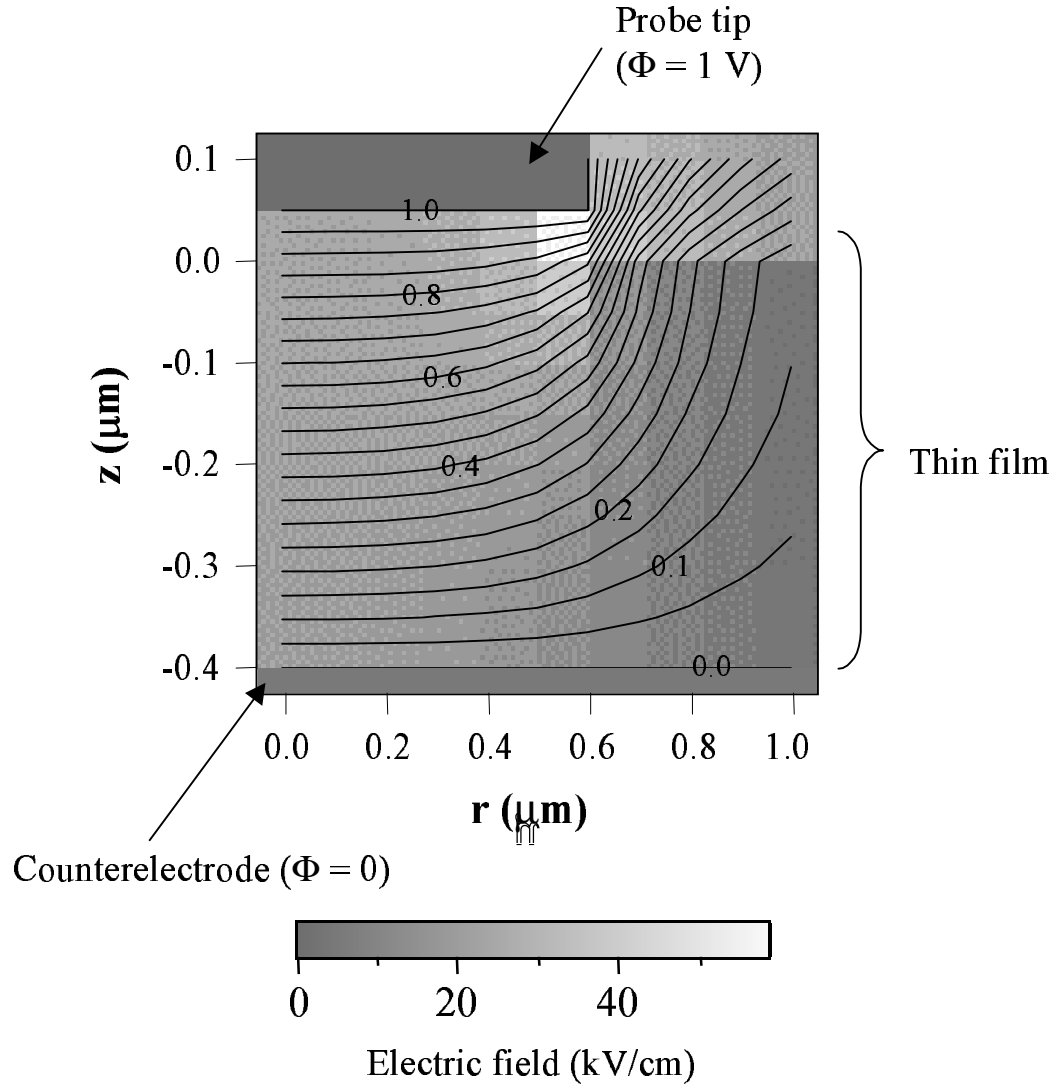


Figure 6.2: The low-frequency electric potential beneath the probe tip in a 400 nm thin film with permittivity $\epsilon_r = 300$. The equipotential lines are shown; electric field lines are perpendicular to these. The bottom surface of the probe tip doesn't exactly line up with the discontinuity in the equipotential lines due to the 50 nm cell size used in the calculation. The labels show the potential at each line.

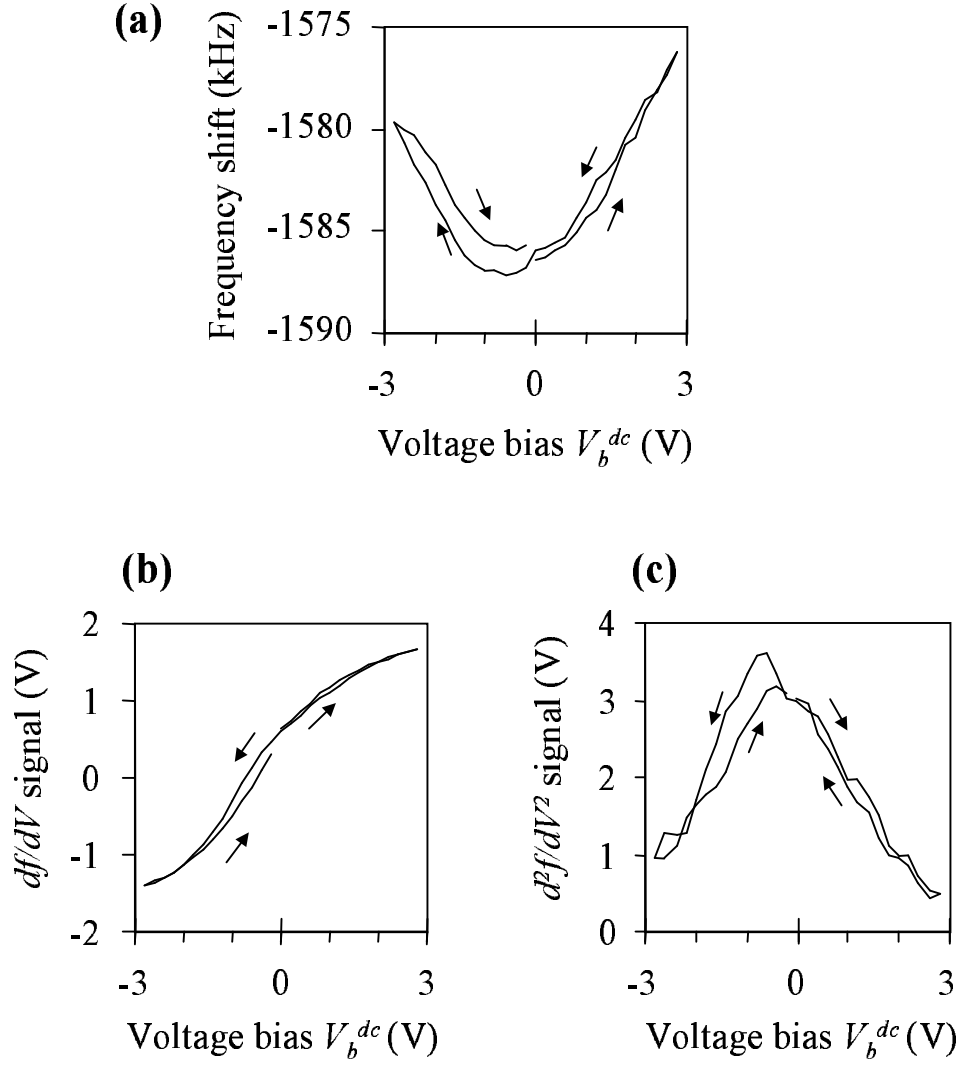


Figure 6.3: Dielectric nonlinearity at one point on the BST/LSCO/LAO thin-film sample. (a) Frequency shift Δf , which is related to the permittivity ϵ_r ; (b) first derivative df/dV ; and (c) second derivative d^2f/dV^2 .

(Fig. 6.1). If the bias voltage as a function of time is

$$V_b = V_b^{dc} + \tilde{V}_b \cos \omega_b t, \quad (6.1)$$

then a lock-in amplifier referenced at ω_b , with the Δf as its input, will output a signal proportional to the derivative of the Δf vs. bias curve shown in Fig. 6.3(a). This derivative signal, which we call “ df/dV ,” is shown in Fig. 6.3(b) as a function of V_b^{dc} . Finally, the second derivative of the Δf vs. bias voltage curve can be extracted using a lock-in amplifier referenced at $2\omega_b$, as shown in (c). The signals df/dV and d^2f/dV^2 are related to the dielectric nonlinearity, as described below.

6.3 Quantitative Dielectric Nonlinearity

Dielectric nonlinearity data are more useful if they are quantitative. The permittivity of the BST thin-film sample, calculated from the data in Fig. 6.3(a) using the method described in Chapter 5, is shown in Fig. 6.4. The permittivity of the BST thin film decreases when an electric field is applied, which is the expected result [13, 46].

To learn about quantitative dielectric nonlinearity, we expand the electric displacement \mathbf{D} in powers of the electric field \mathbf{E} , and keep only the nonzero terms [24]:

$$D_1(\mathbf{E}) = \epsilon_{11}E_1 + \frac{1}{2}\epsilon_{113}E_1E_3 + \frac{1}{6}\epsilon_{1133}E_1E_3^2 + \dots \quad (6.2)$$

We take E_1 to be the rf electric field, which is primarily in the r direction (see Sec. 5.6.2), and $E_3 = E_b$ to be the bias electric field, which is in the z direction.

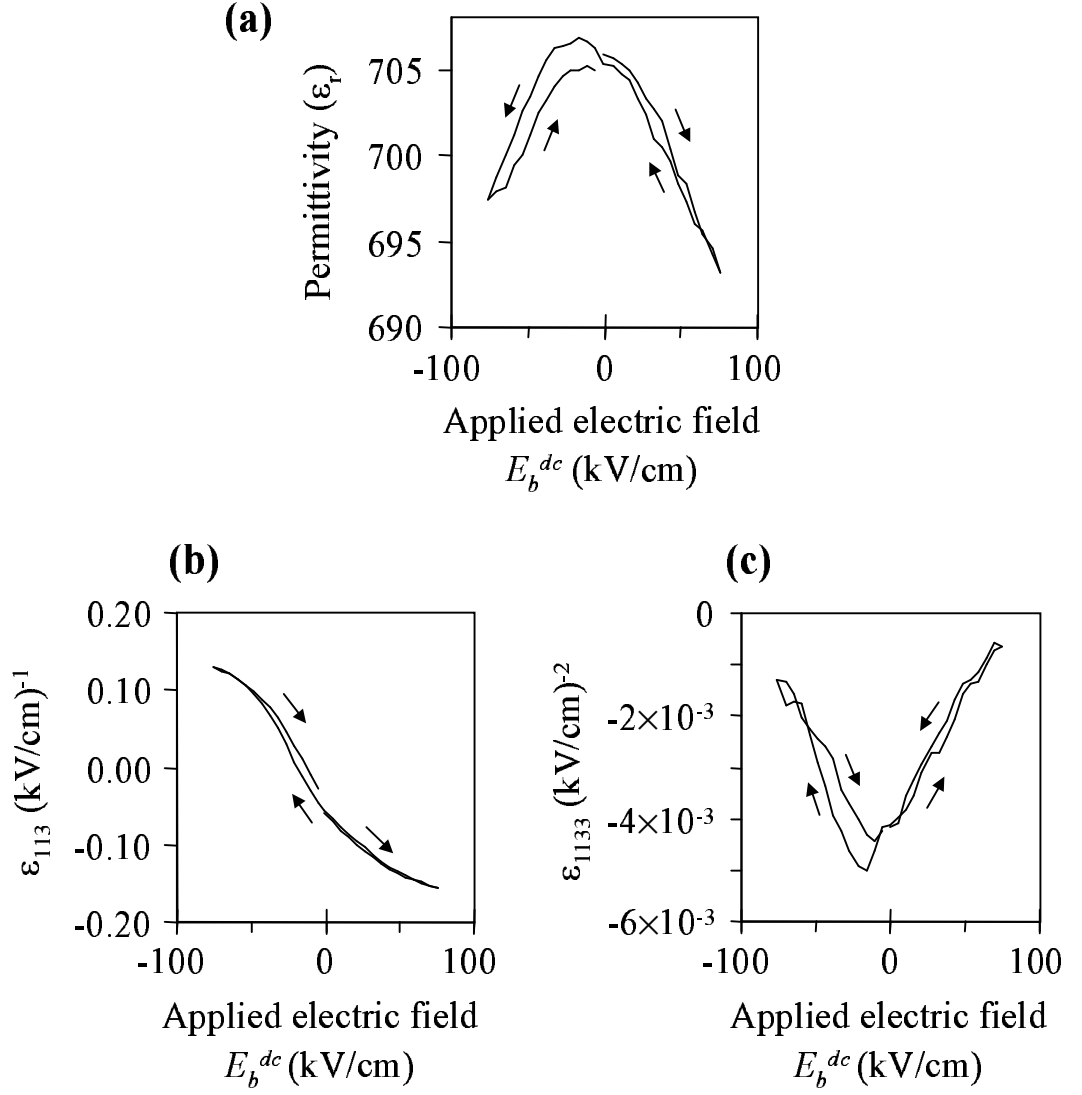


Figure 6.4: Quantitative dielectric nonlinearity at one point on the BST/LSCO/LAO thin film sample. (a) Linear permittivity ϵ_r ; (b) first nonlinear dielectric constant ϵ_{113} ; and (c) second nonlinear dielectric constant ϵ_{1133} .

Adding a low-frequency oscillatory component ($\omega_b = 1$ kHz, with an amplitude of $\tilde{V}_b = 1$ V, in our case) to the bias voltage, the applied electric field is

$$E_3 = E_b^{dc} + \tilde{E}_b \cos \omega_b t. \quad (6.3)$$

Substituting Eq. 6.3 in Eq. 6.2, we find that the effective rf permittivity is then

$$\begin{aligned} \epsilon_{rf} = \frac{D_1}{E_1} &= \epsilon_{11} + \frac{1}{2}\epsilon_{113}E_b^{dc} + \epsilon_{1133} \left(\frac{(E_b^{dc})^2}{6} + \frac{(\tilde{E}_b)^2}{12} \right) \\ &+ \left(\frac{\epsilon_{113}}{2} + \frac{\epsilon_{1133}E_b^{dc}}{3} \right) \tilde{E}_b \cos(\omega_b t) \\ &+ \frac{1}{12}\epsilon_{1133}\tilde{E}_b^2 \cos(2\omega_b t) + \dots \end{aligned} \quad (6.4)$$

We note that the components of ϵ_{rf} at ω_b and $2\omega_b$ are approximately proportional to the nonlinear dielectric constants ϵ_{113} and ϵ_{1133} , respectively. Expanding the resonant frequency of the microscope as a Taylor series about $f_0(\epsilon_{rf} = \epsilon_{11})$, we have

$$f_0[\epsilon_{rf}(t)] = f_0(\epsilon_{11}) + \left. \frac{df_0}{d\epsilon_{rf}} \right|_{\epsilon_{rf}=\epsilon_{11}} [\epsilon_{rf}(t) - \epsilon_{11}] + \dots \quad (6.5)$$

Substituting Eq. 6.4 into Eq. 6.5, and keeping only the larger terms,

$$\begin{aligned} f_0(t) &\approx \text{constant} + \frac{1}{2}\epsilon_{113}\tilde{E}_b \left. \frac{df_0}{d\epsilon_{rf}} \right|_{\epsilon_{11}} \cos(\omega_b t) \\ &+ \frac{1}{12}\epsilon_{1133}\tilde{E}_b^2 \left. \frac{df_0}{d\epsilon_{rf}} \right|_{\epsilon_{11}} \cos(2\omega_b t). \end{aligned} \quad (6.6)$$

Thus, the components of the frequency shift signal at ω_b and $2\omega_b$ can be extracted to determine the nonlinear dielectric constants ϵ_{113} and ϵ_{1133} . These nonlinear quantities can be measured simultaneously with the linear permittivity (ϵ_{11}) while scanning.

The resulting nonlinear dielectric data are shown in Fig. 6.4(b) and (c). Because these data are extracted by modulating V_b , the noise in (b) is less than that in (a). We notice that ϵ_{113} is close to zero for zero applied field, which would be

expected for a material with no spontaneous polarization [24]. In addition, we expect the sign of ϵ_{113} to be sensitive to the direction of the polarization (but not necessarily the magnitude of the polarization), which is evident in (b) (see Sec. 7.2). The second nonlinear dielectric constant, ϵ_{1133} , on the other hand, is nonzero at zero applied field. The curves in Fig. 6.4 are centered at a nonzero field ~ -20 kV/cm, probably because the asymmetric capacitor electrodes induce unequal charges at the two electrodes [3, 72, 94], which in turn leads to a spontaneous internal field in the film, here on the order of 20 kV/cm. The observed tunability of ϵ_r as shown in Fig. 6.4(a) is small ($\sim 2\%$) probably because we are measuring an off-diagonal nonlinear component of the permittivity tensor (ϵ_{113}): the applied field is in the vertical direction, while the microwave measurement is sensitive mainly to the horizontal component of permittivity [94].

6.4 Nonlinear Dielectric Images

In order to obtain an image of dielectric nonlinearity, we apply a nonzero dc voltage bias. The derivative signal (df/dV) is then nonzero for a nonlinear dielectric, as shown in Fig. 6.3(b). Thus, the magnitude of df/dV should be related to the dielectric nonlinearity. This df/dV signal, along with d^2f/dV^2 , can be acquired simultaneously with the frequency shift signal Δf using lock-in amplifiers referenced at ω_b and $2\omega_b$, respectively.

In Fig. 5.12, we showed permittivity images of the 370 nm thick BST thin film on a 70 nm LSCO counterelectrode on a LAO substrate. Shown in Fig. 6.5 are nonlinear dielectric images which were acquired simultaneously with the linear dielectric images shown in Fig. 5.12. For these images in Fig. 6.5, a dc bias of -3.5 V was applied to the probe tip, giving an average vertical dc electric field of

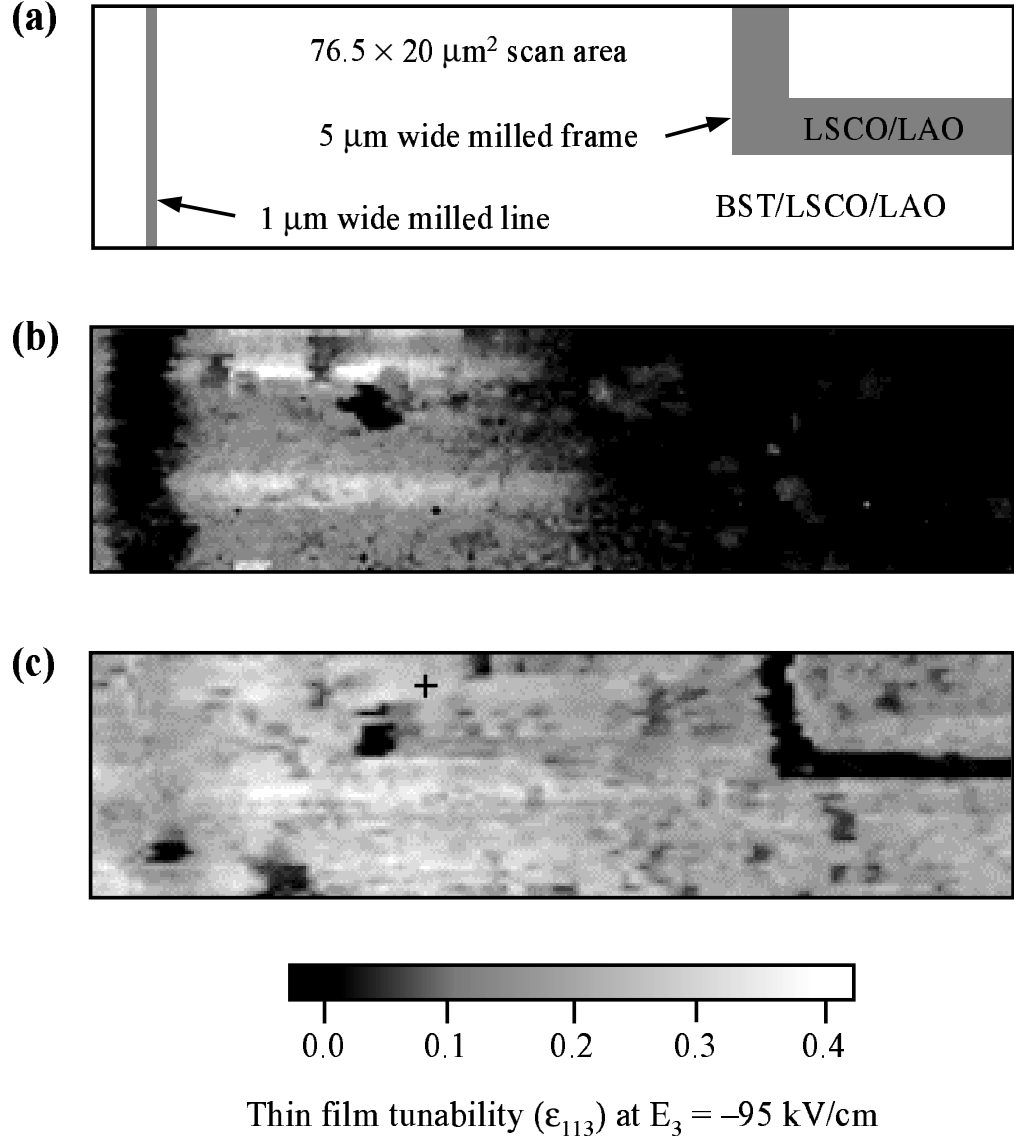


Figure 6.5: Nonlinear dielectric images of the BST/LSCO/LAO thin film sample. (a) Schematic diagram of the focused ion beam (FIB) milled regions in the $76.5 \times 20 \mu\text{m}^2$ scan region. (b) Thin film tunability as shown in the nonlinear dielectric constant ϵ_{113} , before annealing. The low-tunability regions were damaged during FIB milling. (c) Nonlinear dielectric (ϵ_{113}) image after annealing, showing that the tunability has been restored.

-95 kV/cm in the BST thin film. Figure 6.5(b) was acquired before the sample was annealed, and shows that the tunability has been destroyed near the narrow FIB milled line, and over a large area within about $12\text{ }\mu\text{m}$ of the FIB milled frame. Figure 6.5(c), which was acquired after annealing the sample at $650\text{ }^{\circ}\text{C}$ in air for 20 minutes, shows that the tunability has been restored in the damaged regions, and slightly improved in the undamaged regions.

6.5 Other Methods of Applying a Bias

As an alternative, the electric field \mathbf{E}_b could be applied in the horizontal direction using thin film electrodes, such as interdigital electrodes, deposited on top of the dielectric thin film. The advantage in this case is that diagonal nonlinear permittivity tensor terms could be measured, such as ϵ_{111} and ϵ_{1111} ; however, we have found that the electrodes themselves contribute to the frequency shift, causing the calculated value of ϵ_r to be too large. Another disadvantage is that imaging is limited to the small gap between the electrodes.

Another method, which is applicable to bulk crystals, is to have no counter-electrode. Because of the sharpness of the probe tip, if no metallic structures are within a couple of microns of the tip, it simply does not matter what is grounded. In this case, the electric field near the probe tip depends on the radius and shape of the tip, rather than on the distance to ground. For a sample that is at least 0.5 mm thick, it does not make a difference whether the sample holder is grounded. This method will be used to look at dielectric nonlinearity in crystals in Chapter 7.

6.6 Sensitivity to Dielectric Nonlinearity

We found the sensitivity of the microwave microscope to dielectric nonlinearity by observing the noise in the ϵ_{113} data. For a 370 nm thin film on a 500 μm thick LAO substrate, with an averaging time of 40 ms, we found that the nonlinearity sensitivity is $\Delta\epsilon_{113} = 10^{-3} \text{ (kV/cm)}^{-1}$.

Chapter 7

Imaging of Domains in Ferroelectric Crystals

7.1 Introduction

Many methods are available for imaging of ferroelectric domains. Two of the oldest include etching with a substance that preferentially etches domains with one direction of polarization, and the powder technique, where a colloidal suspension of charged particles, of a type which is attracted to domains with one orientation, is allowed to evaporate [54]. Numerous other methods have been used as well. An optical microscope with crossed polarizers can be used to view domains due to the effects of optical birefringence (for 90° domains) and optical rotation (for 180° domains) [65]. Laser scattering can be used, because the index of refraction of domain boundaries is different from the domain's interior [85]. Secondary electrons in scanning electron microscopy are sensitive to the surface potential variations that occur at different domains [15]. X-ray topography can be used due to variations in the Bragg angle from one domain to the next [100]. Nematic liquid crystals in a layer on top of the crystal will align with the polarization, allowing viewing of the domain structure with crossed polarizers [106]. A pyroelectric probe involves locally heating the sample with a laser, and detecting the

sign of the pyroelectric current [76]. Second harmonic generation of reflected light is sensitive to the direction of polarization relative to the incident beam, when the beam is at an angle to the surface [18]. Finally, electrostatic force microscopy can be used to image domains by measuring the local sign of the piezoelectric coefficient [38].

We also are able to image ferroelectric domains with our microwave microscope. While our method is slower, and has lower spatial resolution than most other techniques, this measurement was useful because we can use the same instrument for both ferroelectric domain imaging and for our other measurements, such as microwave permittivity. Because of the limited spatial resolution of the microscope ($\sim 1 \mu\text{m}$), we could not observe domains in thin-film samples, which are generally less than $1 \mu\text{m}$ across [38]; however, the larger domain widths in crystals permitted ferroelectric domain imaging in crystals.

Ferroelectric domain imaging is based on the nonlinear dielectric measurement method described in Chapter 6. With thin films, it was possible to apply a dc or low-frequency electric field beneath the probe tip by biasing the tip and grounding a metallic counterelectrode beneath the film. With crystals, we do not have this luxury. However, as mentioned in Sec. 6.5, a grounded counterelectrode is not required for application of an electric field to the sample, due to the sharpness of the probe tip. This is demonstrated in Fig. 5.8(a), where the electric field is shown for a 5.5 mm thick bulk dielectric sample. In addition, I found experimentally that the measured dielectric nonlinearity in a bulk sample is unaffected by grounding the metallic sample holder or leaving it floating. Although somewhat surprising, this can be understood as follows: the length scale of the concentrated electric field near the probe tip is on the order of $1 \mu\text{m}$; anything

which is far beyond this length scale can be considered to be at infinity, including the metallic sample holder and the probe's outer conductor. The disadvantage of having no grounded counterelectrode within $\lesssim 1 \mu\text{m}$ beneath probe tip is that the electric field is no longer uniform, and dielectric nonlinearity can no longer be measured quantitatively, as was done in Sec. 6.3.

7.2 Determining the Sign of Polarization

To investigate the measurement of the direction of polarization, I scanned a 0.5 mm thick periodically-poled LiNbO₃ sample. As specified by the manufacturer [29], and confirmed with an optical microscope, the ferroelectric domains are 15 μm across, and are in the shape of stripes across the sample (Fig. 7.1). The polarization alternates from domain to domain and is perpendicular to the plane of the large face of the sample. Lithium niobate is a hard ferroelectric, meaning that the polarization cannot be switched even with a strong electric field. The Curie temperature is very high, at 1143 °C.

Figure 7.2(a) shows hysteresis loops that were acquired at two different domains. For these data, the frequency shift was acquired while the voltage bias was swept continuously in a triangle wave at a frequency 2.02 Hz, with an amplitude of 100 V. Forty consecutive hysteresis loops were averaged.

The curves in Fig. 7.2(a) have the same shape, except that they are shifted along the horizontal axis. This shifting can be explained using Fig. 7.2(b), which shows a cross-sectional schematic of the sample with two different ferroelectric domains, with polarization up and down. Because of the discontinuity in the polarization \mathbf{P} at the surface of the sample, an effective charge σ is at the surface of the sample, given by $\sigma = \mathbf{P} \cdot \hat{\mathbf{n}}$, where $\hat{\mathbf{n}}$ is a unit vector normal to the surface.

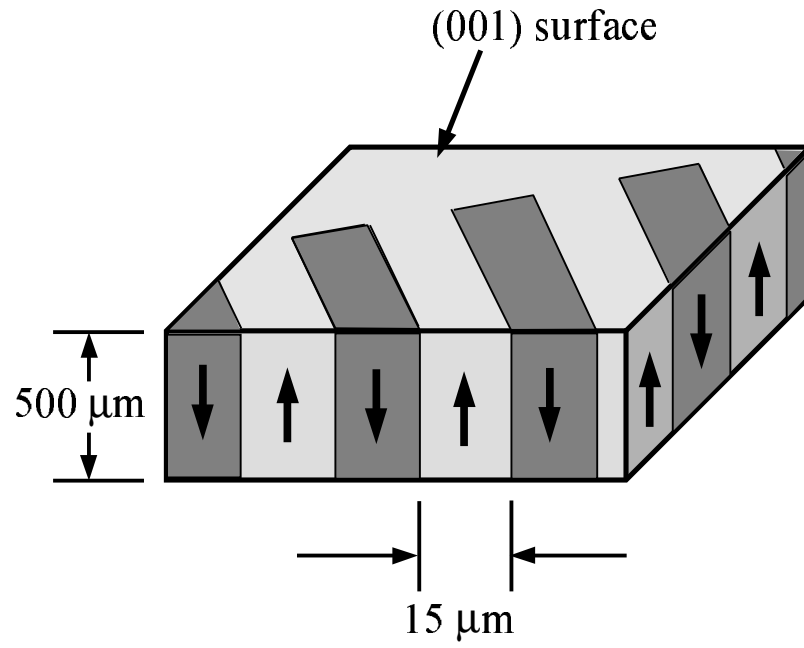


Figure 7.1: Schematic of the region of the periodically-poled LiNbO₃ crystal which was imaged in Fig. 7.3, showing the alternating polarizations of adjacent domains.

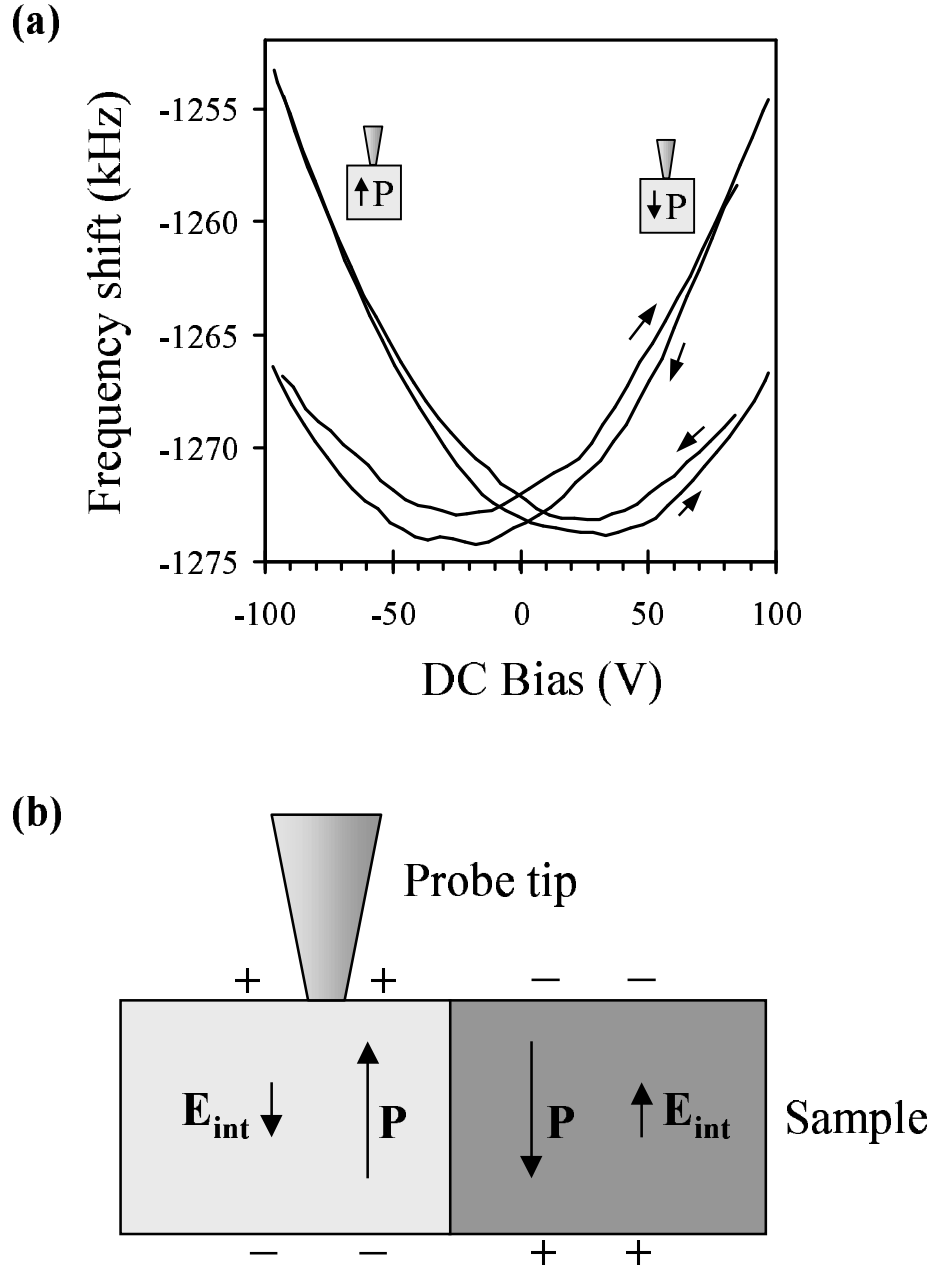


Figure 7.2: (a) Hysteresis loops at two different domains in LiNbO_3 . (b) Schematic of a cross-section of neighboring domains in LiBbO_3 , showing the polarization \mathbf{P} , and the internal depolarization field \mathbf{E}_{int} which results from the effective surface charge.

This surface charge σ produces an effective internal depolarization field $E_{int} = \sigma/\epsilon_0 = P/\epsilon_0$ in the sample, in the direction opposite \mathbf{P} . This internal electric field causes the curves shown in Fig. 7.2(a) to be shifted along the horizontal axis in a direction which is dependent on the local polarization. For LiNbO_3 , with a spontaneous polarization $P_s = 0.71 \text{ C/m}^2$, this would give a huge internal field of $E_{int} = 8.0 \times 10^5 \text{ kV/cm}$. In reality, opposite charges are expected to be attracted to the surface, thereby cancelling most of this internal field. In Fig. 7.2, the shifts of the curves along the horizontal axis are about $\pm 25\text{V}$; using the finite element model (see Chapter 5), we calculate the corresponding average dc field in a $1 \mu\text{m}^3$ volume under the probe tip to be approximately 150 kV/cm . Thus, we believe that the total internal field in the sample is about 150 kV/cm , rather than $8.0 \times 10^5 \text{ kV/cm}$, due to the effect of surface charge cancellation. Additionally, neighboring domains may cause the internal field to have a horizontal component, also contributing to the reduction the vertical component of the internal field.

In order to acquire images of ferroelectric domains, it is preferable to measure the direction of polarization without sweeping the electric field. To accomplish this, we fix the dc voltage bias at 0 V , and oscillate the electric field with an amplitude \tilde{V}_b (see Sec. 6.2) at a frequency $\omega_b \sim 1 \text{ kHz}$. We extract the slope (which we call df/dV) of the Δf vs. bias voltage curve using a lock-in amplifier referenced at ω_b . As shown in Fig. 7.2, a positive value for the slope indicates a region with polarization down, while a negative slope means the polarization is up.

7.3 Ferroelectric Domain Images

7.3.1 Lithium Niobate

Shown in Fig. 7.3(b) is an image of an $80 \times 80 \mu\text{m}^2$ region of the LiNbO_3 sample. As shown in the color bar, the shades of gray indicate the derivative signal df/dV . The white areas have $df/dV < 0$, meaning the polarization is up, while the black areas have polarization down. Fig. 7.3(d) is an image of the opposite face of the same sample. The black areas in (b) are white in (d), and the white areas in (b) are black in (d), proving that this measurement is sensitive to the vertical component of polarization. The large diagonal feature seen in Fig. 7.3(c) and (d) is a scratch on the surface of the sample, which can be observed with an optical microscope.

Figure 7.3(a) shows a frequency shift image of the same region as (b), while (c) is a frequency shift image of the same region as (d). The permittivity of different domains appears to be the same, regardless of the direction of polarization. However, the domain boundaries clearly appear in these frequency shift images. In addition, images acquired by Ray Anthracite with the microwave microscope show an increase in the Q at the domain boundaries. Following a suggestion by Professor Ichiro Takeuchi that these effects could be due to sample topography, I acquired atomic force microscope images of the sample, which show that a 60 nm high step of width ≤ 200 nm exists at the domain boundaries. Thus, the change in frequency shift and increase in Q at the domain boundaries could be due to less material being near the probe tip when it approaches a downward step at domain boundaries. Similar topographic features have been observed on the surface of PbTiO_3 [116].

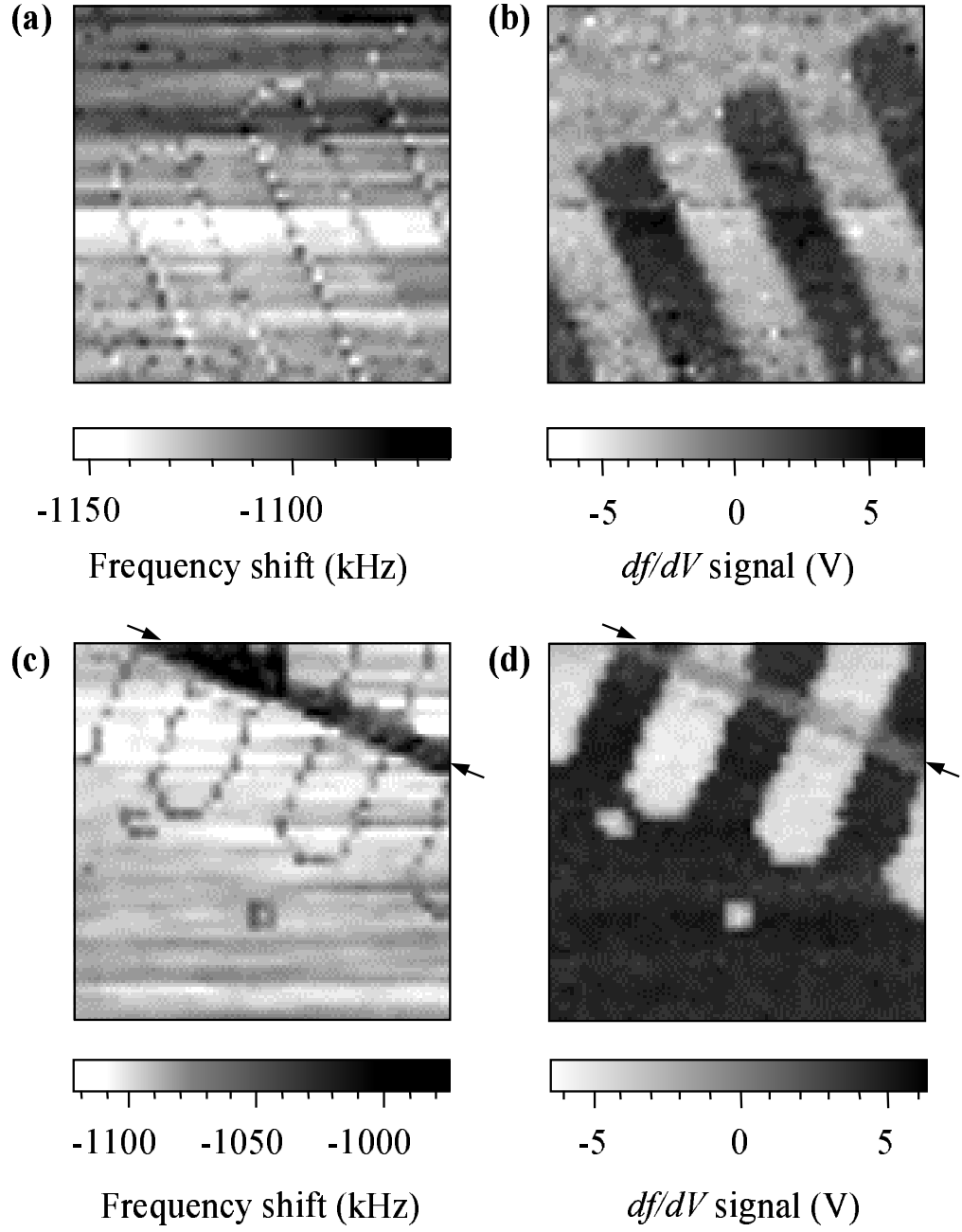


Figure 7.3: Images showing permittivity contrast [(a) and (c)] and domain structure [(b) and (d)] in a $80 \times 80 \mu\text{m}^2$ region of a LiNbO_3 crystal. The images shown in (c) and (d) are of the opposite face to that shown in (a) and (b). The arrows in (c) and (d) show the location of a scratch on the surface of the crystal.

7.3.2 Barium Titanate

Figure 7.4(a) shows an optical photograph of a region of a BaTiO_3 crystal, showing long narrow domains which join together at $\sim 90^\circ$ near the center of the photograph. Figure 7.4(b) shows a microwave microscope image of a similar region on the sample, showing a similar structure to (a). The image in (b) differs from Fig. 7.3(b) and (d), in that the df/dV signal does not change sign at neighboring domains. Instead, the black areas have $df/dV > 0$, while the white areas have $df/dV \sim 0$. This can be explained using Fig. 7.4(c), which shows a cross-sectional schematic of a crystal with 90° domains. Neighboring domains alternately have polarization in the horizontal direction and vertical direction. Thus, the white regions in Fig. 7.4(c) have polarization down, while the black regions have horizontal polarization. Regions with horizontal polarization have no surface charge due to the absence of a discontinuity in the normal component of the polarization at the crystal surface, and hence no internal field to cause the shifting of the curves shown in Fig. 7.2.

An important point is that unless a crystal is a hard ferroelectric like LiNbO_3 , the modulated electric field amplitude \tilde{V}_b cannot be arbitrarily large, since a large electric field will switch the polarization, possibly altering the domain structure, and removing polarization information from the df/dV signal. For the image shown in Fig. 7.4(c), $\tilde{V}_b = 3$ V was sufficiently small.

7.3.3 Deuterated Triglycine Sulfate

Shown in Fig. 7.5 are domain images of a 5.5 mm thick deuterated triglycine sulfate (DTGS) crystal, acquired at 307 K. (For more about DTGS, see Chapter 8.) The images show a $20 \times 20 \mu\text{m}^2$ region of the sample. The $[010]$ axis, which

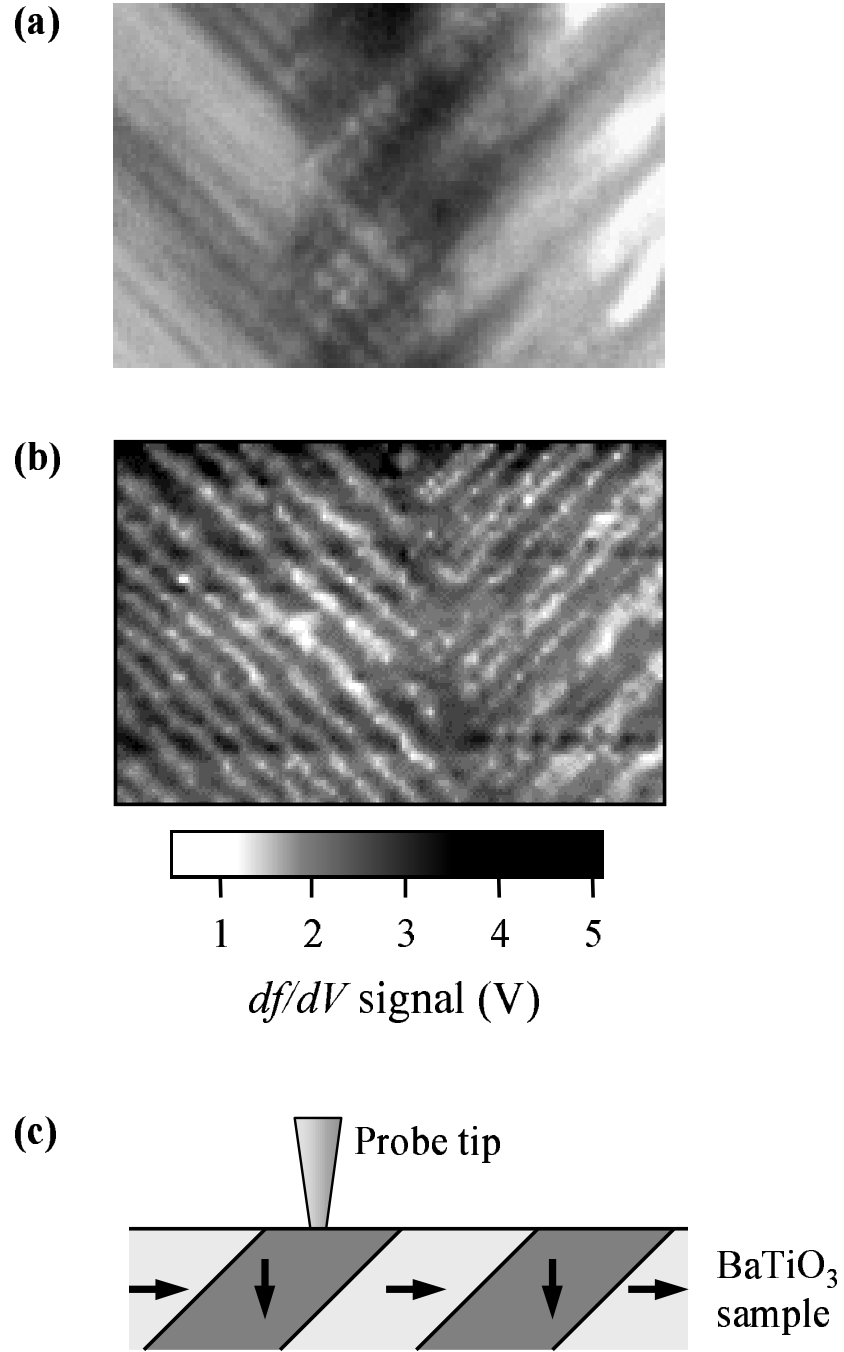


Figure 7.4: (a) Optical photograph, and (b) microwave image showing domains in a $90 \times 60 \mu\text{m}^2$ region of a BaTiO₃ crystal. The schematic in (c) shows the expected 90° domain structure expected in BaTiO₃.

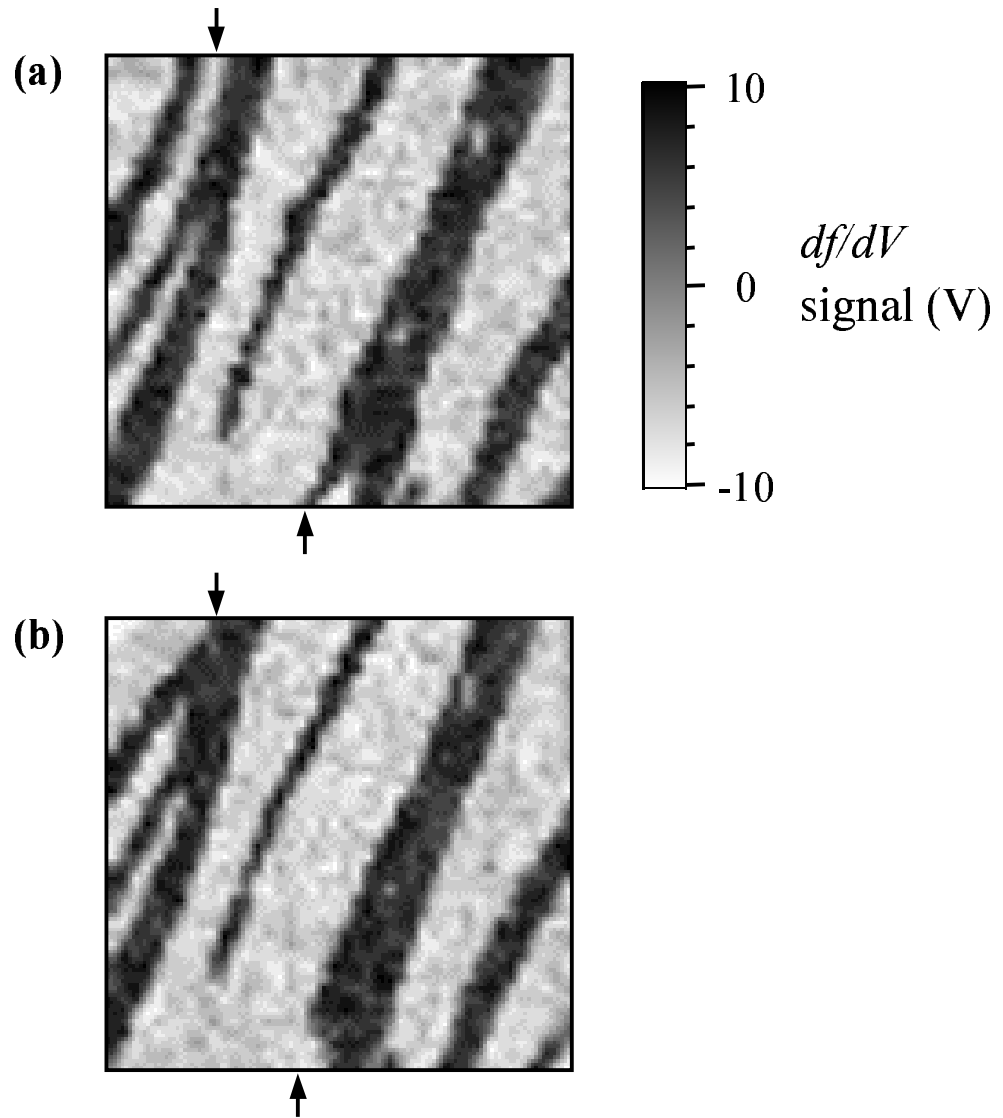


Figure 7.5: Domain images of the same $20 \times 20 \mu\text{m}^2$ region of a DTGS crystal, showing the change in domains over time. There is a time delay of about 20 minutes from (a) to (b).

is parallel to the polarization in DTGS, is normal to the surface in these images. Each image took approximately 20 minutes to acquire, and the second image was acquired immediately following the first. Even in a period of 20 minutes, the domain structure has changed slightly from (a) to (b). The two black domains indicated by the arrow at the top of (a) have joined together in (b). Also, the small black region indicated by the arrow at the bottom of (a) has disappeared in (b).

Figure 7.6 shows a larger, $100 \times 100 \mu\text{m}^2$ region of the DTGS sample. Evident in this image is the general trend for the domain boundaries to be along one direction, which is approximately the $[\bar{1} 0 2]$ direction, as observed in the literature [75, 106].

By applying a dc bias electric field to a ferroelectric crystal, it is possible to switch the polarization of a region of a sample, as shown in Fig. 7.7. The original image of a $20 \times 20 \mu\text{m}^2$ region of the DTGS sample is shown in (a). After acquiring this image, I placed the probe at the point marked by a “+” in (a), and applied a bias of +70 V to the sample. After bringing the dc bias voltage back to 0 V, I acquired the image shown in (b). The polarization in the region outlined by the dotted line has switched directions. Next, I applied a bias of –70 V to the point in (b) marked by the “+”, and then brought the bias back to 0 V. The image in (c) shows that the region outlined by the white dotted line has once again reversed polarization, to look much like the image in (a).

It is not surprising that only a small portion of the domain in Fig. 7.7(b) is switched by applying a bias voltage to the probe tip, since the bias electric field is concentrated over a tiny volume $\sim 1 \mu\text{m}^3$ near the probe tip. In fact, sometimes applying an electric field leaves the domain structure unaffected. For example,

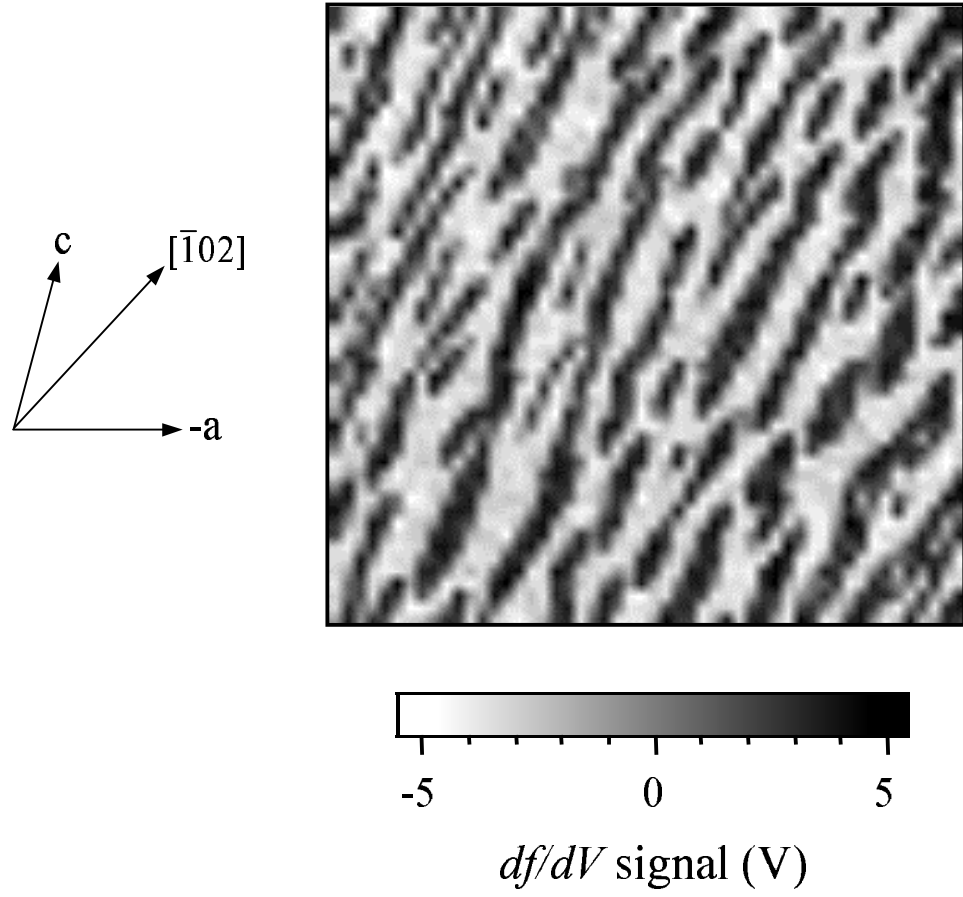


Figure 7.6: A large-area ferroelectric domain image ($100 \times 100 \mu\text{m}^2$) of the DTGS crystal, showing the preferred direction for the domain boundaries along the $[\bar{1} 0 2]$ direction.

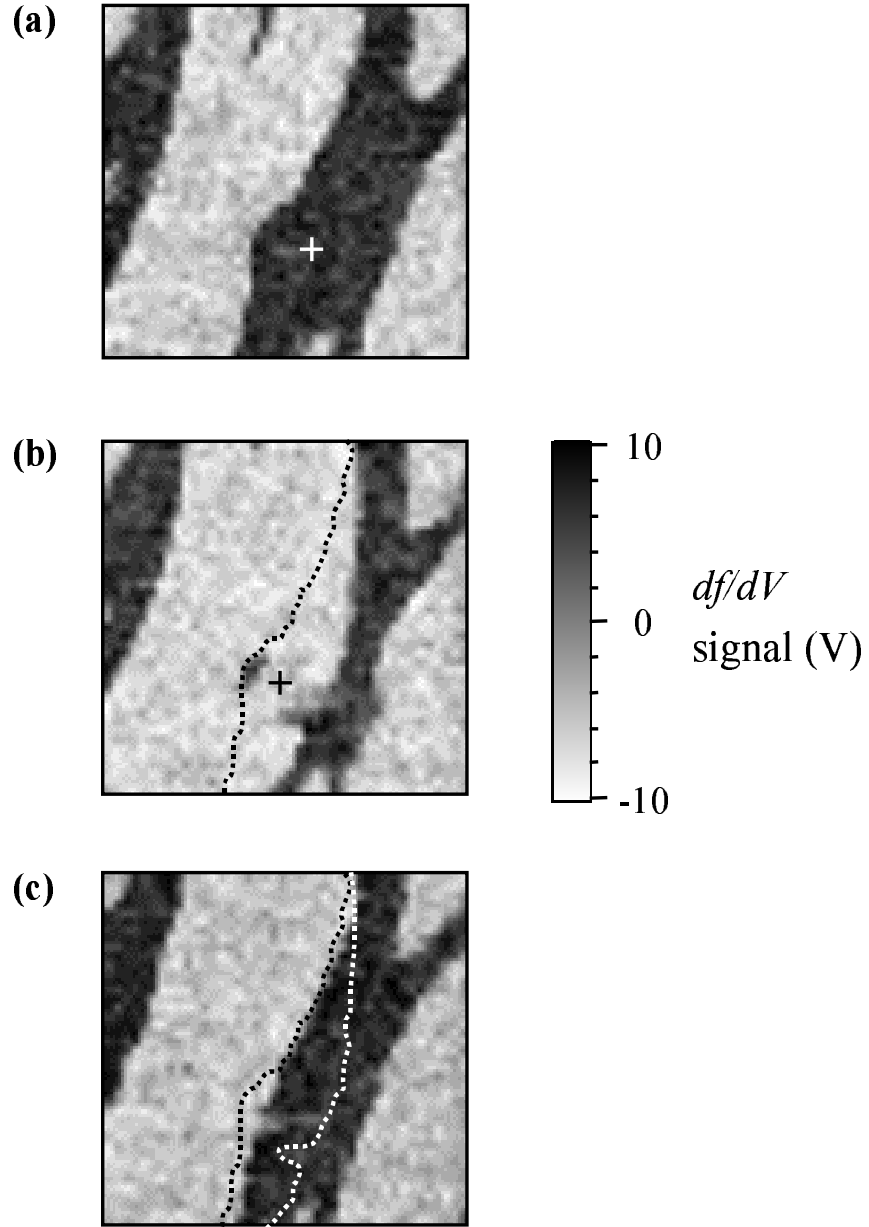


Figure 7.7: Switching a ferroelectric domain in a DTGS crystal. Images are of the same $20 \times 20 \mu\text{m}^2$ region. After acquiring (a), a positive bias was applied at the “+” sign. After acquiring (b), a negative bias was applied at the “+” sign.

when I placed the probe near the center of the white region in the middle of Fig. 7.7(c), and applied a positive bias, the resulting image was unchanged. This is probably because I was applying the electric field to an area near the center of a large domain, where switching polarization requires more energy than in a region near a domain boundary.

Chapter 8

Critical Phenomena in Deuterated Triglycine Sulfate Crystals

8.1 Introduction

Deuterated triglycine sulfate, $(\text{ND}_2\text{CD}_2\text{COOD})_3 \cdot \text{D}_2\text{SO}_4$ (DTGS), which was imaged as described in Sec. 7.3, was useful for observing critical phenomena near the ferroelectric transition. The first reason for choosing DTGS was its Curie temperature (T_c), which is at approximately 335 K, near the middle of the microwave microscope's temperature range of 300–400 K. Second, the polarization is uniaxial, along the $[010]$ axis, which is useful because the microwave microscope is sensitive to the direction of polarization only along one axis (see Sec. 7.2).

Deuterated triglycine sulfate has a second-order ferroelectric transition, of the order-disorder type [65, ?]. This distinguishes it from most oxide ferroelectrics, which have displacive transitions. Displacive ferroelectrics have a double well in the free energy below T_c , which at and above T_c turns into a single well centered at polarization $\mathbf{P} = 0$. On the other hand, in an order-disorder ferroelectric, a double well potential exists even above T_c ; above T_c , $k_B T$ (k_B is Boltzmann's

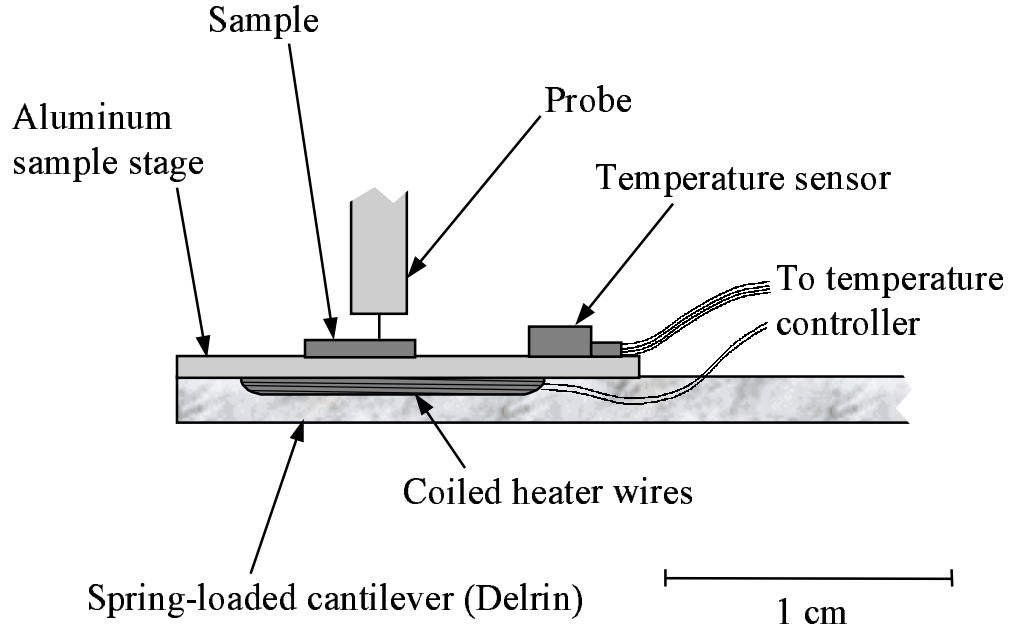


Figure 8.1: Sample holder with a heater stage. The aluminum heater stage sits atop the spring-loaded cantilever shown in Fig. 2.5. The heater wires and temperature sensor are connected to a temperature controller.

constant) exceeds the barrier between the wells, so that the polarization fluctuates with time between the two polarization states. Thus, even though the free energy has a local maximum at $\mathbf{P} = 0$, the time-averaged polarization is zero above T_c .

8.2 Changes to the Experiment

In order to heat the sample above room temperature, I built a heater stage, shown in Fig. 8.1. Heater wires are wound underneath the aluminum sample stage, and held in place with high-thermal-conductance epoxy. A silicon diode temperature sensor [62] is attached to the top of the sample holder. The heater wires and

temperature sensor are connected to a Neocera LTC-21 temperature controller [78], which regulates the temperature of the sample holder. The sample is held in place with grease on top of the aluminum sample stage; this sample stage is integrated into the spring-loaded cantilever shown in Fig. 2.5.

To make sure that changing the temperature of the sample does not change the properties of the microscope resonator itself (e.g., by causing the coaxial cable to heat up and expand, thereby changing the resonant frequency), I scanned a LaAlO_3 sample, the dielectric properties of which do not change appreciably in the range 300–400 K [124]. I chose the material LaAlO_3 , and found that the microscope resonant frequency changed by less than the noise (10 kHz) in this temperature range.

In addition, because DTGS is hygroscopic, it was necessary to minimize the humidity near the sample. A plexiglass enclosure around the microscope seals the interior environment from the room environment. By placing dessicant inside the enclosure, I was able to maintain the humidity in the range 20–35%, depending on the humidity of the air in the room. The enclosure also had the benefits of stabilizing the temperature of the microscope apparatus, and eliminating noise due to air currents in the room (see Sec. 2.1).

By applying a voltage to the probe tip using the bias tee in the microscope resonator, I was able to acquire local hysteresis loops. Instead of changing the voltage bias in discrete steps, as was done in Sec. 6.2, I varied the voltage continuously in a triangle wave at 2.02 Hz using a function generator. This technique is superior to the previous one, because it is faster, and allowed averaging of the data over many hysteresis loops (40, in this case).

Figure 8.2 shows hysteresis loops acquired at three different temperatures,

307 K, 330 K, and 350 K. At all three temperatures, the microscope resonant frequency increases with increasing electric field magnitude, indicating that the permittivity goes down when an electric field is applied; this is the expected result [54]. At 307 K, there is a large amount of hysteresis. At 330 K, just below the Curie temperature of ~ 335 K, there is very little hysteresis. At 350 K, in the paraelectric state, there is virtually no hysteresis, and the curve has flattened out at its base.

8.3 Critical Phenomena in the Permittivity of DTGS

8.3.1 Measurement Technique

To investigate critical phenomena in the permittivity of DTGS, I converted the frequency shifts from the hysteresis loops into quantitative permittivity and tunability. Since the measurement is sensitive to both horizontal and vertical components of permittivity, I had to make an assumption about the sample permittivity. At low frequency at least, the permittivity ϵ_r in the (100) and (001) directions is relatively constant in the temperature range 300–400 K at $\epsilon_r^{(100)} = 9$ and $\epsilon_r^{(001)} = 5$ [49]. Thus, with the (010) axis normal to the top face of the sample, I was able to assume the horizontal component of permittivity to be constant; I took its value to be 7. Then, using the model described in Chapter 5, taking the component of ϵ_r along the (010) direction to be the unknown quantity to be measured, I was able to measure $\epsilon_r^{(010)}$ as a function of temperature, as shown in Fig. 8.3(a). The permittivity peaks in the range 340–350 K. This is slightly above the expected

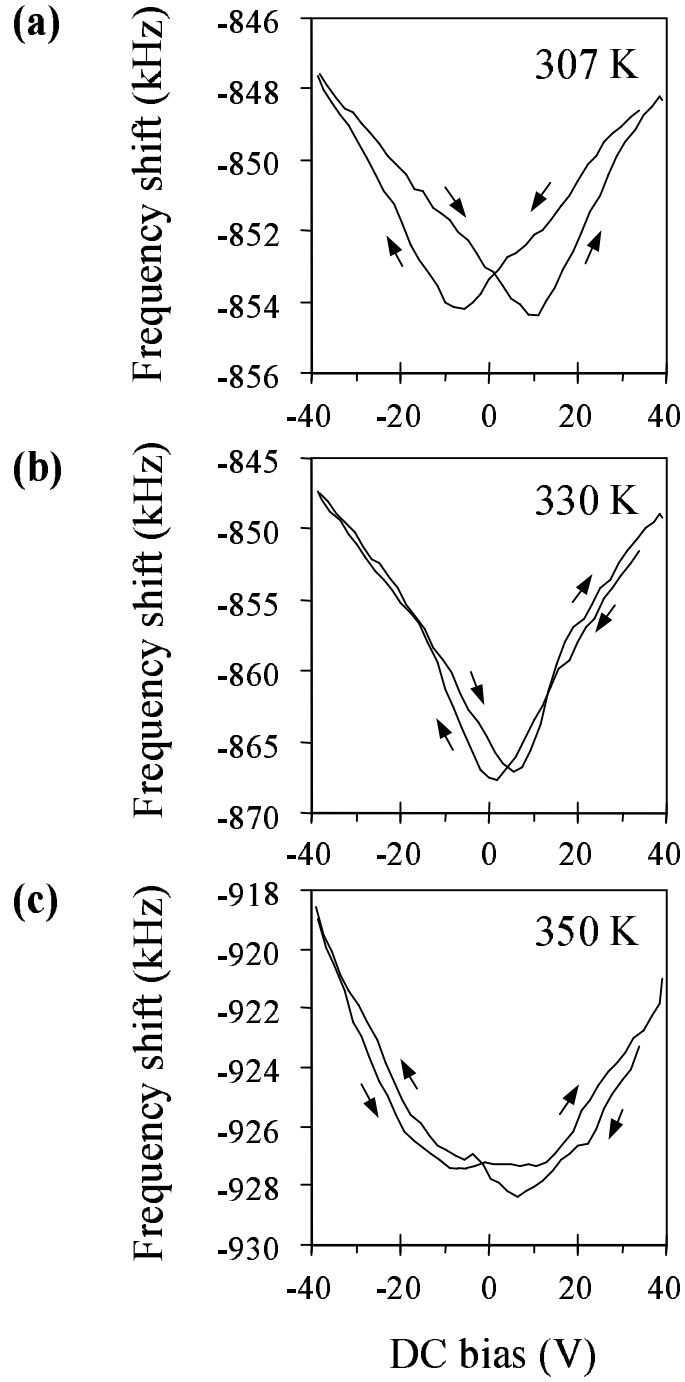


Figure 8.2: Hysteresis loops in DTGS at three different temperatures: (a) 307 K, (b) 330 K, and (c) 350 K. The Curie temperature is approximately 335 K.

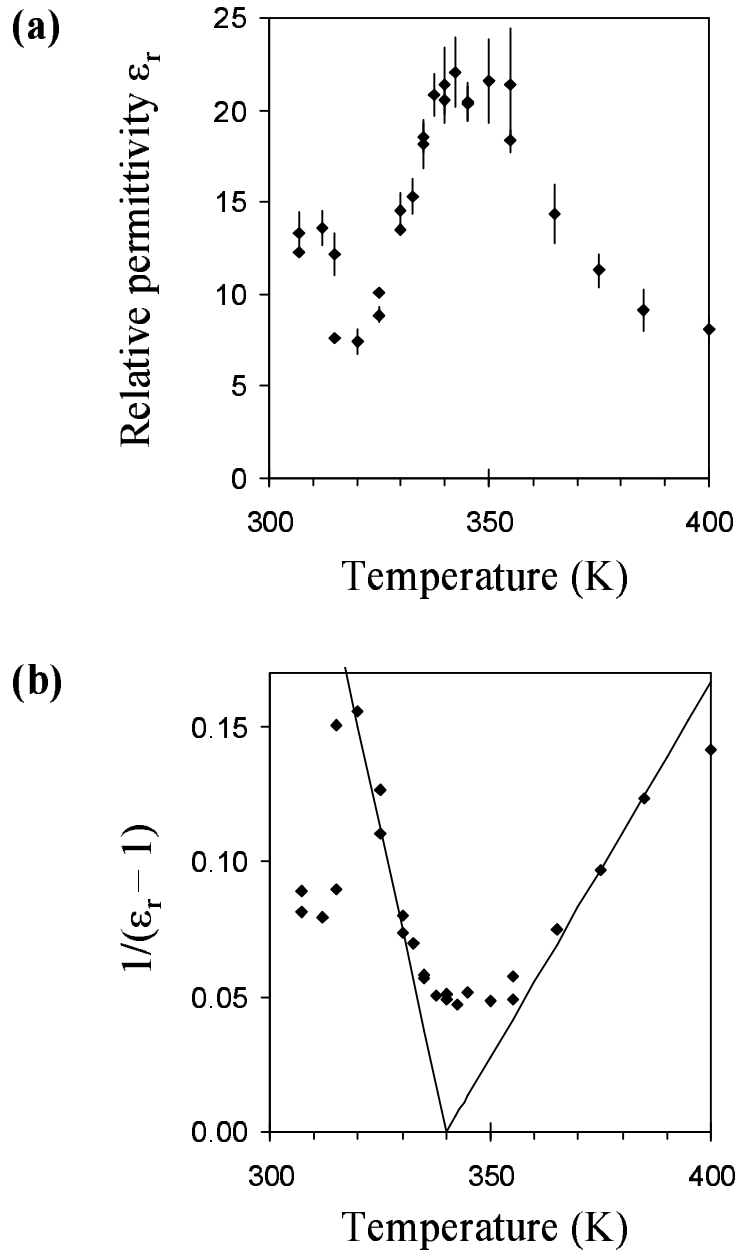


Figure 8.3: (a) Permittivity ϵ_r vs. temperature in DTGS. (b) Inverse electric susceptibility, $1/(\epsilon_r - 1)$ as a function of temperature. The two lines are fits below and above $T_c = 340$ K.

Curie temperature $T_c \sim 335$ K, probably because the top surface of the 5.5-mm-thick sample is slightly cooler than the measured temperature of the heater stage.

8.3.2 Thermodynamic Theory and Curie Constants

Before looking at the data in more detail, we will first review some of the theory of ferroelectric phase transitions. Following the phenomenological thermodynamic theory of Devonshire [30, 65], we start with the elastic Gibbs energy F (usually just called the free energy)

$$F = U - TS - X_i x_i \quad (8.1)$$

where U is internal energy, T is temperature, S is entropy, X_i is stress, and x_i is strain, and the subscript $i = 1, 2, 3$ indicates a summation over all three axes. (We use CGS units in this section, for simplicity.) Using the thermodynamic relation

$$dU = TdS + X_i dx_i + E_i dP_i, \quad (8.2)$$

we find

$$dF = -SdT - x_i dX_i + E_i dP_i. \quad (8.3)$$

Although most authors, including Devonshire [30], use the polarization \mathbf{P} as a variable, as in Eq. 8.3, the electric displacement \mathbf{D} could be used instead, with the same conclusions (Eqs. 8.10–8.14), as was done by Lines and Glass [65]. Next, we assume that all measurements will be done at constant temperature and stress, so that $dT = 0$ and $dX = 0$. We expand the free energy about $\mathbf{P} = 0$:

$$F(P, T, X) = F(0, T, X) + \left. \frac{\partial F}{\partial P_i} \right|_{T, X} P_i$$

$$+ \frac{1}{2!} \left. \frac{\partial^2 F}{\partial P_i \partial P_j} \right|_{T,X} P_i P_j + \frac{1}{3!} \left. \frac{\partial^3 F}{\partial P_i \partial P_j \partial P_k} \right|_{T,X} P_i P_j P_k + \dots \quad (8.4)$$

Next, we assume \mathbf{E} and \mathbf{P} to be along a crystallographic axis [the (010) axis for DTGS], allowing us to take only one component of i , j , and k in Eq. 8.4. Finally, we assume that the non-polar (paraelectric) state is centrosymmetric, so that the free energy is not dependent on the sign of the polarization, allowing us to keep only even powers of the polarization in the free energy expansion. Thus, to sixth order, we have the equation

$$F = \frac{\alpha}{2} P^2 + \frac{\gamma}{4} P^4 + \frac{\delta}{6} P^6 + F(T, X) \quad (8.5)$$

where α , γ , and δ are material-dependent parameters. From Eqs. 8.3 and 8.5, the electric field E is

$$E = \frac{\partial F}{\partial P} = \alpha P + \gamma P^3 + \delta P^5. \quad (8.6)$$

We assume γ and δ to be temperature-independent; thus, all temperature dependence is through the parameter α . For a second-order transition (such as with DTGS), $\gamma > 0$, so that a double well exists below T_c and a single well above T_c . For first-order transitions, $\gamma < 0$, giving a triple-well and metastable states near- T_c . Also, the δ term is not required for second-order transitions, so we will take $\delta = 0$.

When $\alpha < 0$, the free energy F has two minima, characteristic of the ferroelectric state. On the other hand, when $\alpha > 0$ the free energy has one minimum, at $P = 0$, as in the paraelectric state. At the Curie temperature T_c , $\alpha = 0$. (We note that as an order-disorder ferroelectric, this description isn't exactly true for DTGS: even above T_c , there are two minima in the free energy. However, since $k_B T$ is greater than the barrier between the wells at $P = 0$, in a time-averaged sense the crystal behaves as if there was a single minimum in the free energy at

$P = 0$. In fact, despite this discrepancy in the model, TGS and DTGS are well known to have a characteristic second-order transition with close agreement with thermodynamic theory [54].)

For the temperature dependence, the simplest possible case is α varying linearly with temperature near T_c :

$$\alpha = \beta(T - T_c). \quad (8.7)$$

We compute the relative permittivity from Eq. 8.9

$$\frac{1}{\epsilon_r(P) - 1} = \frac{\partial E}{\partial P} = \alpha + 3\gamma P^2. \quad (8.8)$$

The zero-field relative permittivity, ϵ_r^0 , is then

$$\frac{1}{\epsilon_r^0 - 1} = \left. \frac{\partial E}{\partial P} \right|_{E=0} = \alpha + 3\gamma P_s^2, \quad (8.9)$$

where P_s is the spontaneous polarization. Above T_c , $P_s = 0$, so that

$$\epsilon_r^0 - 1 = \frac{1}{\alpha} = \frac{1}{\beta(T - T_c)}, \quad T > T_c \quad (8.10)$$

This equation is in fact the Curie-Weiss law [54],

$$\epsilon_r^0 - 1 = \frac{C_{>}}{T - T_0}, \quad T > T_c, \quad (8.11)$$

when we take $\beta \equiv 1/C_{>}$, and $T_0 \equiv T_c$, which is the case for second-order transitions. The parameter $C_{>}$ is the Curie constant for $T > T_c$.

The Curie constant $C_{>}$ can be found from my data by plotting $1/(\epsilon_r - 1)$ as a function of temperature, as shown in Fig. 8.3(b). The straight lines are fits above and below T_c . The lines cross the horizontal axis at 340 K, which I take to be the temperature measured by the temperature sensor when the sample is at T_c . Because the sample is thick (5.5 mm), the top surface is expected to be at a lower

temperature than that measured by the sensor, explaining why the measured T_c (340 K) is greater than the expected T_c of 335 K. From the slope of the linear fit for $T > T_c$, I find the Curie constant $C_> = 360$ K. Previously reported values for $C_>$ in DTGS are in the range 1900–3000 K [87, 88], 5 to 8 times larger than my measured value. This disagreement could be due to my high measurement frequency, which has the effect of dielectric critical slowing down (see below), which flattens out the curve in Fig. 8.3(b) near T_c , requiring me to obtain the linear fits over a larger temperature range on either side of T_c .

From Eq. 8.6, we find the spontaneous polarization to be

$$P_s = P|_{E=0} = -\frac{\beta(T - T_c)}{\gamma}. \quad (8.12)$$

Substituting Eq. 8.12 into Eq. 8.9, we get

$$\epsilon_r - 1 = \frac{-2}{\beta(T - T_c)}, \quad T < T_c. \quad (8.13)$$

Thus, the Curie constant below T_c is twice that above T_c :

$$\frac{C_<}{C_>} = -2 \quad (8.14)$$

For many materials, such as BaTiO_3 , Eq. 8.14 is accurate. However, in DTGS, it is not. Due to the larger thermoelectric effect in DTGS (the thermoelectric coefficient for TGS [44] is approximately five orders of magnitude higher than for BaTiO_3 [45]), applying an electric field changes the temperature of the DTGS sample. Thus, applying a high-frequency electric field causes the sample temperature to oscillate at the same frequency, making the constant-temperature assumption invalid. Instead of the measurement being isothermal, it is adiabatic, requiring an additional term in Eq. 8.14 [88, 107]:

$$\frac{C_<}{C_>} = -2 \left(1 + \frac{\beta T}{2\gamma c_p} \right) \approx -2.4 \quad (8.15)$$

where c_p is the heat capacity per unit volume at constant polarization.

From the linear fits in Fig. 8.3, I find the ratio of slopes to be -2.7 , in close agreement with the theoretical value of -2.4 , and well within the range of values published previously, -2.3 to -4.2 , based on measurements of $\epsilon_r(T)$ for frequencies below 50 kHz [88].

8.3.3 Critical Slowing Down of Dielectric Response

The data in Fig. 8.3(a) flattens out near T_c , reaching a maximum of only $\epsilon_r \approx 22$. This differs significantly from low-frequency data in the kHz range, which shows a peak in $\epsilon_r(T)$ several orders of magnitude higher, in the range 10^3 – 10^5 (see Fig. 8.4) [49, 88, 107]. I attribute this difference to dielectric critical slowing down, which occurs when the measurement period (the inverse of the measurement frequency) is shorter than the relaxation time of the polarizing distortion of the crystal lattice, and the rf electric field cannot fully polarize the lattice because the ions move too slowly to keep up with the driving field. As a result, the measured susceptibility at high frequency is suppressed, as shown in Fig. 8.4. Also seen in this figure is a minimum in $\epsilon_r(T)$ at T_c at high frequencies [48, 90, 101], which can be understood using the following highly-simplified illustration. The crystal can be represented as ions with mass M in potential wells, with the ions being held in their equilibrium position with a spring constant k , which is inversely related to their polarizability (and thus to the susceptibility of the crystal [58]). The natural frequency of the lattice is then $f = \sqrt{k/M}$. Near T_c , the spring constant k has a minimum, shown by the peak in the electric susceptibility at T_c at low frequency. However, this minimum in k at T_c also acts to decrease the natural frequency f of the lattice, resulting in enhanced slowing down of the dielectric

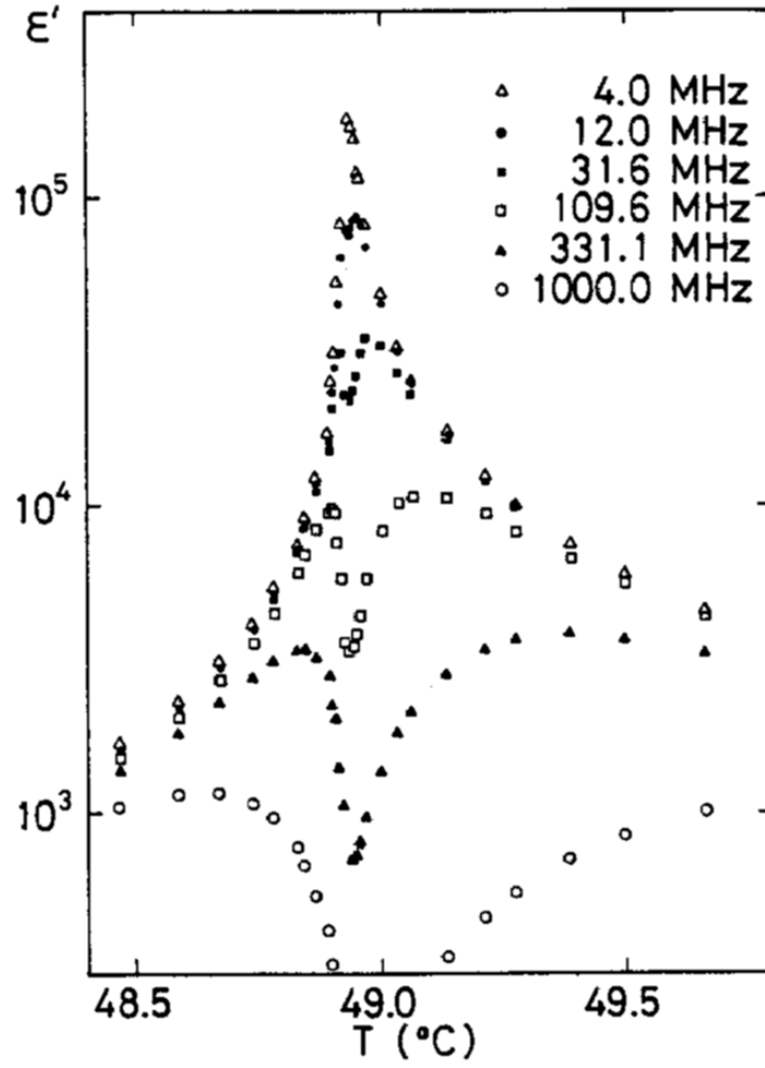


Figure 8.4: Critical slowing down of the dielectric response (ϵ') as a function of temperature and frequency in triglycine sulfate (TGS), which has a T_c of 49°C . From Ref. [101].

response and the minimum in ϵ_r seen in Fig. 8.4 at T_c at high frequency. Thus, the minimum in k near T_c has two effects that almost seem contradictory: the peak in $\epsilon_r(T)$ at T_c at low frequency, as well as the minimum in ϵ_r at T_c at high frequency. I made measurements of $\epsilon_r(T)$ at multiple frequencies in the range 6–12 GHz; the results were inconclusive, but did show some possible evidence of an increased dielectric slowing-down effect with increasing frequency.

8.4 Dielectric Nonlinearity

In addition to the linear permittivity, ferroelectric critical phenomena can also be investigated by looking at dielectric nonlinearity as a function of temperature. Using hysteresis loops like those shown in Fig. 8.2, I can measure the dielectric nonlinearity by defining $\Delta\epsilon_r$ as the change in permittivity upon application of 40 V to the sample. Shown in Fig. 8.5(a) is $\Delta\epsilon_r$ as a function of temperature. Unlike the permittivity (Fig. 8.3), the nonlinearity has a sharp peak, at 340 K. This value for T_c agrees with the linear fits shown in Fig. 8.3(b). Thus, I conclude that the ferroelectric transition in the DTGS sample occurs when the temperature sensor reads 340 K, which probably is higher than the actual temperature of the top surface of the sample, as explained above.

The tunability, which I define as $\Delta\epsilon_r/\epsilon_r$, is shown in Fig. 8.5(b) as a function of temperature; it also has a peak at about 340 K. My measured tunability is expected to differ from measurements that involve uniform fields, such as with a parallel-plate capacitor, since the electric field in my case is nonuniform, and concentrated in a tiny volume of the sample. For example, Triebwasser [107] measured a tunability greater than 50% for an electric field of 6 kV/cm. On the other hand, I measure a tunability of 10%, with an average field in a volume of

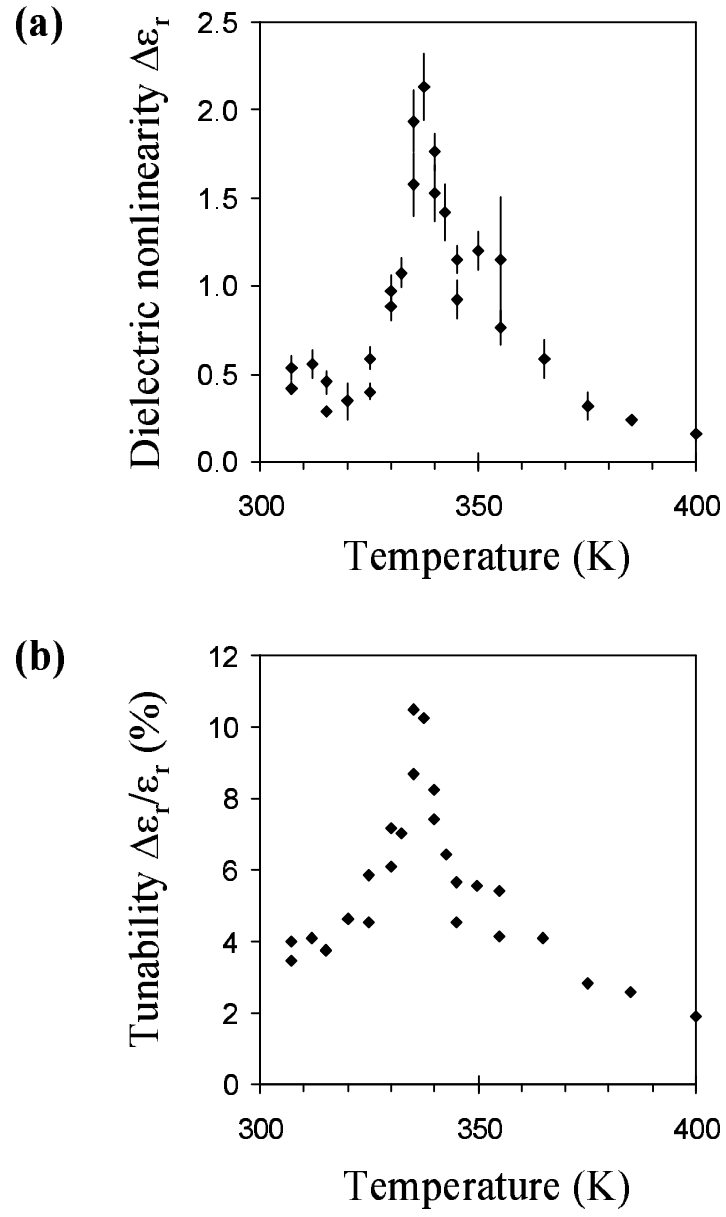


Figure 8.5: (a) Dielectric nonlinearity ($\Delta\epsilon_r$) vs. temperature. (b) Tunability ($\Delta\epsilon_r/\epsilon_r$) vs. temperature.

1 μm^3 beneath the probe tip of 140 kV/cm. I believe that this large difference is due to my measurement averaging over a larger volume than 1 μm^3 . Also, my bias electric field has a component in the horizontal direction, which is not expected to contribute to the measured tunability.

To investigate dielectric nonlinearity in DTGS above T_c in a more quantitative way, we follow the method of Cach, *et al.* [21]. Combining Eqs. 8.6 and 8.8, eliminating P , we obtain

$$\xi(E) \equiv \chi_E^3(E) + 3\alpha\chi_E^2(E) - 4\alpha^3 = 27\gamma E^2, \quad (8.16)$$

where $\chi_E = 1/(\epsilon_r - 1)$ is the electric susceptibility, and α is the zero-field electric susceptibility. The graph of the function $\xi(E)$ vs. E^2 should be a straight line, the slope of which is proportional to the parameter γ in the free energy expansion. These results are shown in Fig. 8.6 for temperatures from 340 K to 365 K. As expected, the data appear to be along straight lines, with a slope which is somewhat independent of temperature. From the slopes of the linear fits, I calculate the parameter $\gamma = (1.6 \pm 0.3) \times 10^{13} \text{ Vm}^5\text{C}^{-3}$. This differs from Cach's low-frequency (1.6 kHz) result for TGS, $\gamma \approx 6 \times 10^{11} \text{ Vm}^5\text{C}^{-3}$ [21] by about a factor of 25. This sizeable discrepancy is probably mainly due to the suppressed ϵ_r at high frequency which is the result of dielectric critical slowing down (Sec. 8.3.3).

8.5 Ferroelectric Domain Structure Relaxation Time

A third way to investigate ferroelectric critical phenomena is through domain formation. When a ferroelectric crystal is cooled from above T_c to below T_c ,

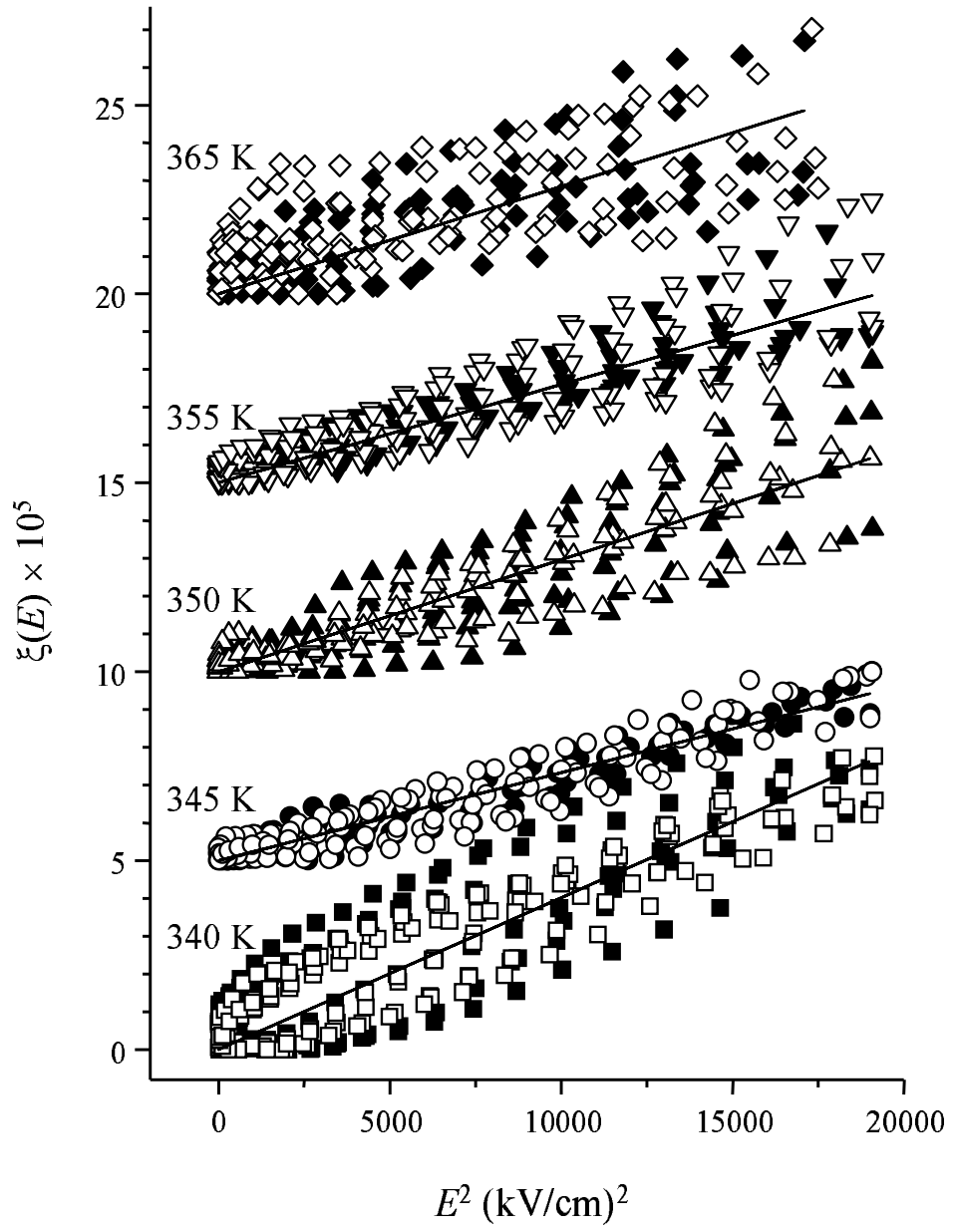


Figure 8.6: The function ξ as a function of the square of the electric field. The data for each temperature have been offset vertically for clarity. Solid symbols are for increasing electric field, while open symbols are for decreasing electric field.

it takes a finite time for domains to nucleate and stabilize in the lowest-energy configuration.

To quantitatively measure ferroelectric domain relaxation times, I used the following procedure. First, I heated the sample, a 0.5 mm thick DTGS crystal, to 360 K and left it there for 20 minutes. Then I cooled it to the measurement temperature and began repeatedly imaging a $40 \times 40 \mu\text{m}$ region of the sample. Each image took 25–35 minutes to complete, so data points are approximately 30 minutes apart. After acquiring the images, I plotted a histogram of the df/dV data for each image. Example images and histograms, acquired by Sangjin Hyun, are shown in Fig. 8.7. In (a), the sample was above T_c (at 380 K for this image). No domains are present, and $df/dV \approx 0$. The histogram to the right of image (a) shows that the df/dV data are centered at about 0 V. Image (b) was acquired immediately after the sample reached 330 K. Many long, narrow domains are visible. The histogram shows a wide peak, which doesn't yet appear to have separated into two peaks representing the two directions of polarization. In (c), taken 30 minutes later, some of the domains have joined together. Finally, in (d), acquired 210 minutes after (b), the narrow domains seen in (b) have joined together to form a small number of wider domains. The histogram to the right of (d) shows two distinct peaks, representing the two directions of polarization.

Some other example images are shown in Fig. 8.8, with the sample at 320 K. These images show the same $100 \times 100 \mu\text{m}$ region at different times following the cooling of the sample from 360 K to 320 K. Unlike Fig. 8.7, it appears that most of the imaged region eventually formed into one large domain, with polarization down ($df/dV < 0$).

To compare ferroelectric domain relaxation times in DTGS as a function of

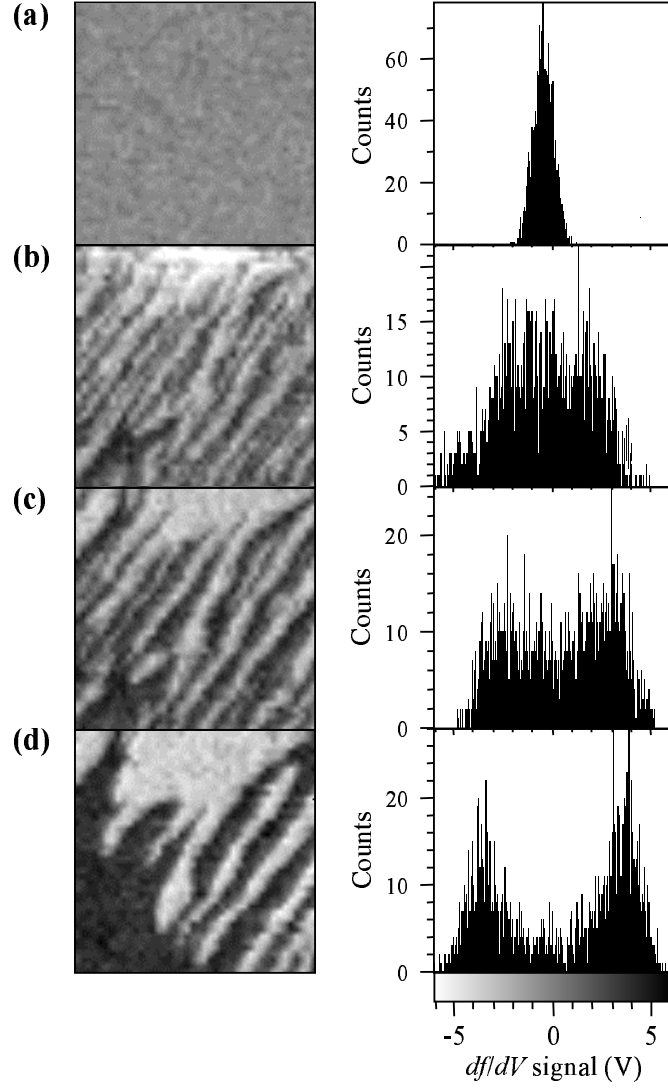


Figure 8.7: Domain formation in DTGS at 330 K. Images are of the same $40 \times 40 \mu\text{m}$ region of the sample. (a) Image acquired with the sample at 380 K. The other three images were acquired (b) 0 minutes, (c) 30 minutes, and (d) 210 minutes after the sample was cooled to 330 K. The histograms to the right of the images show the gradual transition from a single peak centered at $dI/dV = 0 \text{ V}$, to two separate peaks representing the two directions of polarization. The colorbar scale for the images is shown beneath the histograms.

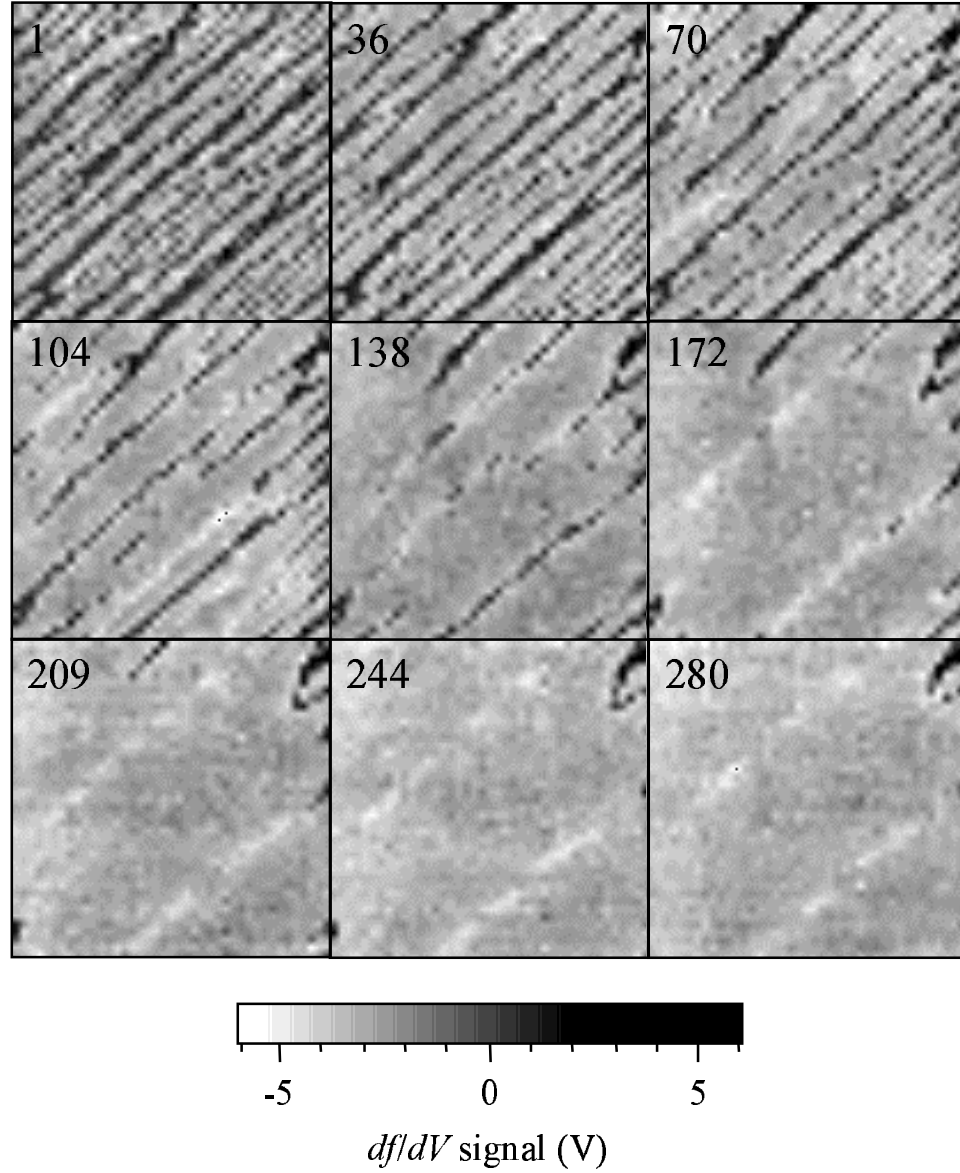


Figure 8.8: Domain formation in DTGS at 320 K. The images are of the same $100 \times 100 \mu\text{m}$ region of the sample, at different times following cooling to 320 K. The elapsed time in minutes is shown in the upper-left corner of each image.

temperature, I fitted the histogram data for each image to a function containing the summation of two Gaussian curves:

$$C(x) = A_1 e^{(x-x_1)^2/(2W_1^2)} + A_2 e^{(x-x_2)^2/(2W_2^2)} \quad (8.17)$$

where A_1 , A_2 , x_1 , x_2 , W_1 , and W_2 are fitting parameters, $C(x)$ is the number of counts in each bin, and x is the df/dV signal. Then, I plotted the amplitude A_1 of the largest peak ($A_1 > A_2$) for each image as a function of time, as shown in Fig. 8.9(a). I fit this function to a decaying exponential,

$$A_1(t) = A_0 - b e^{-t/t_0} \quad (8.18)$$

where A_0 , b , and t_0 are fitting parameters. I took $t_0(T)$ to be the ferroelectric domain relaxation time of the crystal at temperature T .

Figure 8.9(b) shows t_0 as a function of temperature. The domain relaxation time appears to have a minimum near $T_c \approx 335$ K. This behavior can be explained using the thermodynamic model presented in Sec. 8.3.2. The barrier between polarization states in the free energy decreases as T_c is approached from below, reaching zero at T_c . As the height of this barrier decreases, less energy is required to switch the polarization of a unit cell. Consequently, the crystal's domain structure more easily and quickly relaxes to its lowest-energy state near T_c , resulting in the shorter domain relaxation times near T_c seen in Fig. 8.9(b).

This ferroelectric domain relaxation time is quite different from the lattice relaxation time discussed in Sec. 8.3.3. First, we notice that the lattice relaxation time reaches a maximum at T_c , rather than the minimum seen in the domain relaxation time. Second, the time scales between the two effects are vastly different: the lattice relaxation time for DTGS is on the order of 10^{-9} s, while the domain relaxation time is on the order of 10^4 s. These differences are due to the

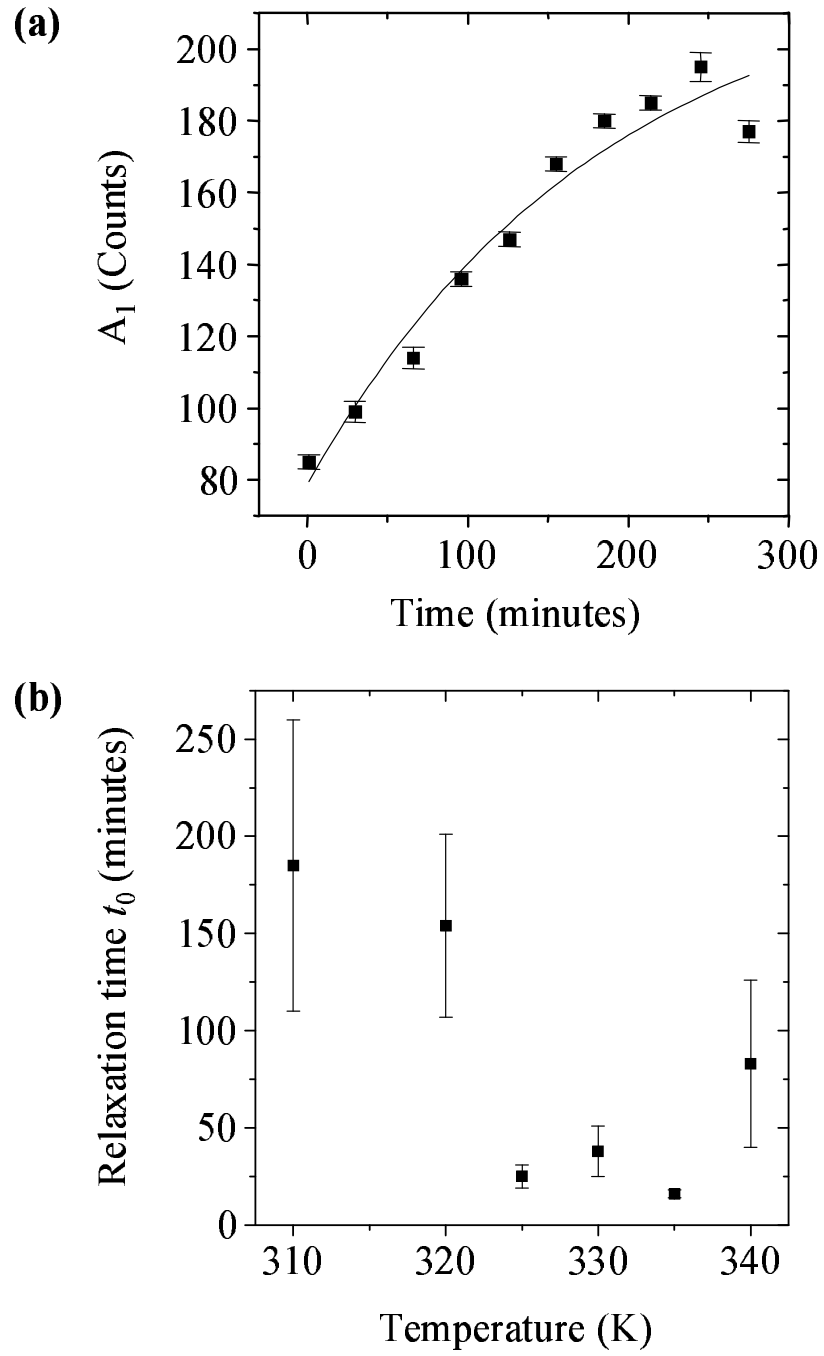


Figure 8.9: (a) Histogram amplitude A_1 vs. time for DTGS at 310 K. (b) Ferroelectric domain relaxation time for DTGS as a function of temperature.

different physical mechanisms causing the two effects. The lattice relaxation time is the inverse of the natural frequency of the lattice, which reaches a minimum at T_c . On the other hand, the ferroelectric domain relaxation time, as explained above, is due to the energy barrier between polarization states going to zero at T_c .

Another consequence of this energy barrier going to zero at T_c is critical fluctuations, which reach a maximum at T_c . The classic example of critical fluctuations is critical opalescence in fluids, which occurs when the latent heat between the liquid and gas phases goes to zero at the critical point [91].

Chapter 9

Summary and Future Work

9.1 Summary

Our near-field scanning microwave microscope is a versatile instrument, which still has many unexplored capabilities. It is unique in several ways even among near-field microwave techniques (see Table 1.1). For example, the spatial resolution is readily adjustable over the range from 1–500 μm simply by changing probes. This is advantageous because different spatial resolutions are desired for different types of measurements. For example, for homogeneity measurements on large wafers, low-resolution measurements are preferable. On the other hand, high resolution imaging is required for imaging defects in thin films.

Another distinguishing feature is the broadband capability of the microscope. To date, we have only begun to exploit this capability, making measurements in the range from 6 to 12 GHz. Without major changes, this range could be extended to include 0.1 to 18 GHz. By using higher-frequency microwave connectors, the range could be extended up to 50 GHz, or even higher. By lengthening the resonator beyond 2 m, the lower frequency limit could also be extended. In addition, by including a commercially-available phase shifter in the resonator, the

resonant frequency could be varied continuously over the frequency bandwidth of the instrument.

The technique for quantitative measurement of permittivity presented in Chapter 5 allows imaging in less than an hour. This distinguishes it from microwave measurements of permittivity by other groups [39, 40, 116], which require measurements at multiple heights. While our technique is less accurate, the ability to acquire spatially-resolved images is a distinct advantage; to our knowledge, our images of quantitative permittivity [94] shown in Fig. 5.12 are the only such images published to date. In addition, we can quantitatively measure dielectric tunability, simultaneous with linear permittivity measurements.

9.2 Future Work

There are several aspects of the microwave microscope that have not yet been investigated, and improvements that could be made to the instrument in the future.

9.2.1 Improvements to the Scanning System

One improvement that could be made to the instrument is the scanning motors. The stepper motors which we use now, while having advantages of high speed (25 mm/s) and high resolution ($0.1\ \mu\text{m}$), vibrate even when the motors are stationary. The amplitude of vibration also depends on the position of the scanning stage. This vibration does not pose a problem for non-contact imaging with a probe-sample separation of tens of microns; however, contact-mode imaging is extremely sensitive to vibration. The first step to solve the vibration problem would be to

use motors which vibrate less. Even better, one could include a piezoelectric scanner on top of low-vibration motor translation stages, to be used for high-resolution imaging.

9.2.2 Making Dielectric Loss Measurements

Another improvement would be to increase the Q of the microscope, an optimization that we have not yet pursued in depth. A higher Q is necessary for quantitative dielectric loss measurements, so that losses in the resonator do not dominate the measurement.

Radiated power, for example, is a serious problem because it decreases the Q , is sample-dependent, and cannot be easily modeled. I have measured radiation from the microscope probe tip with a horn antenna connected to a power meter, and have found the radiated power to be not only a function of the probe geometry (such as the length of the protruding STM tip), but also a function of the permittivity of the sample with which the probe is in contact. In other words, the permittivity of the sample affects the antenna properties of the probe tip. This sample-dependent radiation loss is undesirable, because this radiation loss could be incorrectly attributed to dielectric loss. This effect is evident in images of dielectric thin films, where we have found that Q images always closely resemble Δf images. This probably is due to the Q of the microscope being mainly dependent on the sample's permittivity, rather than its dielectric loss, due to permittivity-dependent radiation.

The desired solution to this sample-dependent radiation problem is simply to minimize radiation from the probe tip. One way to accomplish this is by shortening the length of the protruding STM tip. I found experimentally that the

radiated power from the probe is proportional to the square of the distance that the center conductor extends beyond the outer conductor. Another way to minimize radiation is by decreasing the area between the inner and outer conductors in the probe. According to theory [20], the radiated power is proportional to the square of this area. A third way to reduce radiation is to go to lower frequency, since radiated power is proportional to ω^4 . A fourth way to reduce radiation would be to enclose the probe and sample inside a small metallic cavity which is too small for any internal resonances to occur at the measurement frequency; this would effectively eliminate any far-field radiation from the probe tip, but might be difficult to use.

To investigate further, the reduction in Q due to dielectric loss can be calculated using a formula similar to Eq. 5.18 [5]:

$$\begin{aligned}\Delta\left(\frac{1}{Q_L}\right) &= \Delta\left(\frac{1}{Q_{L2}} - \frac{1}{Q_{L1}}\right) \approx \frac{\epsilon_0}{2W} \int_{V_S} (\epsilon''_{r2} - \epsilon''_{r1}) \mathbf{E}_1 \cdot \mathbf{E}_2 dV \\ &= \frac{-2(\epsilon''_{r2} - \epsilon''_{r1})}{\epsilon'_{r2} - \epsilon'_{r1}} \frac{\Delta f}{f}\end{aligned}\tag{9.1}$$

where Q_{L1} and Q_{L2} are the loaded quality factors, and ϵ''_{r1} and ϵ''_{r2} are the imaginary parts of the dielectric constants, of the unperturbed and perturbed systems, respectively. As an example, we calculate the expected $\Delta(1/Q_L)$ upon going from a 0.5 mm thick LaAlO₃ sample ($\epsilon'_r = 24$, $\epsilon''_r = 7.4 \times 10^{-4}$ [60]) to a 0.5 mm thick SrTiO₃ sample ($\epsilon'_r = 305$, $\epsilon''_r = 9.2 \times 10^{-2}$). Using Eq. 9.1, with our measured $\Delta f = 670$ kHz and $f = 7.5$ GHz, we calculate $\Delta(1/Q_L) = 6 \times 10^{-8}$. Using $Q_{L1} = 114.1$, this gives $\Delta Q_L = 8 \times 10^{-4}$.

Experimentally, we measure $Q_{L1} = 114.1$, and $Q_{L2} = 113.6$, giving $\Delta Q_L = 0.5$, or $\Delta(1/Q_L) = 4 \times 10^{-5}$. This measured change in Q_L is three orders of magnitude larger than the calculated value from dielectric losses. We attribute

this discrepancy to the enhanced radiation loss when the probe is in contact with the SrTiO_3 sample. A way to remove this discrepancy would be to minimize radiation from the probe tip, so that the radiated power is smaller than energy loss in the sample.

9.2.3 Further Investigation of Dielectric Measurements

As pointed out by Wang, Reeves and Rachford [116], quantitative permittivity measurements average over a larger volume of the sample than $1 \mu\text{m}^3$. Consider a case where a $1 \mu\text{m}^3$ defect in a sample has a permittivity of ϵ_r^A , while the surrounding volume has permittivity $\epsilon_r^B > \epsilon_r^A$. Due to averaging over a larger volume than $1 \mu\text{m}^3$, the measured frequency shift will be larger when the probe is in contact with the low-permittivity defect than it would be for a uniform sample with permittivity ϵ_r^A . As a result, the permittivity of the defect will be overestimated.

The best solution to this problem would be to improve the spatial resolution of the microscope, so that the averaging takes place over a smaller volume. However, due to the nature of the measurement, this averaging effect cannot be completely eliminated.

9.2.4 Improving the Spatial Resolution

Many interesting material features require higher spatial resolution than $1 \mu\text{m}$. For example, ferroelectric domains are less than $1 \mu\text{m}$ across in thin films [38]. Ferroelectric domain boundaries are around 0.5–20 nm in width [65]. Superconductors, another potential research application of the microwave microscope, have grains which have sizes on the order of the film thickness, often less than 100

nm. Vortices in high- T_c superconductors have a size determined by the penetration depth, typically around 150 nm. Imaging any of these small features require higher spatial resolution than we can currently achieve with the microwave microscope.

The obvious way to improve the spatial resolution is to decrease the radius of the probe tip. However, this is not a trivial task. When the probe tip is placed in contact with the sample, the sharp tip will always be damaged. A solution might be to scan the sample out of contact. We have tried this with a microwave microscope combined with a scanning tunneling microscope (STM), with the probe tip 1–10 nm from a conducting sample. However, our results appear to show that this microwave measurement is more sensitive to topography than sheet resistance on length scales less than 1 μm . This is probably due to the radius of the probe tip still being on the order of 0.5 μm . One way to maximize the sharpness of the probe tip could be to attach a long, narrow carbon nanotube to the STM tip.

Another approach would be to adopt a geometry used by van der Weide [108], who uses an atomic force microscope (AFM) scanning tip which has been modified to have an extremely sharp coaxial microwave tip. He uses this microwave probe to pick up electromagnetic signals from operating electronics, with a spatial resolution of 10 nm. This same type of tip could be adapted for use with a near-field scanning microwave microscope resembling our system.

9.3 Conclusion

Much progress has been made with our near-field scanning microwave microscope. However, like any experiment, there are always improvements that can be made,

and new capabilities to be investigated. In less than five years since this project was first conceived, we have had success investigating many types of materials, including conducting thin films, superconductors in the normal state, dielectric materials, ferroelectric and paraelectric materials, and magnetic materials. We have high hopes that this instrument will offer much to the realms of physics and materials science, academia and industry, in the years to come.

Appendix A

Input Impedance to a Conducting Thin Film

Sample

The impedance seen by the probe looking into a conducting thin film on an infinite dielectric substrate can be calculated using cascaded impedances [27]. As shown in Fig. A.1, the probe sees the cascaded impedances of the conducting thin film (Z_S), and the dielectric substrate (Z_d). The equation for the impedance looking into the sample is

$$Z_{in} = Z_S \frac{Z_d + iZ_S \tan \beta d}{Z_S + iZ_d \tan \beta d} \quad (\text{A.1})$$

where d is the thickness of the film, and β is the propagation constant in the thin film:

$$\beta = \frac{\omega \mu_0}{Z_S}. \quad (\text{A.2})$$

The impedance in the thin film in the local limit (Z_S) and the impedance in the dielectric substrate (Z_d) are [59]

$$Z_S = R_S + iX_S = \sqrt{\frac{\omega \mu_0 \rho}{2}}(1 + i) = R_S(1 + i) \quad (\text{A.3})$$

$$Z_d = \frac{Z_0}{\sqrt{\epsilon_r}}(1 + \frac{i}{2} \tan \delta) \approx \frac{Z_0}{\sqrt{\epsilon_r}}, \quad (\text{A.4})$$

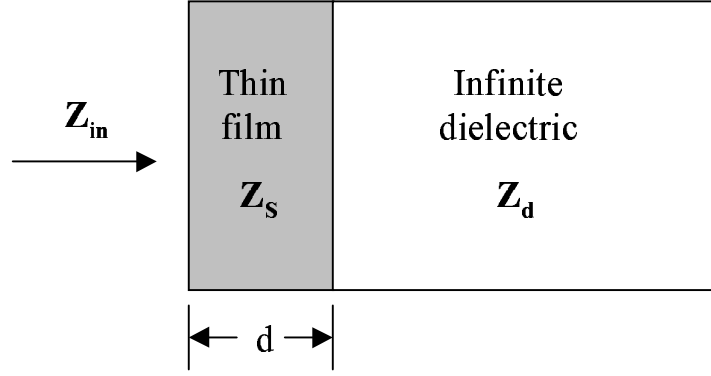


Figure A.1: The input impedance Z_{in} looking into a conducting thin film on an infinite dielectric.

where ω is the frequency, μ_0 is the permeability of free space, ρ is the resistivity, Z_0 is the impedance of free space ($377 \, \Omega$ in MKS units), ϵ_r is the permittivity, and δ is the skin depth.

Using the equation for the skin depth δ in a conductor [52],

$$\delta = \sqrt{\frac{2\rho}{\omega\mu_0}}, \quad (\text{A.5})$$

we can express β using Eqs. A.2, A.3, and A.5 as

$$\beta = \frac{1-i}{\delta}. \quad (\text{A.6})$$

For the limit where the thin film thickness is much less than the skin depth ($d \ll \delta$), we have

$$\tan \beta d = \tan \left[(1-i) \frac{d}{\delta} \right] \approx (1-i) \frac{d}{\delta} \quad (\text{A.7})$$

Now, we can simplify Eq. A.1 to

$$Z_{in} = Z_s \frac{Z_d + (1+i) \frac{d}{\delta} Z_s}{Z_s + (1+i) \frac{d}{\delta} Z_d}. \quad (\text{A.8})$$

Putting $Z_S = R_S(1 + i)$ (Eq. A.3) into Eq. A.8,

$$Z_{in} = \frac{Z_d + i2\frac{d}{\delta}R_S}{1 + \frac{d}{\delta}\frac{Z_d}{R_S}} \quad (\text{A.9})$$

$$= \frac{\frac{\rho}{d} + i\frac{\omega\mu_0\rho}{Z_0/\sqrt{\epsilon_r}}}{1 + \frac{\rho/d}{Z_0/\sqrt{\epsilon_r}}}. \quad (\text{A.10})$$

We find that in our system, the imaginary part of Z_{in} is small. This can be found using the parameters

$$\begin{aligned} \omega &= 2\pi (8 \times 10^9) \text{ GHz} \\ \mu_0 &= 4\pi \times 10^{-7} \text{ H/m} \\ \rho &= 2.4 \times 10^{-8} \text{ }\Omega\text{m} \\ Z_0 &= 377 \text{ }\Omega \\ \epsilon_r &= 6, \end{aligned} \quad (\text{A.11})$$

which give

$$\text{Im } Z_{in} \approx 10^{-5} \text{ }\Omega \ll \text{Re } Z_{in}. \quad (\text{A.12})$$

Also, we can compute the dielectric component to Eq. A.10, using $\epsilon_r \approx 6$ for glass:

$$\frac{Z_0}{\sqrt{\epsilon_r}} \approx 154 \text{ }\Omega. \quad (\text{A.13})$$

Thus, for the thin film to dominate the measurement, we need the sheet resistance R_x to be

$$R_x = \frac{\rho}{d} \lesssim 154 \text{ }\Omega. \quad (\text{A.14})$$

In this limit, then, we conclude that the input impedance to the sample is equal to the sheet resistance: $Z_{in} = R_x$.

Appendix B

Disentangling Sheet Resistance and Topography

B.1 Introduction

As described in Secs. 3.3 and 3.4, the microscope output signals (Δf and Q) are a function of both sample sheet resistance and probe-sample separation, for conducting thin-film samples. The method described in Sec. 3.4 is valid for planar samples, where the probe-sample separation is not variable. However, for samples that are not planar, this method can no longer be used, because the probe-sample separation at a given point on the sample is unknown. In order to solve this problem, we developed an algorithm which disentangles the sheet resistance and sample topography from the Δf and Q signals. The concept is simple: there are two variables which have known values, namely, Δf and Q . There are also two variables which have unknown values: sheet resistance R_x , and probe-sample separation h . If a relationship between these four quantities can be obtained, the two known quantities can be used to calculate the two unknown quantities. In other words, one can obtain the following functions

$$R_x = R_x(\Delta f, Q) \tag{B.1}$$

$$h = h(\Delta f, Q) \quad (\text{B.2})$$

to convert Δf and Q into R_x and h . This algorithm has a U.S. patent pending [6].

B.2 Description of the Disentangling Algorithm

To determine $h(\Delta f, Q)$, we generate a surface plot as shown in Fig. B.1(a) using the data presented in Fig. 3.3(a). Next, a fitting function is found which closely approximates the surface $h(\Delta f, Q)$. We use a fitting function of the form

$$h(\Delta f, Q) = A + \frac{B_1}{\Delta f} + \frac{B_2}{Q} + \frac{B_3}{\Delta f Q + B_4} + C_1 \Delta f + C_2 Q + C_3 \Delta f Q \quad (\text{B.3})$$

where A , B_1 , B_2 , B_3 , B_4 , C_1 , C_2 , and C_3 are fitting parameters.

Because the function $R_x(\Delta f, Q)$ is multi-valued with a difficult shape to fit, we instead use the function $R_x(\Delta f, h)$, using the value of h which has already been determined from $h(\Delta f, Q)$ in the previous step. The surface for $R_x(\Delta f, h)$ is shown in Fig. B.1(b). Finally, a fitting function is found of the form

$$\Delta f(R_x, h) = A' + \frac{B'_1}{h} + \frac{B'_2}{R_x} + \frac{B'_3}{h R_x + B'_4} + C'_1 h + C'_2 R_x + C'_3 h R_x \quad (\text{B.4})$$

where A' , B'_1 , B'_2 , B'_3 , B'_4 , C'_1 , C'_2 , and C'_3 are fitting parameters. With the values of Δf and h known, the value of R_x is found by numerically solving Eq. B.4 for R_x .

Once the two fitting functions have been determined, generating images of h and R_x is simply a matter of substituting the Δf and Q data into the fitting function $h(\Delta f, Q)$, and numerically solving $\Delta f(R_x, h)$ for R_x . The implementation of this algorithm was done by Johan Feenstra, using my images of the $\text{YBa}_2\text{Cu}_3\text{O}_{7-\delta}$ thin film presented in Fig. 3.4. The resulting h and R_x images are shown in Fig.

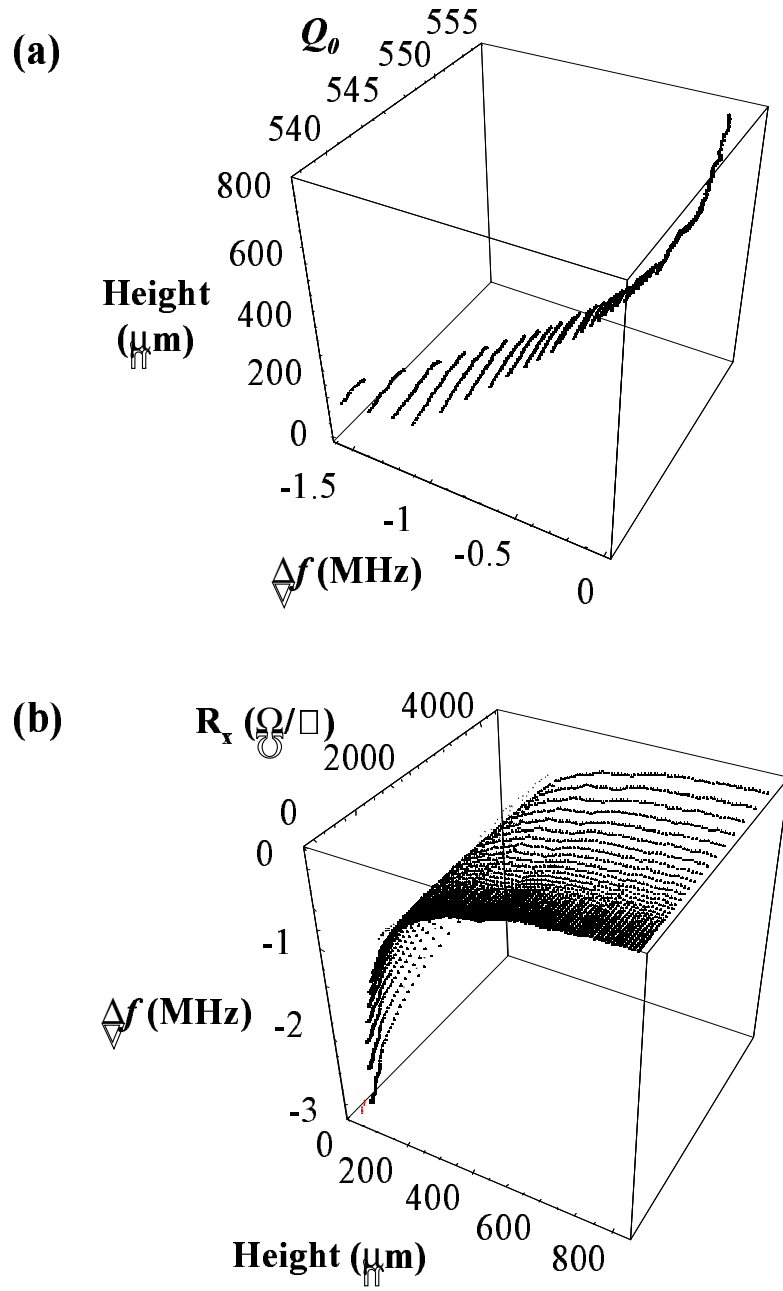


Figure B.1: Surface plots to disentangle sample sheet resistance R_x and probe-sample separation h from Δf and Q . (a) Probe sample separation h as a function of Δf and Q . (b) Sheet resistance R_x as a function of Δf and h .

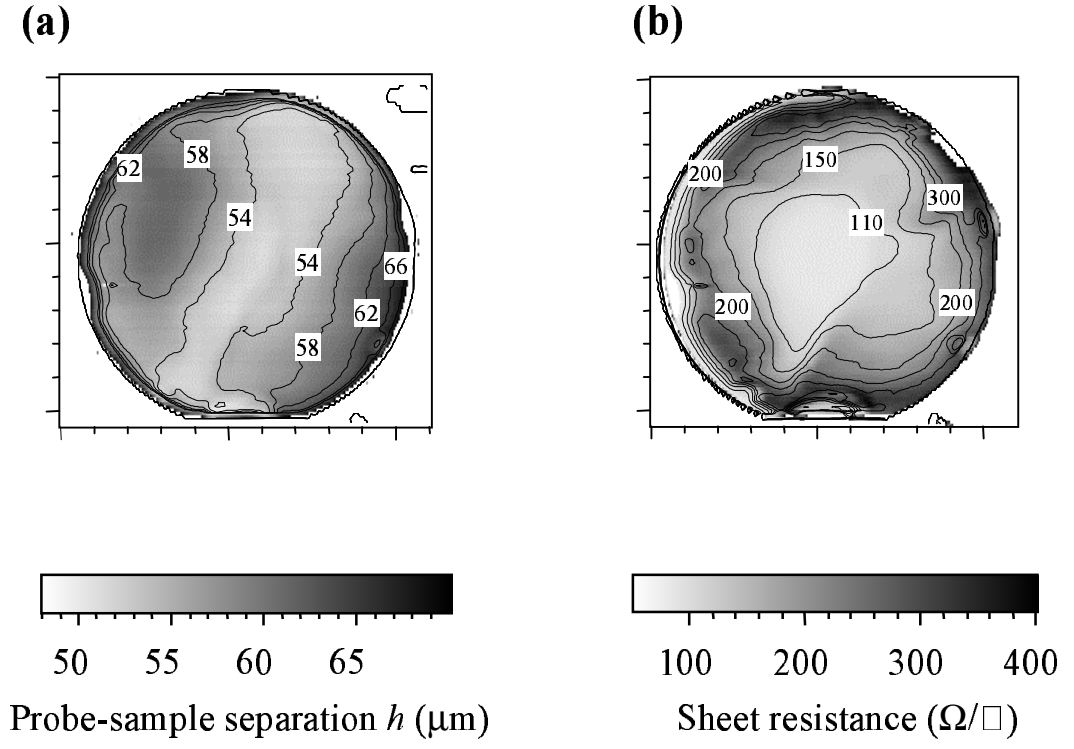


Figure B.2: Images of (a) probe-sample separation h , and (b) sheet resistance R_x of a $\text{YBa}_2\text{Cu}_3\text{O}_{7-\delta}$ thin-film sample at 7.5 GHz. Scan region is $5 \times 5 \text{ cm}^2$.

B.2. The topography data shown in (b) was confirmed quantitatively using a Dektak profilometer scan across the sample [6].

A limitation of this method is due to the dependence of Δf and Q on other sample parameters. In particular, Δf is sensitive to the permittivity of the sample substrate, as well as to the thickness of the sample. As a result, accurate calculation of R_x and h can only be accomplished using a calibration thin-film sample having a substrate with the same permittivity and thickness as the sample to be imaged. This in fact was not the case for the $\text{YBa}_2\text{Cu}_3\text{O}_{7-\delta}$ images in Fig. B.2. The $\text{YBa}_2\text{Cu}_3\text{O}_{7-\delta}$ thin film was on a $300\text{ }\mu\text{m}$ thick sapphire substrate, with a relative permittivity of about 10, while the aluminum thin film calibration sample had a 1.2 mm thick glass substrate, with a relative permittivity of about 6. However, despite this discrepancy, the h image in Fig. B.2(a) is surprisingly accurate.

Appendix C

Microwave Microscope Operating Procedure

C.1 Introduction

This appendix contains a description of the procedure for operate the scanning microwave microscope. Section C.2 instructs the user on how to turn on the instrumentation and set up the microscope components. Section C.3 describes the Runtime data acquisition software, and leads the user through the steps to run a scan. Section C.4 describes the usage of Transform software to visually represent the data in image form. Section C.5 gives other important information. Finally, Sec. C.6 describes new capabilities in Runtime version 5.12 which were not present in version 4.01 (the version which we use with our original microwave microscope instrument). This description is specifically written for my system using Runtime version 5.0 or greater with an Aerotech Unidex 12 motor controller, although it is applicable to our other scanning systems as well.

C.2 Setting up the Experiment

C.2.1 Components

See Fig. C.1 for a diagram of the system. A microwave source (1) is frequency modulated by a function generator (2), and a feedback circuit (7) keeps the source locked onto a resonant frequency of the transmission line resonator. For more information on how the feedback circuit works, see Chapter 2. Several sizes of coaxial probes are available. The resolution is determined by the diameter of the center conductor. The easiest probe to use has a 500 μm -diameter center conductor. There are also probes with 200 μm , 100 μm , and STM tip center conductors. We use flexible coaxial cables for the resonator, such as Gore ReadyFlex cables [115]. To start, use the indicated settings for the instruments. After becoming familiar with the system, feel free to adjust any of these settings.

C.2.2 Getting the Feedback Circuit Locked

Once all the instruments but the frequency-following circuit (FFC) are on and initialized, it is time to frequency lock the circuit. With one hand, hold in the “zero” button on the FFC. With the other hand, turn on the FFC power. While still holding in the “zero” button, adjust the frequency knob on the microwave source and watch the sinusoidal sweep from the diode detector amplifier (4) on the oscilloscope display. When the sinusoidal pattern suddenly turns into a pattern with half its original wavelength, adjust the microwave frequency until this pattern appears like a perfect sine wave, as shown in Fig. 2.6(e). The microwave source is now very close to a resonant frequency.

If you have not yet optimized the phase settings of the lock-in amplifiers, you

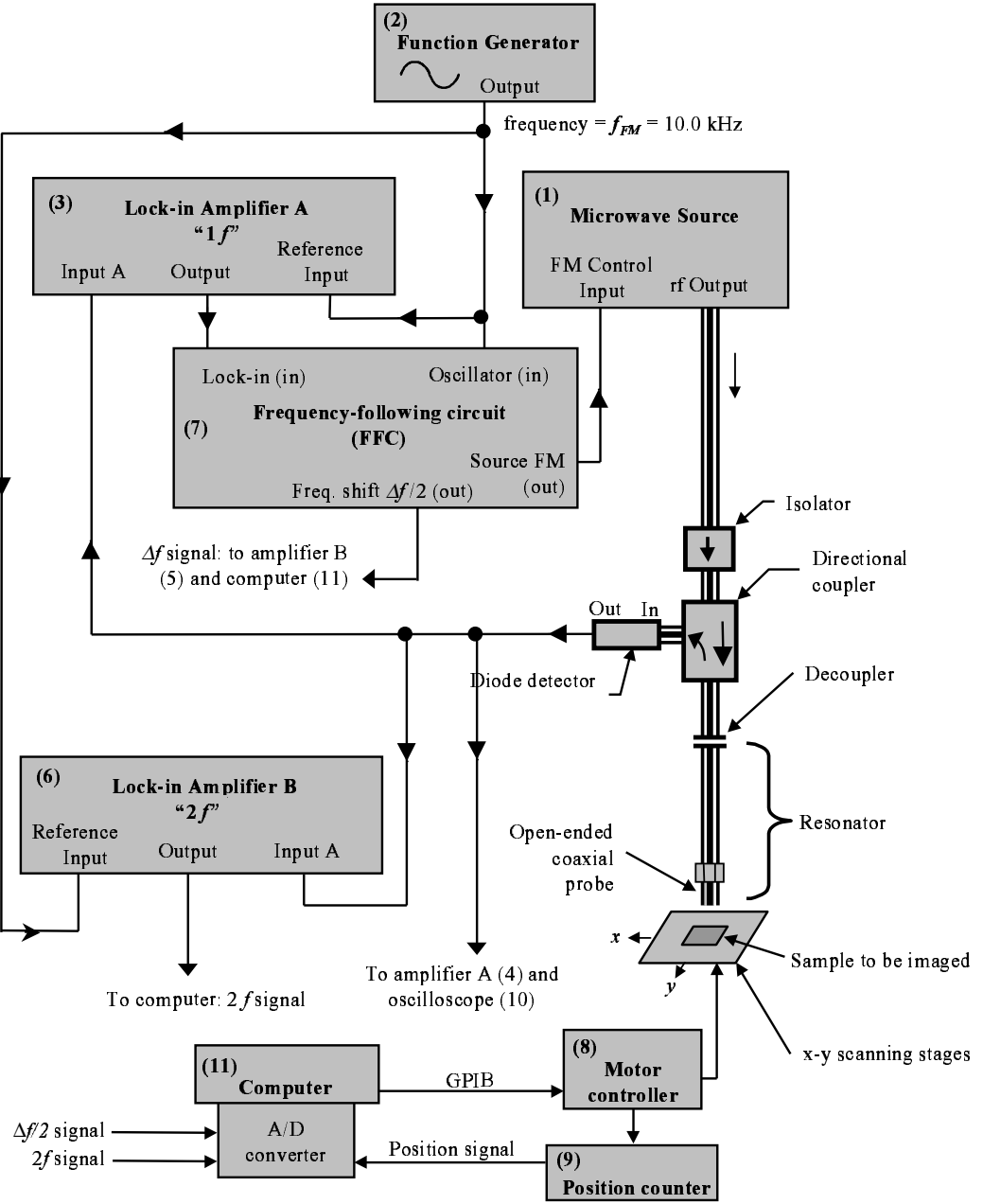


Figure C.1: Microwave microscope circuit diagram. The triple lines are microwave coaxial cables; most solid lines are low-frequency BNC cables.

Component	Settings and Comments
(1) Wavetek 904, 907, or 907A, or HP83620B microwave source	Mode = "FM", output = "ON", leveled = "ON"
(2) HP 33120A function generator	Frequency = 10.0 kHz, amplitude = 1.5 VPP, Offset = 0
(3) $1f$ Lock-in amplifier: Stanford Research SR830	Sensitivity = 1 mV, phase = 0° , time constant = 100 μ s, harmonic = 1, filters: 60 Hz, 120 Hz, bandpass
(4) Amplifier A (diode detector amplifier): Stanford Research SR560:	Gain = 200, filter = 30 kHz low-pass with 12 dB roll-off, invert = OFF
(5) Amplifier B (frequency shift amplifier): SR 560 or Krohn-Hite 3202 low-pass filter	Gain = 1 or 2, filter = 30 Hz low-pass with maximum roll-off, invert = OFF
(6) $2f$ Lock-in amplifier (EG & G 5210)	Sensitivity = 1 mV, phase = 25° , time constant = 30 ms, harmonic = 2
(7) Frequency-following circuit (FFC):	Gain = 1; notice that the Δf output is divided by 2
(8) Aerotech Unidex 12, or other motor controller	
(9) Position counter circuit	Used to keep track of position of the scanning motor
(10) HP 54603 Oscilloscope	Channel 1 connected to amplifier A (4) output; channel 2 connected to amplifier B (5) output. External trigger input connected to synchronous output of function generator (2).
(11) Computer	Controls the scanning stages, and acquires data through A/D converter board
(12) Isolator	Reduces unwanted resonances external to the microscope resonator
(13) Directional coupler	Extracts part of reflected signal, sending it to the diode detector
(14) Decoupler	A coupling capacitor for coupling the microwave source to the resonator
(15) Open-ended coaxial probe	Sizes available (center conductor diameter): 500 μ m, 200 μ m, 100 μ m, and STM tip probe
(16) Diode detector: HP 8473C	Converts rf power input to dc voltage output

Table C.1: List of components for the microwave microscope

will need to do that now. While still holding down the “zero” button, turn the microwave source frequency knob so that the source is slightly off resonance. Now, adjust the phase of the $1f$ lock-in (3) until the “Y” (quadrature) output display on the lock-in indicates an output as close as possible to 0 V. Release the “zero” button. If the oscilloscope shows a clean sinusoidal signal, the feedback circuit is locked. If there is a sinusoidal signal, but it looks distorted, turn the microwave frequency knob slightly until it looks better. If there is no sinusoidal signal at all, the phase of the $1f$ lock-in is probably off by 180° . Press the “zero” button again. Then change the phase of the $1f$ lock-in by 180° . This is most easily done by pressing the “ $+90^\circ$ ” button on the lock-in twice. Now let go of the “zero” button. There should be a clean sinusoidal signal on the oscilloscope. If it is distorted, adjust the microwave frequency slightly. If everything is working properly, the sinusoidal pattern will remain on the display, even when the frequency of the source is adjusted slightly. The circuit is now locked. If none of this works, increase the sensitivity setting on the $1f$ lock-in to a value greater than 1 mV, and try again.

One problem to be aware of is making sure that you lock onto a resonance, not an “anti-resonance.” Referring to Fig. 2.2, it is important to lock onto a resonant minimum, instead of the maximum between resonant minima. To check this, view the amplified diode detector signal (with invert off on amplifier A) on the oscilloscope in “DC” mode, instead of “AC” mode. You might need to reduce the gain to view the signal. Now, turn the frequency dial on the microwave source while holding in the “zero” button on the FFC. When the frequency is near a resonant minimum (which is actually a maximum in the voltage, since the diode detector is a negative voltage), the trace on the oscilloscope will be close to 0

V. When the frequency is near an “anti-resonance,” the trace on the oscilloscope will be at some minimum voltage, which is negative. When the system is locked, make sure that the absolute voltage is near 0 V, at a maximum.

C.2.3 Optimizing the Feedback Settings

Reduce the sensitivity setting (increase the gain) of the $1f$ lock-in (3) until the system either loses lock completely (the sinusoidal signal on the oscilloscope will disappear), or the circuit begins to oscillate. Then increase the sensitivity value by one increment, so that all oscillations disappear. This is the optimum sensitivity for the lock-in, giving the feedback circuit its optimum gain.

With the circuit locked, adjust the phase of the $2f$ lock-in until the “Y” (quadrature) display of the $2f$ lock-in indicates a value of 0 V. Then, adjust the sensitivity of the $2f$ lock-in until the “X” output is less than 10 V, but as large as possible. This is an important step, so that as much as possible of the lock-in amplifier’s range of -10 V to $+10$ V is used.

For a given system, all these settings only need to be adjusted once, unless a change is made to the circuit, resonator, or probe.

C.3 Using the Runtime software

The original Runtime version 4.01 program was written by Randy Black in Visual Basic [71] for use with a scanning SQUID microscope [16]. I modified it for use with my scanning system, and added new functionality. The most recent version is Runtime 5.12 from April 14, 2000.

C.3.1 Loading a Configuration

Now it is time to begin using the computer software. Start up the program “Runtime 5.12” on the computer. In the **File** menu, select **Load Configuration**. A file dialog box will appear, with the current directory “C:\Runtime 5.12”. This is the directory that contains several standard configurations. You may eventually want to create your own, and save it using **Save Configuration** in the **File** menu. Now, open the file “2-input.cfg”. This is a good configuration to start with.

C.3.2 Dependent Variable Settings

Now select **Analog input (ADC1)** from the **Dep. Vars.** menu. A new window will appear. The check boxes along the left hand side allow the user to select which A/D channels the software should record while scanning. Right now, channels 0 and 1 will be selected. The next column contains names for the channels. The first two channels are named “Freq shift” and “2F”. These names can be modified to describe what type of data is being acquired by the different channels. On the right hand side of the menu, there are boxes labeled “sample interval” and “scan interval”. The scan interval is the period of the A/D board sampling. It is set to 0.3 ms, so that the A/D board will read from the channels every 0.3 ms. The sample interval is the period of time the A/D board will look at each channel. This should be as large as possible for a given scan interval. Since we are reading from three channels (channels 0 and 1, and also channel 7 for the position counter) we set the sample interval to 1/3 of the scan interval, or 0.1 ms. Finally, the box labeled “Number of points to average” tells how many points acquired every 0.3 ms will be averaged and saved as a single data point for the

final image. Now click the **OK** button to close the window.

C.3.3 Independent Variable Settings

Next, select **X Pos (unidex)** from the **Indep. Vars.** menu (if you are using a system with another type of motor controller, select the appropriate x-axis variable). A new window will appear. This is where the user can set many different parameters for the x-axis of the motor controller. Here is a brief description of several of the parameters that you may want to adjust in the future:

1. Ramp time: The time the motors will take to get up to speed. Must be at least 50 ms. Recommended value for a typical scan: 250 ms.
2. Slow (mm/s): Not used in Runtime version 5.x for the Unidex motors.
3. Scan (mm/s): Speed at which the x-axis will move while data is being acquired. For a typical sample, set this to 1 mm/s.
4. Fast (mm/s): Speed at which the x-axis will move when the stage is being moved but data is not being acquired. To run the scan as fast as possible, set this to 25 mm/s, the maximum speed of the translation stage.
5. Overshoot: Offset from the beginning of each scan line, to allow time for the motor to get up to speed. The sign of the overshoot is important. If the scan is going from low x to a higher x value, the overshoot should be negative, and vice versa.
6. **Synchronize Now** button: Forces the Unidex motor controller to reset, and home both axes (this will be described below)

7. **Synchronize MT7 in place** button: Instructs the software to read the position of the x-axis, and update its settings for the position counter.
8. **Synchronize MT7,8,9 enter positions** button: Allows the user to initialize the position of the X, Y, and Z motors by entering their positions. This is useful if the computer loses its GPIB connection with the motor controller, or if the computer crashes.

Now click the **OK** button. There is a similar window for the y- and z- axes, which can be opened by selecting **Y Pos unidex** and **Z Pos unidex** from the **Indep. Vars.** menu.

C.3.4 The Control Panel

The control panel is used to adjust the translation stage position by hand. Now open the control panel by selecting **Control Panel** from the **Action** menu. Current A/D board readings of the active channels are shown in the upper part of the window. The lower part of the window is used to move the translation stage. In the box next to the upper button labeled **Goto**, type the number 10 and then click the **Goto** button next to the box. A dialog box will appear, warning you that the Unidex controller is going to home the motors. Click **OK**. Now you will see the x- and y-axis of the stage slowly moving to the zero position. Note that this happens only the first time you give a motor move command. Once the motors are homed, the x-axis will move to the position you gave it, 10 mm. The positions of the x- and y- axes can be between 0 and 100 mm. Similarly, you can adjust the y-axis with the lower **Goto** button in the window. The z-axis is homed in the same manner.

Now is the time to put your sample on the translation stage of the microscope. Start with a large sample (at least a few mm across). Once you are familiar with the system, you may wish to scan smaller samples. Put it near the center of the stage. Then we will use the control panel to find the positions of the four corners of the region of the sample that you wish to scan. Using the Control Panel, move the x-axis to the left edge of the sample. Then, move the y-axis to the upper edge. Write down the position of the upper-left corner of the scan region. Do the same for the lower-right corner of the sample. We will use these as the boundaries for the scan.

C.3.5 Setting the Probe Height

Now, using the Control Panel, move the translation stage so that the probe is approximately above the center of the sample, in order to adjust the height of the probe. Turn off the frequency following circuit before adjusting the probe height. Otherwise, when the probe is brought in contact with the sample, the frequency-following circuit will saturate and lose its lock, resulting in a constant voltage signal of +15 or -15 V to be applied to the microwave source FM input.

If you are using a system with a manual micrometer control for the z-axis, use the following procedure to find the position at which the probe touches the sample. While looking through the optical microscope, turn the probe height micrometer screw to adjust the probe height. Bring the probe so that it is almost in contact with the sample. Then, tap the top of the micrometer screw while looking through the optical microscope. You will see the probe tip move downward slightly relative to the sample. Move the probe a little closer with the micrometer, and tap it again. When the probe is in contact with the sample, you

will no longer see the probe move relative to the sample when the micrometer is tapped. Be sure to move the probe in small increments so that you do not jam the probe too hard against the sample, causing some damage to the probe or the sample. Once the probe is in contact with the sample, observe and write down the micrometer position. Note that each division is 10 μm . Then move the probe away. For the 500 μm probe, move it away at least 200 μm (20 divisions on the micrometer). This is so that the probe doesn't scratch the sample during the initial scan (the sample stage might be tilted). If you are using a system with a z-axis motor, you will need to do this operation using the **Control Panel** to move the z motor. Be careful not to jam the probe into the sample; this could damage the probe, sample, and other expensive things such as the z-axis scanning stage. To prevent significant damage to the system, it would be wise to have the z-axis within 1 mm of its lower limit when the probe is in contact with the sample. Now you may turn on the frequency-following circuit again. Close the **Control Panel** by clicking **OK**.

C.3.6 Setting Scan Parameters and Running the Scan

Bring up the scan parameters window by clicking **Acquire Data Set** in the **Action** menu. Then click the **Edit Scenes** button. A window will appear which allows you to set the bounds for a scan. Near the top of the window there are two boxes, labeled "Start Val" and "Stop Val." This is where you set the beginning and ending positions of the x-axis for each scan line. Enter the values that you wrote down earlier for the left and right edges of your sample. Farther down in the window are three more boxes, "Start Val", "Step Val", and "Num Vals." Set the start value to the position of the y-axis at the top edge of your sample. Set

the step value to the spacing you want between raster lines in the scan. Then, set Num Vals to the number of scan lines you want in the scan. For a sample that is 10 mm tall, for example, you could set Step Val to 1 mm, and Num Vals to 11. Click **OK** to close the window.

Now the **Acquire Data Set** window is open. The three boxes along the top allow the user to specify the filename for their data. The text in the three boxes will be concatenated to make the filename. A suggested format is to use the first box to specify your name (with your first initial, for example), the second box as an index number of the scan, and the third box to describe the sample being scanned. For example, I might name my 245th scan which is of a YBCO sample “D245-YBCO” by typing “D”, “245”, and “-YBCO” in the three boxes. The next five boxes down are all optional. You might want to at least enter the date. You can also enter comments for the scan. When you are ready to begin scanning, click **Begin Scanning**. Another window will open, and the microscope will begin the scan. You may pause the scan at any time by clicking **Pause**. Once paused, you can automatically re-scale the graph of the current scan line by clicking **Rescale**, or manually change the scale by clicking on one of the vertical scale boxes, typing a new value, and pressing Enter. You can abort the scan by clicking **Abort**, or resume by clicking **Resume**. Once the scan has completed, the computer will tell you by bringing up a dialog box.

C.3.7 Saving Your Data

Under the **File** menu, click **Save** to save the file in binary format. The file will have the extension “.dat”. Be sure to create your own directory in which to save your files.

Click **Save to ASCII grid** to save an image in text format. A window will appear which is mainly to give you information about the scan. In the lower right corner, you can select which channel you would like to save the data from. Then click OK. A file name dialog box will appear. The file will have the extension “.grd”. The file will be saved in a format which can be read by Transform, a data-visualization program.

C.4 Using Transform to View Your Data

Open the application “Transform” [36]. If you don’t have Transform, another program such as Origin [70] can be used. I do not recommend Transform if you don’t own it already: it is poorly designed, and not worth the money. Select **Open** in the **File** menu. Enter the filename of one of your saved “.grd” files, and click **Open**. The data will now appear in table form. Select **Generate image** from the **Image** menu. Try out different color tables in the **Color Tables** menu. Two good ones to try are Rainbow or Seismic. When viewing an image, the five buttons visible along the left side of the window are, from top to bottom, for (1) selecting a region of the image, (2) adjusting the color attributes, (3) “fiddling” with the color bar (try this out by clicking in different areas of the image window), (4) resizing, and (5) setting axis attributes such as scales.

You can also save your file in Transform’s “.hdf” format (**Save** in the **File** menu) and print it (**Print** in the **File** menu).

C.5 Other Information

C.5.1 Re-establishing Your GPIB Connected With the Motor Controller

From time to time the Unidex motor controller loses its GPIB connection with the computer. This is a hardware problem with the Unidex controller, rather than a software problem. It often occurs if you send the motor controller a command which will take a long time to execute (longer than 17 seconds). When this happens, a dialog box will appear that says “GPIB error.” First, click **Open Connection**. Wait for a message to appear in the status display. If an error appears, you will need to turn the motor controller off and then on, click **Exit, Reset Motors**, and home the motors again (don’t forget to move the probe and sample apart first, to prevent damage to either). If no error appears, click **Restore Motor Positions**. Finally, click **Exit, Ignore Error**. If this works (it will unless the motor controller has crashed, which happens occasionally), the Runtime software will have restored everything back to normal, despite the Unidex controller’s best efforts to ruin your day.

C.5.2 Viewing Images in Runtime

Runtime 5.x also lets you view an image in gray-scale form. Click **View Frame** in the **Action** menu. Then, using the box in the lower right corner of the window, select which channel to use. Then click **OK** to view the image. This is a quick way to see your results. Use Transform (see Sec. C.4) to view your image in color and with custom color bars.

C.5.3 Adjusting the Tilt of the Sample and Probe

When you run your first scan, most likely you will observe an overall tilt in the image. This is due to the surface of your sample not being parallel to the translation axes. The tilt can be adjusted by two micrometers on the sample tilt stage. Try adjusting these, and scanning again. It can take a lot of time to achieve acceptable results. A good way to adjust the tilt more quickly is to set up a high-speed scan (set the scan speed to 25 mm/s) with a small number of scan lines over the sample (less than ten). Then, observe the probe and sample through the optical microscope while the scan is running. You will be able to see whether there is an overall tilt to the sample, and adjust it while the scan is running. This method will at least allow you to quickly get the tilt of the stage close to being parallel to the axes. You probably will still need to run trial scans of the sample, adjusting the tilt depending on what you see in the scan image.

Make sure you start out with the probe far away (at least 200 μm for the 500 μm probe) until you get the tilt adjusted better. Then, you may move the probe closer in. The closer the probe is to the sample, the more sensitive your data will be to small errors in the tilt of the sample. For the 500 μm probe, a good scanning height is 50 μm . For the smaller probes, the probe will need to be much closer to achieve an acceptable signal-to-noise ratio.

Once you get the stage tilt at least close to parallel, you might also want to adjust the tilt of the probe so that the surface of the probe tip is parallel to the surface of your sample. The probe tilt is adjusted using the six “push/pull” thumb screws in the probe holder. These push/pull screws are in pairs. One member of each pair pushes on the bottom probe mount plate, and has its head flush with the top probe holder plate; the other member is the “pull” screw, and

has its head spaced above the top probe holder plate. This arrangement allows the screws to be tightened so that the probe alignment will not be lost even if the probe holder is bumped accidentally. Before adjusting the probe tilt, loosen the bottom probe mount plate by loosening one screw from each of the three pairs. Then, adjust the tilt by turning one pair of screws in opposite directions. For example, if you want to lower one edge of the bottom probe mount plate, loosen the “pull” screw by turning it counterclockwise; then tighten the “push” screw by turning it clockwise. After you have adjusted the tilt, tighten all three pairs of screws so that the probe tilt will not shift.

C.6 Additional Capabilities of Runtime

Needing to use Runtime for new types of scanning, I added new functionality to the software. Descriptions of these new capabilities are given below.

C.6.1 Z-Axis Slow Approach

For the z-axis, there is an additional parameter, the “slow-approach distance,” which can be set in the **MT9 Parameters** window. This gives a certain distance where the z-axis will slow down from its fast speed to its scan speed. I always use a value of 0.1 mm for the slow-approach distance, and a value of 0.05 mm/s for the z-axis scan speed for contact mode imaging. This slow-approach distance is also used by Runtime when bringing the probe back into contact with the sample from its background measurement position (see Sec. C.6.4).

C.6.2 Recording Scaled Data

It is much more useful to record frequency shift in kHz rather than in volts, and the Q as its actual value, rather than in volts. This is done by giving a multiplier and an offset to the data in the **ADC1 Data Acquisition Parameters** window, in the columns marked “Multiplier” and “Offset.” For example, for our Wavetek 907A microwave source, the FM input conversion factor is 2.41 MHz/V. Also, the FFC divides the frequency shift signal by 2. Thus, if using this microwave source, you should enter a multiplier of 4820 and an offset of 0. To convert from the $2f$ voltage to Q , you will also need a multiplier. The multiplier and offset are the A and B parameters in Fig. 2.8.

C.6.3 Step Scans

A step scan is defined as a scan where the motors stop at each point to acquire data, rather than taking data while the x-axis is in motion. Step scanning was required for contact-mode imaging, due to vibrations which occur while the motors are in motion. To do a step scan, click on the “Step Scan” check box in the **Scene Program** window so that it is checked. Now, set the step size in the “Step Val” box. If you want the probe to retract between scan lines (I recommend this), check the box marked “Non-drag on return.” If you want the probe to retract between all points on the sample, so that the probe is never dragged across the sample, check the box “Non-drag between points.” This mode causes the least damage to the probe, but significantly increases the time it takes to acquire a scan. In the “Z (MT9) Displacement (mm)” box, set the distance to retract the probe with the z-axis motor.

In the “First point delay” box, set the time (in ms) to wait at the beginning

of each scan line, before taking data. This is to allow time for vibrations to be dampened. In the “Step delay” box, set the time to wait at points which aren’t the first point in the scan line. You might need the first point delay to be larger than the step delay.

The “Drag offset” gives a distance to drag the probe before each scan line, which seems to help with some scans. The sign of this distance matters, so if you are scanning in the positive x direction, this offset should be negative.

C.6.4 Taking Background Data

If you want to take background data, check the box marked “Record background at start of each scan line”. Set the distance to retract the probe in the “Offset distance” box. I recommend at least 3 mm. In the **ADC1 Data Acquisition Parameters** window, you can indicate how to treat the background data for each channel, in the column marked “Operation”. The possible values here are:

Setting	Description
N	No operation: ignore background value
S	Subtract background value from data value
D	Divide data value by background value

The “S” setting is useful for the frequency shift signal, while the “D” setting is useful for the “2f” signal.

C.6.5 Bidirectional Scans

Bidirectional scans are for taking single hysteresis loops at one point on the sample, or at multiple points along one line. Check the box “Bidirectional scan”

to select this mode. The x-axis variable will be used for the hysteresis loop, so set it to one of the two analog output voltage channels. In the “Initial Val” box, set the initial value for the variable. In the “Start Val” and “End Val” box, set the minimum and maximum values for the scan. In the “Step Val” box, set the amount to change the variable for each data point. For example, if you want a hysteresis loop centered at 0 V, with the range -5 V to $+5$ V, enter an initial value of 0, a start value of -5 , and an end value of $+5$. In the “Number of linear scans” box, set the number of linear scans you want. For example, if you want to scan from 0 V to 5 V, down to -5 V, and back up to 0 V, set this value to 3.

C.6.6 Hysteresis Scans

The hysteresis scan capability is different from the bidirectional scan capability, in that it can be used for a 2-dimensional image. Also, the data is saved differently (see below). Check the “Hysteresis scan” box to do a hysteresis scan. Set the hysteresis variable in the “Hysteresis variable” box. The “Start Value” is the initial value for the hysteresis variable, and the “Min Value” and “Max Value” are the minimum and maximum values. For example, to have a hysteresis loop centered at 0 V, with the range -5 V to $+5$ V, enter the values 0, -5 , and 5 for the start, minimum, and maximum values. The “Increment” is how much to change the hysteresis variable for each new data point. The “Delay time (ms)” is how long to wait before taking each new data point. Enter the number of hysteresis loops to acquire at each point on the sample in the “# of loops” box. On the other hand, if you would like to do a single sweep from the minimum to the maximum value, check the “Single sweep” box; otherwise, make sure this box is unchecked. An estimate of the number of data points per position on the

sample will be given in the “Number of data points” box. For a hysteresis scan, each point on the hysteresis loop will have to be saved in a separate text file when you save the grid files.

C.6.7 Scans at Multiple Frequencies

The independent variable “HP83620B” can be used to set the frequency of an HP 83620B Microwave Source, through a GPIB connection. Make sure the microwave source has a GPIB address of 25. Test the connection by using the **Control Panel** in Runtime. When a frequency command is sent, Runtime sends four identical commands, about half a second apart. This is required for the frequency to be stable. I think this is a problem with the HP microwave source, when it is in DC-FM mode. Because of this time delay, this frequency control shouldn’t be used for a frequency sweep.

To scan at multiple frequencies, click the **Edit Program** button in the **Scene Program** window. Then you may add commands to change the frequency. The scans will be taken sequentially, and will need to be saved in separate grid files. Each individual scan is called a “frame” in this context.

BIBLIOGRAPHY

- [1] F. Abbas, L. E. Davis, and J. C. Gallop, “Tunable microwave components based on dielectric nonlinearity by using HTS/ferroelectric thin films,” *IEEE Trans. Appl. Supercond.*, vol. 5, p. 3511, 1995.
- [2] E. Abbè, “Beiträge zur theorie des mikroskops und der mikroskopischen wahrnehmung,” *Archiv Mikroskopische Anat.*, vol. 9, p. 413, 1873.
- [3] S. Aggarwal, A. M. Dhote, R. Ramesh, W. L. Warren, G. E. Pike, D. Dimos, M. V. Raymond, B. A. Tuttle, and J. J. T. Evans, “Hysteresis relaxation in (Pb,La)(Zr,Ti)O₃ thin film capacitors with (La,Sr)CoO₃ electrodes,” *Appl. Phys. Lett.*, vol. 69, p. 2540, 1996.
- [4] J. E. Aitken, “Swept-frequency microwave Q -factor measurement,” *Proc. IEE*, vol. 123, p. 855, 1997.
- [5] H. M. Altshuler in *Handbook of Microwave Measurements II*, pp. 530–533, New York: Polytechnic Inst. of Brooklyn, 1963.
- [6] S. M. Anlage, B. J. Feenstra, and D. E. Steinhauer. U.S. Patent Pending, application 09/473,961, filed Dec., 1999.
- [7] S. M. Anlage, D. E. Steinhauer, C. P. Vlahacos, and F. C. Wellstood. U.S. Patent Pending, filed April, 2000.

- [8] S. M. Anlage, D. E. Steinhauer, B. J. Feenstra, C. P. Vlahacos, and F. C. Wellstood, "Near-field microwave microscopy of materials properties," in *Microwave Superconductivity*, Kluwer, Amsterdam, 2000.
- [9] S. M. Anlage, D. E. Steinhauer, C. P. Vlahacos, B. J. Feenstra, A. S. Thanawalla, W. Hu, S. K. Dutta, and F. C. Wellstood, "Superconducting materials diagnostics using a scanning near-field microwave microscope," *IEEE Trans. Appl. Supercond.*, vol. 9, p. 4127, 1999.
- [10] S. M. Anlage, C. P. Vlahacos, S. Dutta, and F. C. Wellstood, "Scanning microwave microscopy of active superconducting microwave devices," *IEEE Trans. Appl. Supercond.*, vol. 7, p. 3686, 1997.
- [11] S. M. Anlage, F. C. Wellstood, C. P. Vlahacos, and D. E. Steinhauer. U.S. Patent No. 5,900,618, issued May 4, 1999.
- [12] E. H. Ash and G. Nicholls, "Super-resolution aperture scanning microscope," *Nature*, vol. 237, p. 510, 1972.
- [13] C. Basceri, S. K. Streiffer, and A. I. Kingon, "The dielectric response as a function of temperature and film thickness of fiber-textured (Ba,Sr)TiO₃ thin films grown by chemical vapor deposition," *J. Appl. Phys.*, vol. 82, p. 2497, 1997.
- [14] N. Belhadj-Tahar, A. Fourier-Lamer, and H. de Chanterac, "Broad-band simultaneous measurement of complex permittivity and permeability using a coaxial discontinuity," *IEEE MTT-S Int. Microwave Sym.*, vol. 38, p. 1, 1990.

- [15] R. L. Bihan and M. Maussion, "Study of the surface of ferroelectric crystals with the scanning electron microscope," *Ferroelectrics*, vol. 7, p. 307, 1974.
- [16] R. C. Black, *Magnetic microscopy using a superconducting quantum interference device*. PhD thesis, Physics, University of Maryland, College Park, Maryland, 1995.
- [17] J. C. Booth, D. H. Wu, and S. M. Anlage, "A broadband method for the measurement of the surface impedance of thin films at microwave frequencies," *Rev. Sci. Instrum.*, vol. 65, p. 2082, 1994.
- [18] S. I. Bozhevolnyi, J. M. Hvam, K. Pedersen, F. Laurell, H. Karlsson, T. Skettrup, and M. Belmonte, "Second-harmonic imaging of ferroelectric domain walls," *Appl. Phys. Lett.*, vol. 73, p. 1814, 1998.
- [19] C. A. Bryant and J. B. Gunn, "Noncontact technique for the local measurement of semiconductor resistivity," *Rev. Sci. Instrum.*, vol. 36, p. 1614, 1965.
- [20] E. C. Burdette, F. L. Cain, and J. S. Seals, "*In Vivo* probe measurement technique for determining dielectric properties at vhf through microwave frequencies," *IEEE MTT-S Int. Microwave Sym.*, vol. 28, p. 414, 1980.
- [21] R. Cach, A. Jaśkiewicz, and R. Lamber, "Dielectric nonlinearity of TGS near the phase transition temperature," *Acta Physica Polonica*, vol. A62, p. 249, 1982.
- [22] K. R. Carroll, J. M. Pond, D. B. Chrissey, J. S. Horwitz, R. E. Leuchtner, and K. S. Grabowski, "Microwave measurement of the dielectric constant of

- Sr_{0.5}Ba_{0.5}TiO₃ ferroelectric thin films,” *Appl. Phys. Lett.*, vol. 62, p. 1845, 1993.
- [23] R. A. Chakalov, Z. G. Ivanov, Y. A. Boikov, P. Larsson, E. Carlsson, S. Gevorgian, and T. Claeson, “Fabrication and investigation of YBa₂Cu₃O_{7- δ} /Ba_{0.05}Sr_{0.95}TiO₃ thin film structures for voltage runable devices,” *Physica C*, vol. 308, p. 279, 1998.
- [24] Y. Cho, A. Kirihaara, and T. Saeki, “Scanning nonlinear dielectric microscope,” *Rev. Sci. Instrum.*, vol. 67, p. 2297, 1996.
- [25] Y. Cho, S. Atsumi, and K. Nakamura, “Scanning nonlinear dielectric microscope using a lumped constant resonator probe and its application to investigation of ferroelectric polarization distributions,” *Jpn. J. Appl. Phys.*, vol. 36, p. 3152, 1997.
- [26] Y. Cho, S. Kazuta, and K. Matsuura, “Scanning nonlinear dielectric microscopy with nanometer resolution,” *Appl. Phys. Lett.*, vol. 75, p. 2833, 1999.
- [27] R. E. Collin, *Foundations for Microwave Engineering*. New York: McGraw-Hill, 1992.
- [28] Deltronic Crystal Industries, Inc., Dover, New Jersey. From a data sheet on strontium barium niobate.
- [29] Deltronic Crystal Industries, Inc., Dover, New Jersey (phone 973-361-2222).
- [30] A. F. Devonshire, “Theory of barium titanate-part i,” *Phil. Mag., Ser. 7*, vol. 40, p. 1040, 1949.

- [31] D. C. Dube, M. T. Lanagan, J. H. Kim, and S. Lang, “Dielectric measurements on substrate materials at microwave frequencies using a cavity perturbation technique,” *J. Appl. Phys.*, vol. 63, p. 2466, 1988.
- [32] S. K. Dutta, C. P. Vlahacos, D. E. Steinhauer, A. S. Thanawalla, B. J. Feenstra, F. C. W. ans Steven M. Anlage, and H. S. Newman, “Imaging microwave electric fields using a near-field scanning microwave microscope,” *Appl. Phys. Lett.*, vol. 74, p. 156, 1999.
- [33] B. J. Feenstra, C. P. Vlahacos, A. S. Thanawalla, D. E. Steinhauer, S. K. Dutta, F. C. Wellstood, and S. M. Anlage, “Near-field scanning microwave microscopy: measuring local microwave properties and electric field distributions,” *IEEE MTT-S Int. Microwave Sym.*, vol. novolume, p. 965, 1998.
- [34] A. T. Findikoglu, C. Doughty, S. M. Anlage, Q. Li, X. X. Xi, and T. Venkatesan, “DC electric field effect on the microwave properties of $\text{YBa}_2\text{Cu}_3\text{O}_7/\text{SrTiO}_3$ layered structures,” *J. Appl. Phys.*, vol. 76, p. 2937, 1994.
- [35] A. T. Findikoglu, Q. X. Jia, C. Kwon, D. W. Reagor, G. Kaduchak, K. O. Rasmussen, and A. R. Bishop, “Comparative study of broadband electrodynamic properties of single-crystal and thin-film strontium titanate,” *Appl. Phys. Lett.*, vol. 75, p. 4189, 1999.
- [36] Fortner Research, Sterling, Virginia (www.fortner.com). Transform version 3.3.
- [37] J. Gallop, L. Hao, and F. Abbas, “Spatially resolved measurements of HTS microwave surface impedance,” *Physica C*, vol. 282–287, p. 1997, 1997.

- [38] C. S. Ganpule, V. Naharajan, H. Li, A. S. Ogale, D. E. Steinhauer, S. Aggarwal, E. Williams, and R. Ramesh, “Role of 90° domains in lead zirconate titanate thin films,” *Appl. Phys. Lett.*, 2000.
- [39] C. Gao and X.-D. Xiang, “Quantitative microwave near-field microscopy of dielectric properties,” *Rev. Sci. Instrum.*, vol. 69, p. 3846, 1998.
- [40] C. Gao, F. Duewer, and X.-D. Xiang, “Quantitative microwave evanescent microscopy,” *Appl. Phys. Lett.*, vol. 75, p. 3005, 1999.
- [41] S. S. Gevorgian, T. Martinsson, P. L. J. Linnér, and E. L. Kollberg, “CAD models for multilayered substrate interdigital capacitors,” *IEEE MTT-S Int. Microwave Sym.*, vol. 44, p. 896, 1996.
- [42] M. Golosovsky, A. Galkin, and D. Davidov, “High-spatial resolution resistivity mapping of large-area YBCO films by a near-field millimeter-wave microscope,” *IEEE MTT-S Int. Microwave Sym.*, vol. 44, p. 1390, 1996.
- [43] T. E. Harrington, J. Wosik, and S. A. Long, “Open resonator mode patterns for characterization of anisotropic dielectric substrates for HTS thin films,” *IEEE Trans. Appl. Supercond.*, vol. 7, p. 1861, 1997.
- [44] K.-H. Hellwege and A. M. Hellwege, eds., *Londolt-Börnstein: Numerical Data and Functional Relationships in Science and Technology, Ser. III*, vol. 16b. New York: Springer, 1981.
- [45] K.-H. Hellwege and A. M. Hellwege, eds., *Londolt-Börnstein: Numerical Data and Functional Relationships in Science and Technology, Ser. III*, vol. 16a. New York: Springer, 1981.

- [46] B. H. Hoerman, G. M. Ford, L. D. Kaufmann, and B. W. Wessels, “Dielectric properties of epitaxial BaTiO_3 thin films,” *Appl. Phys. Lett.*, vol. 73, p. 2248, 1998.
- [47] S. Hogan, S. Wagner, and F. S. Barnes, “Resistivity measurement of thin semiconductor films on metallic substrates,” *Appl. Phys. Lett.*, vol. 35, p. 77, 1979.
- [48] M. Horioka, A. Sawada, and M. Wada, “Dielectric dispersion in $\text{Li}_2\text{Ge}_7\text{O}_{15}$,” *Ferroelectrics*, vol. 95, p. 233, 1989.
- [49] S. Hoshino, T. Mitsui, F. Jona, and R. Pepinsky, “Dielectric and thermal study of tri-glycine sulfate and tri-glycine fuoberyllate,” *Phys. Rev.*, vol. 107, p. 1255, 1957.
- [50] C. Hubert, J. Levy, A. C. Carter, W. Chang, S. W. Kirchoefer, and J. S. Horwitz, “Confocal scanning optical microscopy of $\text{Ba}_x\text{Sr}_{1-x}\text{TiO}_3$ thin films,” *Appl. Phys. Lett.*, vol. 71, p. 3353, 1997.
- [51] Sangjin Hyun, Seoul National University. Private communication, 2000.
- [52] J. D. Jackson, *Classical Electrodynamics*. New York: Wiley, 1975.
- [53] G. Q. Jiang, W. H. Wong, E. Y. Raskovich, W. G. Clark, W. A. Hines, and J. Sanny, “Open-ended coaxial-line technique for the measurement of the microwave dielectric constant for low-loss solids and liquids,” *Rev. Sci. Instrum.*, vol. 64, p. 1614, 1993.
- [54] F. Jona and G. Shirane, *Ferroelectric Crystals*. New York: Dover, 1993.

- [55] G. W. C. Kaye and T. H. Laby, *Tables of physical and chemical constants*. Essex, England: Longman, 1995.
- [56] Ken Stewart, NASA Goddard. Grid polarizer sample.
- [57] G. Kent, “Dielectric resonances for measuring dielectric properties,” *Microwave J.*, p. 99, October 1988.
- [58] C. Kittel, *Introduction to Solid State Physics*. New York: Wiley, 7th ed., 1996.
- [59] N. Klein, H. Chaloupka, G. Müller, S. Orbach, H. Piel, B. Roas, L. Schultz, U. Klein, and M. Peiniger, “The effective microwave surface impedance of high- T_c thin films,” *J. Appl. Phys.*, vol. 67, p. 6940, 1990.
- [60] T. Konaka, M. Sato, H. Asano, and S. Kubo, “Relative permittivity and dielectric loss tangent of substrate materials for high- T_c superconducting film,” *Journal of Superconductivity*, vol. 4, p. 283, 1991.
- [61] R. S. Kwok and J.-F. Liang, “Characterization of high- Q resonators for microwave-filter applications,” *IEEE MTT-S Int. Microwave Sym.*, vol. 47, p. 111, 1999.
- [62] Lakeshore Cryotronics, Inc., Westerville, Ohio (phone 614-891-1392). DT-471 Silicon Diode Temperature Sensor.
- [63] A. F. Lann, M. Abu-Teir, M. Golosovsky, D. Davidov, S. Djordjevic, N. Bontemps, and L. F. Cohen, “A cryogenic microwave scanning near-field probe: Application to study of high- T_c superconductors,” *Rev. Sci. Instrum.*, vol. 70, p. 4348, 1999.

- [64] S.-C. Lee, C. P. Vlahacos, B. J. Feenstra, A. Schwartz, D. E. Steinhauer, F. C. Wellstood, and S. M. Anlage, “Magnetic permeability imaging of metals with a scanning near-field microwave microscope,” *Appl. Phys. Lett.* Submitted.
- [65] M. E. Lines and A. M. Glass, *Principles and Applications of Ferroelectric and Related Materials*. Oxford: Clarendon, 1977.
- [66] Longreach Scientific Resources, Orr’s Island, Maine (phone 207-833-6940). Tungsten tunneling tips, diameter 250 μm , length 25 mm.
- [67] Z. Ma, A. J. Becker, P. Polakos, H. Huggins, J. Pastalan, H. Wu, K. Watts, Y. H. Wong, and P. Mankiewich, “RF measurement technique for characterizing thin dielectric films,” *IEEE Trans. Electron Devices*, vol. 45, p. 1811, 1998.
- [68] J. S. Martens, V. M. Hietala, D. S. Ginley, T. E. Zipperian, and G. K. G. Hohenwarter, “Confocal resonators for measuring the surface resistance of high-temperature superconducting films,” *Appl. Phys. Lett.*, vol. 58, p. 2543, 1991.
- [69] T. Matsuda, R. Abe, and A. Sawada, “Nonlinearity of the dielectric constant of ferroelectric triglycine sulfate,” *J. Phys. Soc. Jpn.*, vol. 32, p. 999, 1972.
- [70] Microcal Software, Northampton, Massachusetts (www.originlab.com). Origin, version 5.0.
- [71] Microsoft Corporation, Redmond, Washington (www.microsoft.com). Visual Basic.

- [72] F. A. Miranda, C. H. Mueller, C. D. Cabbage, and K. B. Bhasin, "HTS/ferroelectric thin films for tunable microwave components," *IEEE Trans. Appl. Supercond.*, vol. 5, p. 3191, 1995.
- [73] F. A. Miranda, F. W. van Keuls, R. R. Romanofsky, and G. Subramanyam, "Tunable microwave components for Ku- and K-band satellite communications," *Integr. Ferroelectrics*, vol. 22, p. 269, 1998.
- [74] J. R. Mosig, J. E. Besson, M. Gex-Fabry, and F. E. Gardiol, "Reflection of an open-ended coaxial line and application to nondestructive measurement of materials," *IEEE Trans. Instrum. Meas.*, vol. 30, p. 46, 1981.
- [75] N. Nakatani, "Ferroelectric domain structure of tri-glycine sulfate observed using a scanning electron microscope," *Jpn. J. Appl. Phys.*, vol. 12, p. 1723, 1973.
- [76] N. Nakatani, K. Hayakawa, and H. Inoue, "Observation of domain structure in triglycine sulfate by a pyroelectric probe technique," *Jpn. J. Appl. Phys.*, vol. 34, p. 5453, 1995.
- [77] L. S. Napoli and J. J. Hughes, "A simple technique for the accurate determination of the microwave dielectric constant for microwave integrated circuit substrates," *IEEE MTT-S Int. Microwave Sym.*, vol. MTT-19, p. 664, 1971.
- [78] Neocera, Inc., Beltsville, Maryland (www.neocera.com). LTC-10 temperature controller.
- [79] A. M. Portis, *Electrodynamics of high-temperature superconductors*. New Jersey: World Scientific, 1993.

- [80] W. H. Press, *Numerical Recipes in C: The Art of Scientific Computing*. New York: Cambridge University Press, 1992.
- [81] S. Ramo, J. R. Whinnery, and T. V. Duzer, *Fields and Waves in Communication Electronics*. New York: Wiley, 1984.
- [82] M. E. Reeves, George Washington University. Private communication, 2000.
- [83] G. Roussy and M. Felden, “A sensitive method for measuring complex permittivity with a microwave resonator,” *IEEE MTT-S Int. Microwave Sym.*, vol. 14, p. 171, 1966.
- [84] G. Rupprecht and R. O. Bell, “Dielectric constant in paraelectric perovskites,” *Phys. Rev.*, vol. 135, p. A748, 1964.
- [85] S. M. Shapiro, R. W. Gammon, and H. Z. Cummins, “Visual observation of ferroelectric domains in TGS,” *Appl. Phys. Lett.*, vol. 10, p. 113, 1967.
- [86] Z.-Y. Shen, C. Wilker, P. Pang, W. L. Holstein, and D. Face, “High T_c superconductor-sapphire microwave resonator with extremely high Q-values up to 90 K,” *IEEE MTT-S Int. Microwave Sym.*, vol. 40, p. 2424, 1992.
- [87] A. V. Shil’nikov, V. A. Fedorikhin, A. P. Pozdnyakov, A. V. Sopit, and L. A. Shuvalov, “Dielectric properties of single-crystal deuterated triglycine sulfate (DTGS) in ultra-weak low- and infra-low-frequency electric fields,” *Phys. Solid State*, vol. 41, p. 977, 1999.
- [88] I. M. Sil’vestrova, “Dielectric parameters of deuterated triglycine sulfate,” *Sov. Phys. Crystallography*, vol. 6, p. 466, 1962.

- [89] I. I. Smolyaninov, C. H. Lee, and C. C. Davis, "Near-field second harmonic imaging of lean zirconate titanate piezoceramic," *Appl. Phys. Lett.*, vol. 74, p. 1942, 1999.
- [90] R. Sobiestianskas, J. Grigas, Z. Czapla, and S. Dacko, "Critical dielectric relaxation in ferroelectric betaine phosphite in the microwave regime," *Phys. Stat. Sol. A*, vol. 136, p. 223, 1993.
- [91] H. E. Stanley, *Introduction to phase transitions and critical phenomena*. New York: Oxford, 1971.
- [92] D. E. Steinhauer, C. P. Vlahacos, S. K. Dutta, B. J. Feenstra, F. C. Wellstood, and S. M. Anlage, "Quantitative imaging of sheet resistance with a scanning near-field microwave microscope," *Appl. Phys. Lett.*, vol. 72, p. 861, 1998.
- [93] D. E. Steinhauer, C. P. Vlahacos, S. K. Dutta, F. C. Wellstood, and S. M. Anlage, "Surface resistance imaging with a scanning near-field microwave microscope," *Appl. Phys. Lett.*, vol. 72, p. 1736, 1997.
- [94] D. E. Steinhauer, C. P. Vlahacos, F. C. Wellstood, S. M. Anlage, C. Canedy, R. Ramesh, A. Stanishevsky, and J. Melngailis, "Imaging of microwave permittivity, tunability, and damage recovery in (Ba,Sr)TiO₃ thin films," *Appl. Phys. Lett.*, vol. 75, p. 3180, 1999.
- [95] D. E. Steinhauer, C. P. Vlahacos, F. C. Wellstood, S. M. Anlage, C. Canedy, R. Ramesh, A. Stanishevsky, and J. Melngailis, "Quantitative imaging of dielectric permittivity and tunability with a near-field scanning microwave microscope," *Rev. Sci. Instrum.*, 2000.

- [96] S. K. Streiffer, C. Basceri, A. I. Kingon, D. Lipa, S. Bilodeau, R. Carl, and P. C. van Buskirk, "Dielectric behavior of CVD (Ba,Sr)TiO₃ thin films on Pt/Si," *Mat. Res. Soc. Symp. Proc.*, vol. 415, p. 219, 1996.
- [97] R. C. Taber, "A parallel plate resonator technique for microwave loss measurements on superconductors," *IEEE Trans. Appl. Supercond.*, vol. 9, p. 2182, 1991.
- [98] M. Tabib-Azar, N. S. Shoemaker, and S. Harris, "Non-destructive characterization of materials by evanescent waves," *Meas. Sci. Technol.*, vol. 4, p. 583, 1993.
- [99] M. Tabib-Azar, D.-P. Su, and A. Pohar, "0.4 μm spatial resolution with 1 GHz ($\lambda = 30 \text{ cm}$) evanescent microwave probe," *Rev. Sci. Instrum.*, vol. 70, p. 1725, 1999.
- [100] K. Takahashi and M. Takagi, "Topographic study of domain boundaries in tgs. i," *J. Phys. Soc. Jpn.*, vol. 44, p. 1266, 1978.
- [101] Y. Takayama, K. Deguchi, and E. Nakamura, "Re-examination of the dielectric critical slowing down in ferroelectric triglycine sulfate," *J. Phys. Soc. Jpn.*, vol. 53, p. 4121, 1984.
- [102] V. V. Talanov, L. V. Mercaldo, S. M. Anlage, and J. H. Claassen, "Measurement of the absolute penetration depth and surface resistance of superconductors and normal metals with the variable spacing parallel plate resonator," *Rev. Sci. Instrum.*, vol. 71, p. 2136, 2000.

- [103] V. I. Tal'yanskii, A. A. Filimonov, and E. G. Yashchin, "Curie-Weiss law for the nonlinear susceptibility χ_{zxy} of a KH_2PO_4 crystal," *Sov. Phys. Solid State*, vol. 12, p. 2224, 1971.
- [104] A. S. Thanawalla, S. K. Dutta, C. P. Vlahacos, D. E. Steinhauer, B. J. Feenstra, S. M. Anlage, and F. C. Wellstood, "Microwave near-field imaging of electric fields in a superconducting microstrip resonator," *Appl. Phys. Lett.*, vol. 73, p. 2491, 1998.
- [105] A. S. Thanawalla, W. Hu, D. E. Steinhauer, S. K. Dutta, B. J. Feenstra, S. M. Anlage, F. C. Wellstood, and R. B. Hammond, "Frequency-following imaging of the electric field around resonant superconducting devices using a near-field scanning microwave microscope," *IEEE Trans. Appl. Supercond.*, vol. 9, p. 3042, 1999.
- [106] N. A. Tikhomirova, S. A. Pikin, L. A. Shuvalov, L. I. Dontsova, E. S. Popov, A. V. Shilnikov, and L. G. Bulatova, "Visualization of static and the dynamics of domain structure in triglycine sulfate by liquid crystals," *Ferroelectrics*, vol. 29, p. 145, 1980.
- [107] S. Triebwasser, "Study of the second-order ferroelectric transition in triglycine sulfate," *IBM J. Research Dev.*, vol. 2, p. 212, 1958.
- [108] D. W. van der Weide and P. Neuzil, "The nanosilloscope: Combined topography and AC field probing with a micromachined tip," *J. Vac. Sci. Technol. B*, vol. 14, p. 4144, 1996.

- [109] C. P. Vlahacos, “A near-field scanning microwave microscope,” Master’s thesis, Physics Department, University of Maryland, College Park, Maryland, Dec. 1999.
- [110] C. P. Vlahacos, R. C. Black, S. M. Anlage, A. Amar, and F. C. Wellstood, “Near-field scanning microwave microscope with 100 μm resolution,” *Appl. Phys. Lett.*, vol. 69, p. 3274, 1996.
- [111] C. P. Vlahacos, D. E. Steinhauer, S. K. Dutta, B. J. Feenstra, S. M. Anlage, and F. C. Wellstood, “Non-contact imaging of dielectric constant with a near-field scanning microwave microscope,” *Microscopy and Analysis*, p. 5, January 2000.
- [112] C. P. Vlahacos, D. E. Steinhauer, S. K. Dutta, B. J. Feenstra, S. M. Anlage, and F. C. Wellstood, “Quantitative topographic imaging using a near-field scanning microwave microscope,” *Appl. Phys. Lett.*, vol. 72, p. 1778, 1998.
- [113] Š. Lányi, J. Török, and P. Řehůřek, “Imaging conducting surfaces and dielectric films by a scanning capacitance microscope,” *J. Vac. Sci. Technol. B*, vol. 14, p. 892, 1996.
- [114] W. L. Gore and Assoc., Inc., Newark, Delaware. Private communication.
- [115] W. L. Gore and Assoc., Inc., Newark, Delaware (www.gore.com). ReadyFlex microwave cables.
- [116] Y. G. Wang, M. E. Reeves, and F. J. Rachford, “Simultaneously imaging of dielectric properties and topography in a PbTiO_3 crystal by near-field scanning microwave microscopy,” *Appl. Phys. Lett.*, vol. 16, p. 219, 2000.

- [117] J. W. Ward, M. W. Utlaut, and R. L. Kubena, "Computer simulation of current density profiles in focused ion beams," *J. Vac Sci. Technol.*, vol. B5, p. 169, 1987.
- [118] C. Weber, R. Ono, J. C. Booth, L. Vale, S. Benz, A. M. Klushin, H. Kohlstedt, C. Buchal, and R. Semerad, "Coplanar transmission lines with meandering centre conductors in Y-Ba-Cu-O/Au bilayers," *Supercond. Sci. Technol.*, vol. 12, p. 998, 1999.
- [119] W. B. Weir, "Automatic measurement of complex dielectric constant and permeability at microwave frequencies," *Proc. IEEE*, vol. 62, p. 33, 1974.
- [120] C. Wilker, Z.-Y. Shen, V. X. Nguyen, and M. S. Brenner, "A sapphire resonator for microwave characterization of superconducting thin films," *IEEE Trans. Appl. Supercond.*, vol. 3, p. 1457, 1993.
- [121] Wolfram Research, Champaign, Illinois (www.wolfram.com). Mathematica, version 3.0.
- [122] Y. Xu and R. G. Bosisio, "Nondestructive measurements of the resistivity of thin conductive films and the dielectric constant of thin substrates using an open-ended coaxial line," *IEE Proc.-H*, vol. 139, p. 500, 1992.
- [123] R. A. York and R. C. Compton, "An automated method for dielectric constant measurements of microwave substrates," *Microwave J.*, p. 115, March 1990.
- [124] C. Zuccaro, M. Winter, N. Klein, and K. Urban, "Microwave absorption in single crystals of lanthanum aluminate," *J. Appl. Phys.*, vol. 82, p. 5695, 1997.

Curriculum Vitae

Name: David Ethan Steinhauer

Permanent Address: 20004 96th NE, Bothell, WA 98011

Degree and date to be conferred: Ph.D., 2000

Title of Dissertation: Quantitative Imaging of Sheet Resistance, Permittivity, and Ferroelectric Critical Phenomena with a Near-Field Scanning Microwave Microscope

Date of birth: September 18, 1972

Place of birth: Melrose, Massachusetts

Collegiate institutions attended

Institution	Dates attended	Degree	Date of degree
University of Washington	1991-1995	B.S., Physics	1995
University of Maryland	1995-1998	M.S., Physics	1998
University of Maryland	1998-2000	Ph.D., Physics	2000

Employment:

1. Consultant, Neocera, Inc., Beltsville, Maryland (August, 1999–Present)
2. Research Assistant, NASA Goddard Space Flight Center, Greenbelt, Maryland (June–August, 1995)
3. Programmer and Engineering Assistant, NeoPath, Inc., Redmond, Wash-

ington (June, 1992–August, 1993; June–August, 1994)

Professional Publications:

1. D. E. Steinhauer, C. P. Vlahacos, F. C. Wellstood, Steven M. Anlage, C. Canedy, R. Ramesh, A. Stanishevsky, and R. Ramesh, “Quantitative Imaging of Dielectric Permittivity and Tunability with a Near-Field Scanning Microwave Microscope,” to be published in *Rev. Sci. Instrum.*, July, 2000. cond-mat/0004439.
2. D. E. Steinhauer, C. P. Vlahacos, F. C. Wellstood, Steven M. Anlage, C. Canedy, R. Ramesh, A. Stanishevsky, and R. Ramesh, “Imaging of Microwave Permittivity, Tunability, and Damage Recovery in (Ba,Sr)TiO₃ Thin Films,” *Appl. Phys. Lett.*, vol. 75, p. 3180, 1999. cond-mat/9910014.
3. D. E. Steinhauer, C. P. Vlahacos, S. K. Dutta, B. J. Feenstra, F. C. Wellstood, and Steven M. Anlage, “Quantitative Imaging of Sheet Resistance with a Scanning Near-Field Microwave Microscope,” *Appl. Phys. Lett.*, vol. 72, p. 861, 1998. cond-mat/9712171.
4. D. E. Steinhauer, C. P. Vlahacos, S. K. Dutta, F. C. Wellstood, and Steven M. Anlage, “Surface Resistance Imaging with a Scanning Near-Field Microwave Microscope,” *Appl. Phys. Lett.*, vol. 71, p. 1736, 1997. cond-mat/9712142.
5. Sheng-Chiang Lee, C. P. Vlahacos, B. J. Feenstra, Andrew Schwartz, D. E. Steinhauer, F. C. Wellstood, and Steven M. Anlage, “Magnetic Permeability Imaging of Metals with the Scanning Near-Field Microwave Microscope,” submitted to *Appl. Phys. Lett.*, April, 2000.

6. Steven M. Anlage, D. E. Steinhauer, B. J. Feenstra, C. P. Vlahacos, and F. C. Wellstood, "Near-Field Microwave Microscopy of Materials Properties," in *Microwave Superconductivity*, ed. by H. Weinstock and M. Nisenoff, (Kluwer, Amsterdam, 2000). cond-mat/0001075.
7. C. P. Vlahacos, D. E. Steinhauer, S. K. Dutta, B. J. Feenstra, Steven M. Anlage, and F. C. Wellstood, "Non-Contact Imaging of Dielectric Constant with a Near-Field Scanning Microwave Microscope," *Microscopy and Analysis*, p. 5, January, 2000.
8. S. K. Dutta, C. P. Vlahacos, D. E. Steinhauer, Ashfaq S. Thanawalla, B. J. Feenstra, F. C. Wellstood, Steven M. Anlage, and Harvey S. Newman, "Imaging Microwave Electric Fields Using a Near-Field Scanning Microwave Microscope," *Appl. Phys. Lett.*, vol. 74, p. 156, 1999. cond-mat/9811140.
9. Steven M. Anlage, Wensheng Hu, C. P. Vlahacos, D. E. Steinhauer, B. J. Feenstra, S. K. Dutta, Ashfaq S. Thanawalla, and F. C. Wellstood, "Microwave Nonlinearities in High- T_c Superconductors: The Truth Is Out There," *J. Superconductivity*, vol. 12, p. 353, 1999. cond-mat/9808194.
10. Ashfaq S. Thanawalla, Wensheng Hu, D. E. Steinhauer, S. K. Dutta, B. J. Feenstra, Steven M. Anlage, F. C. Wellstood, and Robert B. Hammond, "Frequency Following Imaging of the Electric Field around Resonant Superconducting Devices using a Near-Field Scanning Microwave Microscope," *IEEE Trans. Appl. Supercond.*, vol. 9, p. 3042, 1999. cond-mat/9811141.
11. Steven M. Anlage, D. E. Steinhauer, C. P. Vlahacos, B. J. Feenstra, Ashfaq S. Thanawalla, Wensheng Hu, S. K. Dutta, and F. C. Wellstood, "Superconducting Materials Diagnostics Using a Scanning Near-Field Microwave

Microscope,” *IEEE Trans. Appl. Supercond.*, vol. 9, p. 4127, 1999. cond-mat/9811158

12. Ashfaq S. Thanawalla, S. K. Dutta, C. P. Vlahacos, D. E. Steinhauer, B. J. Feenstra, Steven M. Anlage, and F. C. Wellstood, “Microwave Near-Field Imaging of Electric Fields in a Superconducting Microstrip Resonator,” *Appl. Phys. Lett.*, vol. 73, p. 2491, 1998. cond-mat/9805239.
13. B. J. Feenstra, C. P. Vlahacos, Ashfaq S. Thanawalla, D. E. Steinhauer, S. K. Dutta, F. C. Wellstood, and Steven M. Anlage, “Near-Field Scanning Microwave Microscopy: Measuring Local Microwave Properties and Electric Field Distributions,” *IEEE MTT-S-Int. Microwave Sym. Digest*, p. 965, 1998. cond-mat/9802293.
14. C. P. Vlahacos, D. E. Steinhauer, S. K. Dutta, B. J. Feenstra, Steven M. Anlage, and F. C. Wellstood, “Quantitative Topographic Imaging Using a Near-Field Scanning Microwave Microscope,” *Appl. Phys. Lett.*, vol. 72, p. 1778, 1998. cond-mat/9802139.
15. Steven M. Anlage, C. P. Vlahacos, D. E. Steinhauer, S. K. Dutta, B. J. Feenstra, Ashfaq S. Thanawalla, and F. C. Wellstood, “Low Power Superconducting Microwave Devices and Microwave Microscopy,” *Particle Accelerators*, vol. 61, p. 321, 1998. cond-mat/9808195.

Presentations and Posters:

1. Contributed talk B20.07 at the American Physical Society March Meeting, March, 1997, Kansas City, Missouri. Title: “Measurements Using a Scanning Near-Field Coaxial Probe Microwave Microscope.”

2. Poster D41.50 at the American Physical Society March Meeting, March, 1997, Kansas City, Missouri. Title: "Near-Field Scanning Microwave Microscopy of Microwave Devices."
3. Contributed talk W26.03 at the American Physical Society March Meeting, March, 1998, Los Angeles, California. Title: "Quantitative Sheet Resistance Imaging with a Scanning Near-Field Microwave Microscope."
4. Poster I38.98 at the American Physical Society March Meeting, March, 1998, Los Angeles, California. Title: "Near-Field Scanning Microwave Microscopy."
5. Poster WEIF-49 at the IEEE International Microwave Symposium, June 10, 1998. Title: "Near-Field Scanning Microwave Microscopy: Measuring Local Microwave Properties and Electric Field Distributions."
6. Contributed talk XC08.05 at the American Physical Society March Meeting, March, 1999, Atlanta, Georgia. Title: "Imaging of Microwave Permittivity, Polarization, and Loss in Ferroelectric Thin Films."
7. Contributed talk KK8.6 at the Materials Research Society Meeting, December, 1999, Boston, Massachusetts. Title: "Imaging of Microwave Permittivity and Tunability in Nonlinear Dielectric Thin Films."
8. Invited talk K20.001 at the American Physical Society March Meeting, March, 2000, Minneapolis, Minnesota. Title: "Quantitative Imaging of Microwave Permittivity, Tunability, Polarization, and Domain Structure in Ferroelectrics."